Designing a Low Cost XY Stage for Abrasive Water Jet Cutting

by

Fadi Abu Ibrahim

B.E. Mechanical Engineering
American University of Beirut, 2002

SUBMITTED TO THE DEPARTMENT OF MECHANICAL ENGINEERING
IN PARTIAL FULLFILMENT OF THE DEGREE OF

MASTER OF SCIENCE IN MECHANICAL ENGINEERING

at the

MASSACHUSETTS INSTITUTE OF TECHNOLOGY

June 2004

Signature of Author..
Department of Mechanical Engineering
May 10, 2004

Certified by..
Alexander H. Slocum
Professor of Mechanical Engineering
Thesis Advisor

Accepted by..
Ain A. Sonin
Chairman, Department Committee of Graduate Students

ACKNOWLEDGEMENTS

Thanks first and foremost to God for giving me the talents and abilities to get this far, and for having me lucky enough to have my brother Feras. Feras I wish someday I will be like you. Thank you Rima, you are the best that happened to me since I moved to Boston. I also wish to thank my Dad, Mom, Hannoud, Rabih and Julie for their love and support.

Thanks to Alex Slocum for being the best advisor. He took me on board, gave me a great project and his guidance and expertise provided a great learning experience. I look forward to a prosperous future when me and Alex start making and selling our machines. This work was supported by iCampus, the MIT/Microsoft Alliance for research in educational technology, MIT's NSF Engineering Research Center, the Center for Bits & Atoms under Grant # CCR-0122419, a grant from Prof. Isaac Colbert, MIT's Dean for Graduate Students. I would also like to thank OMAX Corp. for their support and interest in building the parallel mechanism abrasive water jet cutter.

Thanks to Maureen Lynch for all her help. Thanks to Fred Cote for his always-present willingness to help in the machine shop and for teaching me so much about machining. Thanks to Ethan Crumlin for giving me the greatest help. Thanks to Jian Li, John Hart, James White and Shorya Awtar for their willingness to answer all my questions, and for being great friends. A special thanks to Jaime Werkmeister for remembering our birthdays.

Thanks to Marc and Carolina Graham for being the best friends I made in Boston, they where more than friends Marc and Carolina where family. Thanks to Bassel Younan and Karim Yehia for being the best apartment mates and for the great friendship we established. Thanks to Tilman Buchner, Tarek Abu Fakher and Haitham Aawar for being my best friends.

I would like to dedicate this thesis to Feras.

ABSTRACT

Designing a Low Cost XY Stage for Abrasive Water Jet Cutting

by

Fadi Abu Ibrahim

Submitted to the Department of Mechanical Engineering

On May 10, 2004 in Partial Fulfillment of the

Requirements for the Degree of Master of Science

In Mechanical Engineering

At the Massachusetts Institute of Technology

This thesis guides the reader through the design of an inexpensive XY stage for abrasive water jet cutting machine starting with a set of functional requirements and ending with a product. Abrasive water jet cutting allows for mass customization of 2D parts, such as inlaid tiles. Most water jet cutters are based on a prismatic-prismatic design (gantry type). In an effort to reduce the number of precision parts in the machine, a rotary-rotary parallel drive design is proposed. The proposed mechanism will be actuated by electric DC windshield wiper motors directly coupled to the links, this eliminates the need for gearing mechanisms that add up to the total cost and complexity of the design. Kinematics of the design is simulated for a working area of 310mm x 310mm. Dynamic analysis is performed and the concepts of decoupled and configuration invariant inertia are derived, simplified to a set of conditions on the kinematic structure/mass properties of the arm linkages and applied to significantly simplify the mechanism's control system. The XY stage was designed to be inexpensive and small enough to be placed in hardware stores, garages and small machine shops. A vision of water jet cutters sold in boxes stacked on shelves in Wal-Mart[1], available for all machinists, artists, schools, and industries might one day thus become a reality if the pumps could also be made cheaply.

Thesis Supervisor: Prof. Alexander H. Slocum

Title: Professor of Mechanical Engineering

---

[1] `http://www.walmart.com/`

I INTRODUCTION

I.1 Background

In a time when "better, faster, cheaper" are words to live by in the manufacturing world, the goal is to design a low cost XY stage actuated by two motors to be used in abrasive water jet cutting. Different techniques will be used to confirm a good quality at a low price. The design will be mainly targeted toward third world and evolving markets where precise machines at a low cost may be a solution to the current economic and industrial need to raise production quality. The machine should be inexpensive and small enough to be placed in hardware stores, garages and small machine shops for custom cutting any material. Not only companies will benefit from the design but also all technicians, artists, universities, school shops and people who will get the machine to turn their ideas into parts.

The purpose of designing a new machine is to best satisfy the needs of the customer who expects to profit from the investment. To achieve this goal, the Functional Requirements (FR) or static design goals, must be defined and used as the highest level of guidance. Hence the XY stage defined had to follow some predefined functional requirements listed in Table 1.

Functional Requirements	
Machineable area	310mmx310mm
Max acceleration	0.1g
Max velocity	10mm/sec
Resolution	0.5mm
Foot print	Small
Cost	≤$1500

Table 1: Functional Requirements for the machine

I.2 Water Jet Machining Overview

Abrasive jets have been in use in industry since 1982. Water jets, the precursor to abrasive jets, have been in use since 1970. Abrasive jets are widely used in the automobile, aerospace, and glass industries, to create precision parts from hard-to-cut materials. [1]

An abrasive jet uses water that is pressurized and then forced through a small sapphire orifice at about 2.5 times the speed of sound. Garnet[2] abrasive is then pulled into this high-speed stream of water and mixed together in a long tube. A stream of abrasive laden water exits the tube, and is directed at the material to be machined. The jet drags the abrasive through the material in a curved path and the resulting centrifugal forces on the particles press them against the work piece. The cutting action is a grinding process where the forces and motions are provided by water, rather than a solid grinding wheel. [1]

[2] Garnet is a reddish natural crystal, with a Mohr hardness of 6.5 to 7.5.

Apart from the advantages of speed, accuracy and ease of use, abrasive water jet machining is also environmentally friendly (no oils, noxious gases or liquids) provides a quality sandblasted-like finish and involves no heat in the machining process (can therefore be used to cut materials with low melting points). [1]

One of the major factors limiting the extensive use of abrasive water jet machining is controlling the process. The linear speed of the abrasive jet nozzle must be varied for changes in the shape of the part. Abrupt changes in speed or excessive speed can result in poor quality. As a result of this abrasive jets are usually reserved for low-tolerance large runs, where hundreds of parts are created with a well-tested program, or for materials that cannot be machined in any other way. Today, OMAX[3] is one of the leading abrasive jet machine providers and has developed software that can completely control the operation of the abrasive jet in an easy-to-use environment. [1]

I.3 Concept Generation

Five different general design concepts where developed and compared using simple calculations, along with an analysis for the simplicity of each concept. All concepts have the same water tank at the base; however the means of nozzle motion is unique to each concept.

In order to help do a first pass comparison of the concepts, a simple calculation was performed to measure the moment load on the support bearings. As the moment load on the support system increases, bigger bearings and more materials are required. The nozzle in each concept is assumed to be at its worst case position.

---

[3] http://www.omax.com/

For simplicity in the concept generation stage, all structural elements of the concepts are assumed to be aluminum beams with a $0.1m \times 0.1m$ cross section. The weight of the nozzle and the supporting components are assumed to be a 50N load at the end of the output beam.

I.3.1 First Concept

The first concept uses an X-Y axis system suspended upon the work space. The Y axis travels on the X axis that is aligned with the back of the machine. The nozzle travels back and forth on the Y-axis. Figure I-1 is a model of the first concept.

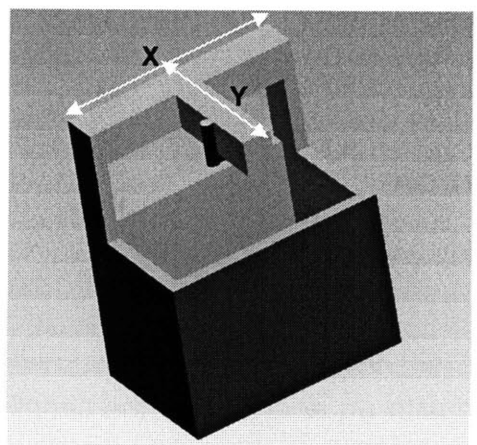

Figure I-1: Concept one

The moment load is calculated by $\sum M = \sum (F \times D)$. Where M is the moment load on the base, F is the load and D is the distance between the load and the base. Assuming the arms are $0.6m$ in length and weigh $50N$, the moment load on the base of concept one comes to be $45Nm$.

This concept requires two sets of linear motion systems and lengthy bellows to seal the linear bearings. Linear motion systems and bellows are expensive to buy, install, and maintain.

I.3.2 Second Concept

In the second concept shown in Figure I-2, there are no cantilever arms hence eliminating bending loads down to zero. However one extra linear stage is required and sealing is not simple due to the location of the linear stages very close to the water tank. The design is limited to cutting parts that are smaller than the bed size. The gantry also required two Y actuators to prevent racking. This concept is deemed infeasible when compared to the first concept, due to the extra costs and the complexity it brings forth to the machine design.

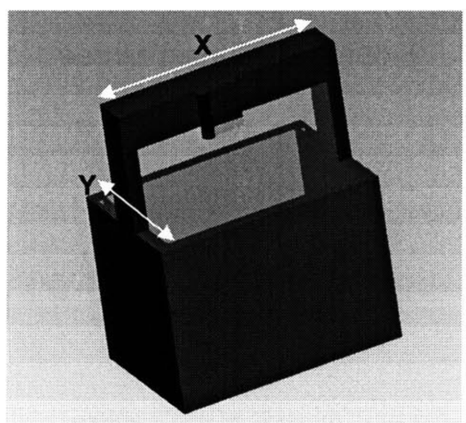

Figure I-2: Concept two

I.3.3 Third Concept

The third concept shown in Figure I-3, utilizes a rotating arm suspended from the center of a frame that is positioned at the center of the water tank. The nozzle traverses the rotating arm thus creating an $R\theta$ motion system. This concept seems good at first glance because it shortens the length of the cantilever arm and the system is counterbalanced by the two parts of the arm that are on opposite sides, thus reducing the load on the bearing system. However there are problems associated with it. The nozzle has to travel under the frame, which complicates sealing the axes. Secondly, having the water and abrasive lines follow the nozzle under the frame would be a difficult task. Lastly, the design is limited to cutting parts that are smaller than the bed size. This concept is deemed unfeasible compared to the first concept.

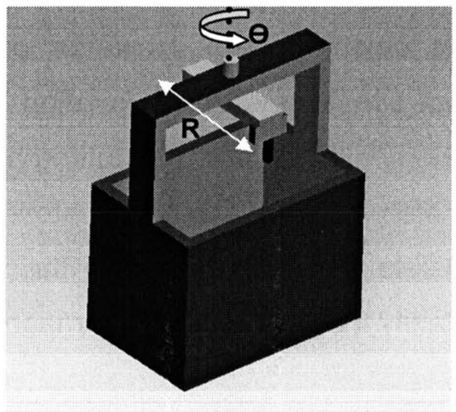

Figure I-3: Concept three

I.3.4 Fourth Concept

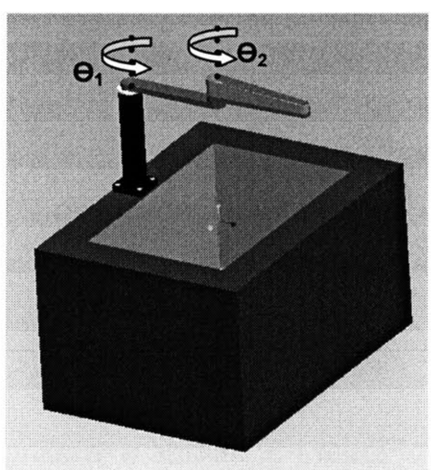

Figure I-4: Concept four

The fourth concept, shown in Figure I-4, is a $\theta\theta$ system. The nozzle, at the tip of the second arm, is positioned everywhere in the working area by two rotating arms. The lengths of the arms have to be slightly longer for the nozzle to reach the corners of the working area. However, the system uses two rotary joints, hence eliminating the need for sealing bellows and linear joints that are heavy and expensive. A weight of 20 N will be given to the arms in this concept, since no linear stages are mounted to the arms. The moment load at the base of the system was calculated to be 48Nm.

I.3.5 Fifth Concept

The Fifth concept, shown in Figure I-5, is a modification of the $R\theta$ system where an extra arm adds stiffness to the system. The rotary joint is located outside the working area hence solving all issues related to sealing, abrasive/water lines and part sizes. The moment load on the bearing base of the concept is 80Nm. The kinematics for this concept are formulated and simulated in Appendix A.

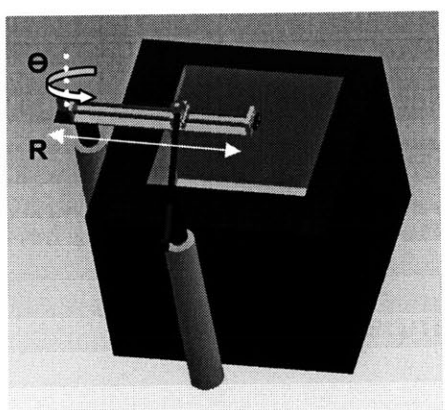

Figure I-5: Concept five

I.4 First Pass Comparison

Now that all the concepts are introduced, expensive and unfeasible ideas are discarded after a first pass analysis. Table 2 summarizes the concepts and their characteristics.

Concept	M_b (Nm)	Complexity and cost (1- 4)	No of bearing systems	Bellows (Y/N)	Feasible (Y/N)
1	45	3	2	Y	Y
2	--	4	3	Y	N
3	--	4	2	Y	N
4	48	1	2	N	Y
5	80	2	2	Y	Y

Table 2: First pass comparison of concepts

From the table, three feasible concepts emerge; concepts one (XYjet), four (θjet) and five (Ajet). The three concepts are put through further analysis in a second pass comparison and a final concept selection stage to ultimately choose the best system for the machine.

I.5 Second Pass Comparison

In the second pass analysis the above concepts are taken into more detail and then compared based on the footprint and the sensitivity to errors from the actuators (backlash).

I.5.1 Sensitivity Analysis

The errors caused by angular deflections are the most troublesome, since these result in what is known as Abbe error.

$$Abbe\_error = (offset\_dist) \times \sin(angle)$$

"Perhaps the greatest sin in precision machine design is to allow an angular error to manifest itself in a linear form via amplification by a moment arm". [2] Due to the importance of Abbe errors, a sensitivity analysis using MATLAB was performed by passing the machine throughout the working area and calculating the respective error amplification at the tool tip. The MATLAB script was simulated for various working areas, noting the maximum Abbe error value corresponding to each working area. Figure I-6 is a plot of the maximum Abbe error values versus working areas $(L \times L)$ for both the Ajet and the θjet. The Abbe errors due to the actuators are zero in the XYjet. The sensitivity to errors in the Ajet is higher than that in the θjet and in both concepts the sensitivity values increase as the working area gets larger.

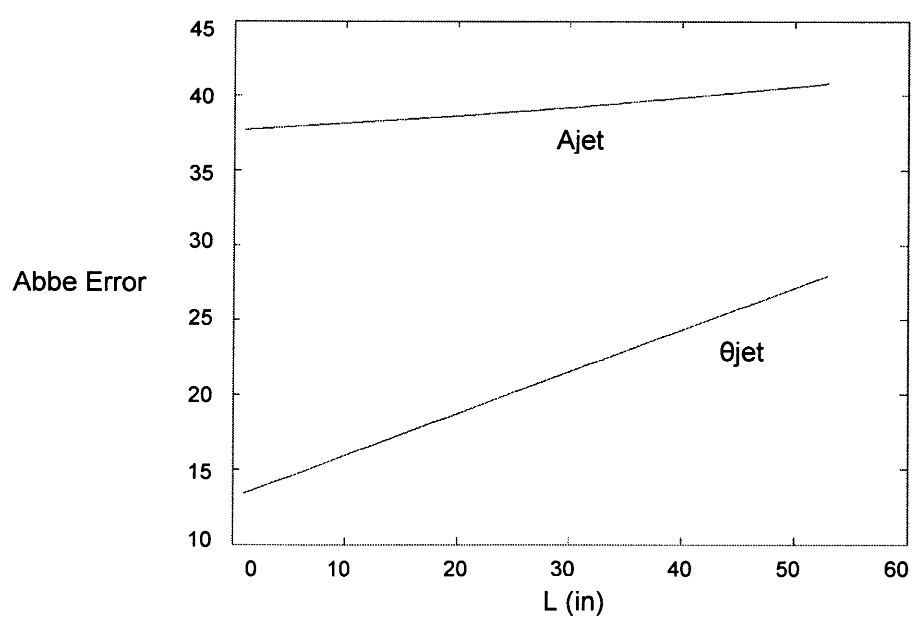

Figure I-6: Sensitivity to error vs. Work area size (LxL)

I.5.2 Foot Print

Foot print, or the total area taken by the machine in the workshop, is a major functional requirement. The smaller the footprint, the more appealing the design. The working area was changed form 12.5x12.5 to 25x25 in^2 for each concept, and the respective footprint was calculated via a MATLAB code. Figure I-7 is a plot of the Foot Print vs. working area for both the Ajet and the θjet. It is noticed that the footprint of the Ajet is bigger then that of the θjet and the XYjet. The θjet is not as stiff in the Z direction as the Ajet however that could be accounted for, as shown later in Chapter III. The θjet and XYjet are taken into the final pass comparison stage,

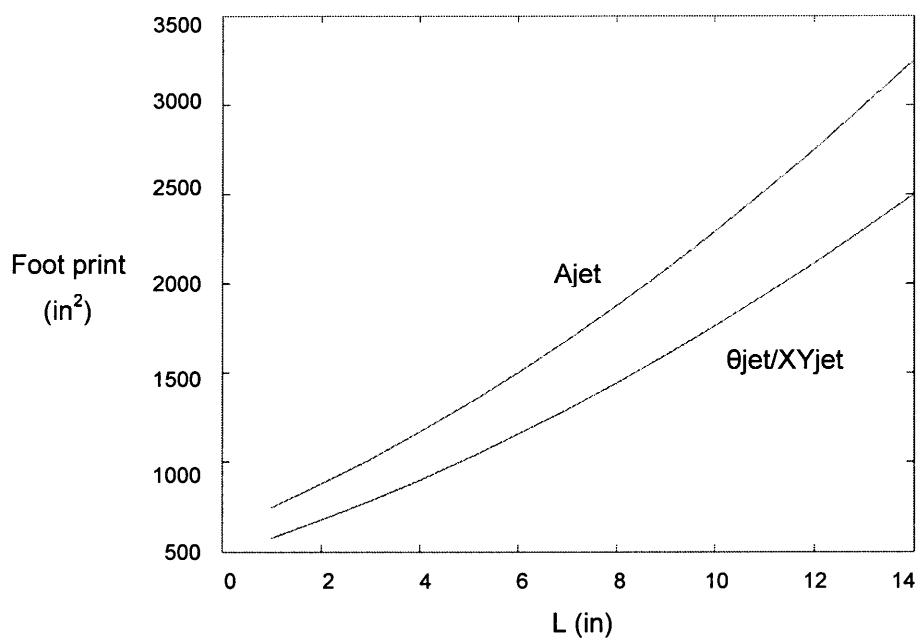

Figure I-7: Foot Print vs. working area (LxL)

I.6 Final Pass Comparison

I.6.1 Error Budget

In order to represent the relative position of a body in space with respect to a reference system, a 4x4 matrix is needed. The matrix is called the homogeneous transfer matrix. The first three columns are direction cosines (unit vectors i, j, k) representing the orientation of the body with respect to the reference coordinate frame. The last column is the position of the body with respect to the reference frame. This summary is explained in full detail in [2]

$$T_n^R = \begin{bmatrix} O_{ix} & O_{iy} & O_{iz} & P_x \\ O_{jx} & O_{jy} & O_{jz} & P_y \\ O_{kx} & O_{ky} & O_{kz} & P_z \\ 0 & 0 & 0 & 1 \end{bmatrix}$$

The upper superscript is the reference frame in which the results are desired to be represented in. The subscript is the reference frame from which you are transferring. It follows then that the equivalent coordinates of a point in a coordinate frame n with respect to the reference frame R, are

$$\begin{bmatrix} X_R \\ Y_R \\ Z_R \end{bmatrix} = T_n^R \begin{bmatrix} X_n \\ Y_n \\ Z_n \end{bmatrix}$$

In this case, there are three reference coordinate systems, the position of the tool tip with respect to the reference one will be: $T_3^R = T_1^R T_2^1 T_3^2$. All rigid bodies have three translational $(\delta_X, \delta_Y, \delta_Z)$ and three rotational $(\varepsilon_{X,}\varepsilon_{Y,}\varepsilon_Z)$ errors. The DOF motions or errors result from several sources, such as imperfections in the bearings, deflections due to loads, thermal distortions, etc. The goal in error budgeting is to allocate allowable values for each. For any machine member, the error matrix describing its error in position with respect to its ideal position is:

$$E=\begin{bmatrix}1 & -\varepsilon_z & \varepsilon_y & \delta_x\\ \varepsilon_z & 1 & -\varepsilon_x & \delta_y\\ -\varepsilon_y & \varepsilon_x & 1 & \delta_z\\ 0 & 0 & 0 & 1\end{bmatrix}\Rightarrow T_n^R=\begin{bmatrix}1 & -\varepsilon_z & \varepsilon_y & a+\delta_x\\ \varepsilon_z & 1 & -\varepsilon_x & b+\delta_y\\ -\varepsilon_y & \varepsilon_x & 1 & c+\delta_z\\ 0 & 0 & 0 & 1\end{bmatrix}$$

Where a, b and c are the distances between the two coordinate systems in the x, y and z. Since the cutting tool is a jet of water the lateral direction is not a sensitive direction, hence the total error in that direction is not as important as the one in the x and y. Error sources are sketched and formulated in Table 3.

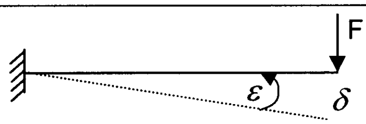	$\delta=\dfrac{FL^3}{3EI}$ $\quad\varepsilon=\dfrac{FL^2}{2EI}$
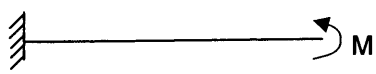	$\delta=\dfrac{ML}{EI}$ $\quad\varepsilon=\dfrac{ML}{EI}$
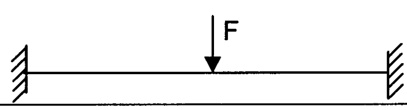	$\delta=\dfrac{FL^3}{192EI}$
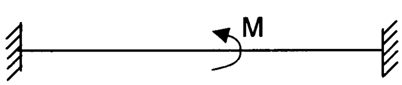	$\delta=\dfrac{ML}{12EI}$
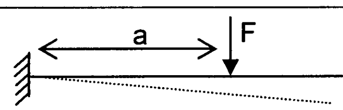	$\delta=\dfrac{Fa^2(a-3L)}{6EI}$ $\quad\varepsilon=\dfrac{Fa^2}{2EI}$
Torsion	$\varepsilon=\dfrac{TL}{GJ}$
Tension / Compression	$\delta=\dfrac{FL}{AE}$

Table 3: Structural error sources

After specifying the sources of systematic errors, each member was individually taken. The deflections and machining and random errors where taken and entered into the E matrix to give the homogeneous transfer function matrix. Table 4 shows the resultant errors in the x, y and z directions. A MATLAB code was developed based on the above formulations. The numerical results were proved correct by running the analysis using an EXCEL spread sheet designed by Slocum et al.[4]

Concepts	δ_x	δ_y	δ_z
θjet	0.0016	-0.0019	-0.1616
XYjet	0.0011	0.0014	-0.0695

Table 4: Resulting values from the error budget analysis

For an estimate cost of $1500 and a not so high resolution of 0.5mm, the θjet is the best mechanism for the low cost XY stage. The θjet's low stiffness in the Z direction will be taken into account in the next section.

[4] http://pergatory.mit.edu/2.75/software_tools/software_tools.html

II CONTROL / ACTUATION

II.1 Sketch

A sketch of the series drive rotary-rotary mechanism is shown in Figure II-1a. An alternative mechanism that is stiffer in the Z direction can be a 5 link parallel drive mechanism where the motors are both at the base. Figure II-1b is a sketch of the parallel drive mechanism. Table 5 gives some first dimensions for the machine to carry on with the analysis. Most of the concepts and the calculations in this chapter are based on [3] [4].

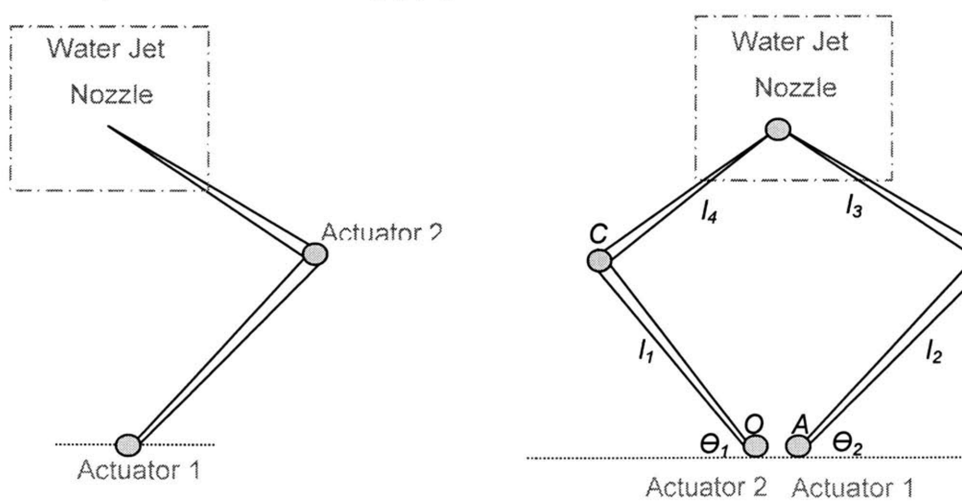

Figure II-1: Preliminary sketches of two possible rotary-rotary mechanisms

Machine Dimensions	
Arms Length (L_1,L_2)	35cm (14")
Arm Cross Section	380mmx25mm (1.5"x1")
Material	Aluminum 6061

Table 5: Machine Dimensions

II.2 Actuation Mechanisms

Research in the field of parallel drives analyzes and optimizes the kinematics however it does not always stress means of actuation, structure simplicity and controls. A robot can be actuated through a direct drive mechanism or through transmission. With a transmission, the reducer must supply the necessary gear reduction while maintaining the proper precision level by introducing no backlash to the link. When the word backlash is read, the first idea that pops into the mind is "preloaded gears", but what about the friction in preloaded gear mechanisms and the complexity of building a preloaded gear structure. Friction is unpredictable and large values lead to poor control accuracy, by producing friction torques in the force control system. In addition, gearing mechanisms are a source of compliances, and low mechanical stiffness causes arm deflections and limits the dynamic response. If the higher order delay from the low stiffness makes the system unstable, then the loop gain of the system cannot be increased. Poor stiffness at the gearing also causes vibration, a critical issue for high speed manipulation, where the robot reaches a certain position and cannot move to the next step.

In a direct drive mechanism the motor's rotor is directly coupled to the link, thus potentially eliminating gearing completely. This results in friction and backlash being removed except at the bearings, and a reliable stiffer mechanical structure with no gears to wear. The joint consists of a motor, a set of arm links and the bearings. This will result in a better control performance, and improved position accuracy. Since the construction uncertainties in this simple structure are greatly reduced, a higher precision, simple dynamics and better system response are expected. However, a direct drive motor requires very high torque and current drives which can result in very large motor size, inertia, and cost. The direct drive mechanism will be taken into more detail in the sections to come. But next the drive systems and actuators will be discussed.

II.3 Drive Systems / Actuators

For mechanisms with linear actuators, several options of actuation are available: hydraulic, pneumatic, piezoelectric, electric, etc... However for revolute joints, electric motors are the best choice to use. Key components in the design of the robot are the motors and the drive amplifiers. There should be enough torque at all times; In addition, torque fluctuations should be minimized in order to achieve accurate control. Direct Current (DC) motors or Brushless D.C. torque motors can be used

A direct drive DC motor consists of a stator, rotor and bush rings. The torque is exerted at the air gap between the rotor and the stator, and it is proportional to the diameter of the rotor. That explains why motors with a large diameter and short rotor lengths are used in direct drive robots. In an ideal motor the Torque is constant, however in reality it varies as the rotor rotates which results in Torque ripple that prevents smooth motions and accurate control.

DC motors have high efficiency, low torque ripple, linear torque speed characteristics and simplicity of construction. However in these motors the large currents delivered to the rotor are through mechanical commutators, as a result sparks can be generated causing the brush to wear, and producing unwanted noise.

Brushless DC motors replace the mechanical commutation with electric switching circuits. No sparks are generated while preserving all the previous characteristics of DC motors. The setup of such motors is different; the rotor has the permanent magnets and the stator carries the coils. The coils being placed on the stator that has a bigger surface area than the rotor results in better heat transfer and cooling of the coils. The position of the rotor is located through a position sensor and accordingly the proper switches are triggered. Two problems are faced with these motors: First, they are expensive. Second, there is a Torque ripple when the switches turn on and off as the motor rotates. Hence, for designing the 2D planar robot a conventional DC motor will be used.

In an attempt to reduce the price of the machine and make it easy to build anywhere in the world it is hypothesized that DC windshield wiper motors will be used. These motors are widely available; people interested in building the machine themselves can get them out of old cars. The motors typically are not back-drivable due to an internal worm gearbox, have a tolerable backlash, a stalling Torque of 14 Nm and a no load speed of 81 rpm. These motors are very easy to mount as shown in Figure II-2 and posses enough Torque to actuate the machine at the desired speeds. Backlash in the motors can be reduced by the spring preload from the high pressure water supply tube and future control schemes to be designed.

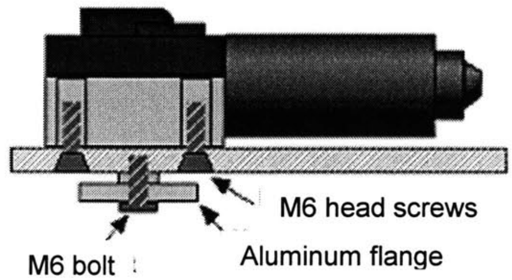

Figure II-2: Mounting the windshield wiper motor

II.4 Link Design and Control Issues

If one motor is at the end of the first link, the robot becomes heavy because the first link and motor must support and drive the second link and motor. The weight of the motor that drives one link is a load on the motor that drives the previous link. As a result the required torque needed to drive individual links increases exponentially, therefore the sizes of consecutive motors increases exponentially. Another design that can be used to solve this problem is to have the motors at the base, and then transmit the torque to the links through respective links. Then the challenge becomes to overcome the complexity added to the design through the extra mechanical links.

II.4.1 Damping

In direct drive systems the bearings are the only source of damping, hence we will be dealing with an almost zero damping situation that is very hard to control. This is because when the inertial load to the mechanical damping coefficient is large the back *emf* of the motor yields a damping effect. This electromechanical damping effect is less than the amount needed to stabilize the system response. Velocity feedback compensation is a good way to deal with this problem, but one must set the gain K_v very high to get the required responses. In addition, a high performance sensor is needed to accurately measure the slow speed of the motor (same as velocity of the link) that isn't affected by noise disturbances.

II.4.2 Stiffness

The robot's endpoint static stiffness is the ability to maintain a commanded position in the face of external loads. This stiffness is determined through the mechanical construction of the system as well as the feedback loop gains of the individual servo systems. In a gear-drive system the output torque is amplified by the gear ratio which is not the case in a direct drive system. Therefore the direct drive robot needs a higher controller gain.

II.4.3 Equations of Motion

Nonlinear and highly coupled is the general behavior of a manipulator arm. Equation 2-1 gives the dynamic equation of the i^{th} motor:

$$\left(J_{rot} + \frac{J_{arm}}{n_i^2}\right)\ddot{\alpha}_i + \frac{\tau_{coup}}{n_i} + \frac{\tau_{non}}{n_i} = \tau_{mot} \qquad (2\text{-}1)$$

Where τ_{non} τ_{coup} τ_{mot} are the nonlinear, coupling and motor torques. n_i is the gear ratio of the i^{th} motor in the mechanism. J_{arm} is the arm inertia that varies depending upon the arm configuration. J_{rotor} is the rotor inertia, invariant. $\ddot{\alpha}_i$ is the motor's angular acceleration. Note that the nonlinear and coupling torques are attenuated by the gear ratio, where as depending on the gear ratio the variations of J_{arm} will be attenuated by n_i^2.

II.4.4 Over Heating

From Equation 2-1, it can be noticed that the gravity load is attenuated by n_i $\left(\tau_{coup}/n_i\right)$, thus in a direct drive mechanism when the motor is at rest gravity is attenuated. Gear friction produces a torque that would oppose the gravity torque; in direct drive systems this is no more present. Hence the motors will take the gravity load entirely and continuously, which will over heat the actuation system. When choosing the actuator special attention should be placed on the overheating problem. However in our planar robot there are no gravity loads.

II.5 Dynamics and Modeling

II.5.1 General Dynamics

The equation of motion for the manipulator arm:

$$\tau_i = H_{ii}\ddot{\theta}_i + \sum H_{ij}\ddot{\theta}_j + \sum_j \sum_k \left(\frac{\partial H_{ij}}{\partial \theta_k} - \frac{1}{2}\frac{\partial H_{jk}}{\partial \theta_i} \right) \dot{\theta}_j \dot{\theta}_k + \tau_{gi} \qquad (2\text{-}2)$$

Where τ_i, τ_{gi} are the joint, gravity torques. θ_i is the joint displacement. H_{ij} is the i-j element of the inertia matrix. The first term in the inertia matrix is determined by the kinematics structure of the manipulator arm and the mass properties of the links. Therefore a design problem is to reduce the inertia to a diagonal form that gets rid of the second term in Equation 2-2. (the inertia torque caused by the other accelerating links).

$$\tau_i = H_{ii}\ddot{\theta}_i + \sum_k \left(\frac{\partial H_{ii}}{\partial \theta_k}\dot{\theta}_i \dot{\theta}_k - \frac{1}{2}\frac{\partial H_{kk}}{\partial \theta_i}\dot{\theta}_k^2 \right) + \tau_{gi} \qquad (2\text{-}3)$$

Nonlinear velocity torques, given in the second term, result from the spatial dependency of the diagonal elements on the inertia matrix. But if we can figure out a way to make the inertia matrix independent of the link configuration then the third term in Equation 2-3 is eliminated to give:

$$\tau_i = H_{ii}\ddot{\theta}_i + \tau_{gi} \qquad (2\text{-}4)$$

Now the system is linear and decoupled, and can be treated as a SISO (single input, single output) system.

II.5.2 Modeling

Consider a robot with a serial number of links. Let l be an arbitrary joint number. We then imagine all the joints between $l+1$ and n immobilized and combined as one rigid body.

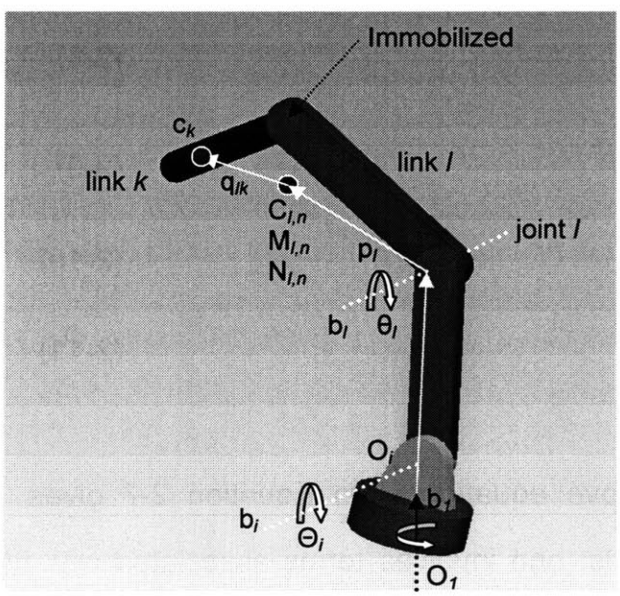

Figure II-3: Lumping of links. (Total mass and center of gravity)

Kinetic energy stored in the links can be modeled as:

$$T = \sum_{x=1}^{n} \left(m_x v_{cx}^T v_{cx} + \omega_x^T I_x \omega_x \right) / 2 \tag{2-5}$$

Where m_k is the mass of link k, I_k is the inertia tensor of link k, $v_{ck} = \sum_{i=1}^{k} b_i \dot{\theta}_i \times r_{i,ck}$ is the linear velocity of the centroid of link k and $\omega_k = \sum_{i=1}^{k} b_i \dot{\theta}_i$ is the angular speed of link k. Substituting v_{ck} and into Equation 2-5 gives:

$$T = \sum_{i=1}^{k} \sum_{j=1}^{k} \left(H_{ij} \dot{\theta}_i \dot{\theta}_j \right) \frac{1}{2} \tag{2-6}$$

$$H_{ij} = \sum_{k=\max[i,j]}^{n} \left[m_k \left(b_i^T b_j . r_{i,ck}^T r_{j,ck}^T - b_j^T r_{i,ck} . b_i^T r_{j,ck} \right) + b_i^T I_k b_j \right] \tag{2-7}$$

Let $M_{l,n}$ $C_{l,n}$ and p_l be the mass, centroid of the (n-i+1) links and the position between O_l and $C_{l,n}$

$$M_{l,n} = \sum_{k=1}^{n} m_k \tag{2-8}$$

$$p_l = \sum_{k=1}^{n} \frac{m_k r_{l,ck}}{M_{l,n}} \tag{2-9}$$

$$r_{i,ck} = r_{i,l} + p_l + q_{l,k} \tag{2-10}$$

$$\sum_{k=1}^{n} m_k q_{l,k} = 0 \tag{2-11}$$

Substituting the above equations into Equation 2-7 gives H_{ij} which can be divided into two parts: one involves terms associated with the last (*n-l+1*) links and the other for the other links. Let $N_{l,n}$ be the inertia tensor of the *n-l+1* links relative to $C_{l,n}$.

$$H_{ij} = \sum_{k=\max[i,j]}^{n} \left[m_k \left(b_i^T b_j . r_{i,ck}^T r_{j,ck}^T - b_j^T r_{i,ck} . b_i^T r_{j,ck} \right) + b_i^T I_k b_j \right] + b_i^T N_{l,n} b_j$$
$$+ M_{l,n} \left[b_i^T b_j \left(r_{i,l} + p_l \right)^T \left(r_{j,l} + p_l \right) - b_i^T \left(r_{i,l} + p_l \right) . b_i^T \left(r_{j,l} + p_l \right)^T \right] \qquad (2\text{-}12)$$

We will first try to set the off diagonal elements to be invariant or zero for all arm configurations. Note the sketch in Figure II-4, the inertial frame O-XYZ is located to coincide with O_l and the Z axis is set in the direction of b_l.

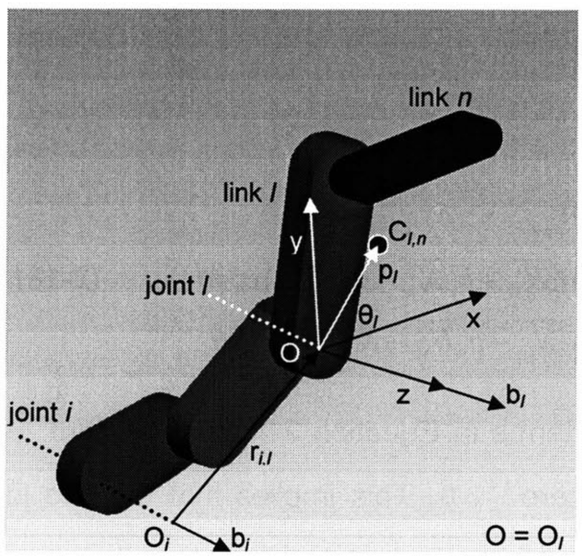

Figure II-4: Immobilizing joints

$$p_l = \begin{bmatrix} L_{l,n} \cos\theta_l \\ L_{l,n} \sin\theta_l \\ 0 \end{bmatrix} \qquad (2\text{-}13)$$

$$A = \begin{bmatrix} \cos\theta_l & -\sin\theta_l & 0 \\ \sin\theta_l & \cos\theta_l & 0 \\ 0 & 0 & 1 \end{bmatrix} \text{ Rotation matrix} \qquad (2\text{-}14)$$

$$N = A\overline{N_{l,n}}A^T = \begin{bmatrix} \overline{N_{xx}} & \overline{N_{xy}} & \overline{N_{xz}} \\ \overline{N_{xy}} & \overline{N_{yy}} & \overline{N_{yz}} \\ \overline{N_{xz}} & \overline{N_{yz}} & \overline{N_{zz}} \end{bmatrix} \quad (2\text{-}15)$$

If b_i is not perpendicular to b_l, the x-y plane intersects b_i at O_i. The position vector of O_i, $r_{i,l}$ and the direction cosines of the i^{th} joint axis are given by:

$$r_{i,l} \equiv \overrightarrow{O_iO_l} = \begin{bmatrix} r_x \\ r_y \\ r_z \end{bmatrix} \quad (2\text{-}16)$$

$$b_i = \begin{bmatrix} b_x \\ b_y \\ b_z \end{bmatrix} \quad (2\text{-}17)$$

Substituting the above:

$$\begin{aligned} H_{il} = \left(ML^2 + \overline{N_{zz}}\right)b_z + (b_x\overline{N_{xz}} + b_y\overline{N_{yz}} + MLb_zr_x)\cos\theta \\ +(b_y\overline{N_{xz}} - b_x\overline{N_{yz}} + MLb_zr_y)\sin\theta \end{aligned} \quad (2\text{-}18)$$

For H_{il} = 0, all three terms in Equation 2-1 must be zero. $\overline{N_{zz}} > 0, ML^2 > 0 \Rightarrow$ For the first term to be zero $b_z = 0$. This implies that the two joint axes have to be perpendicular to each other which in turn limit the design options to 2D. Second and third terms = *0* $\Rightarrow \overline{N_{yz}} = 0, \overline{N_{xz}} = MLr_z$. As for the diagonal parameters, from Equation 2-12 we get:

$$\begin{aligned} H_{ii} = \sum_{k=i}^{l-1}\left(m_k\left[\left[r_{i,ck}\right]^2 - \left(b_i^T r_{i,ck}\right)^2\right]\right) + b_i^T ANA^T b_i + \\ M\left(\left[\left|r_{i,l} + p_l\right|^2 - \left[b_i^T\left(r_{i,l} + p_l\right)\right]^2\right]\right) \end{aligned} \quad (2\text{-}19)$$

Calculations similar to those for the non diagonal elements can be performed. Summarized below are the necessary conditions that the kinematics and the mass properties the arm must satisfy for the diagonal/off-diagonal H elements to be "invariant".

Condition 1: $b_i = b_l$ The two joint axes are parallel,

Condition 2: $\begin{cases} b_i^T b_l \neq 0 \text{ and} \\ r_x = r_y = 0 \Rightarrow (Oi{=}O)\text{, and} \\ \overline{N_{xy}} = 0\text{, and} \\ \overline{N_{xx}} + ML^2 = \overline{N_{yy}} \end{cases}$

Condition 3: $\begin{cases} b_i^T b_l = 0\text{, and} \\ L{=}0 \text{ and} \\ \overline{N_{xy}} = 0 \text{ and} \\ \overline{N_{xx}} = \overline{N_{yy}} \end{cases}$

Condition 4: $\begin{cases} b_i^T b_l = 0 \text{ and} \\ r_y{=}0 \\ \overline{N_{xy}} = 0 \\ \overline{N_{xx}} = \overline{N_{yy}} + ML^2 \end{cases}$

II.5.3 Arm Design: Two DOF

An open kinematic chain manipulator arm has a decoupled inertia arm if the joint axes of the two links are orthogonal:

Condition 1: $m_2 L r_z = \overline{N_{xz}}$

Condition 2: $\overline{N_{yz}} = 0$

Two specific cases arise when $L = 0$ and $r_z = 0$. Conditions 1 and 2 are shown in Figure II-5.

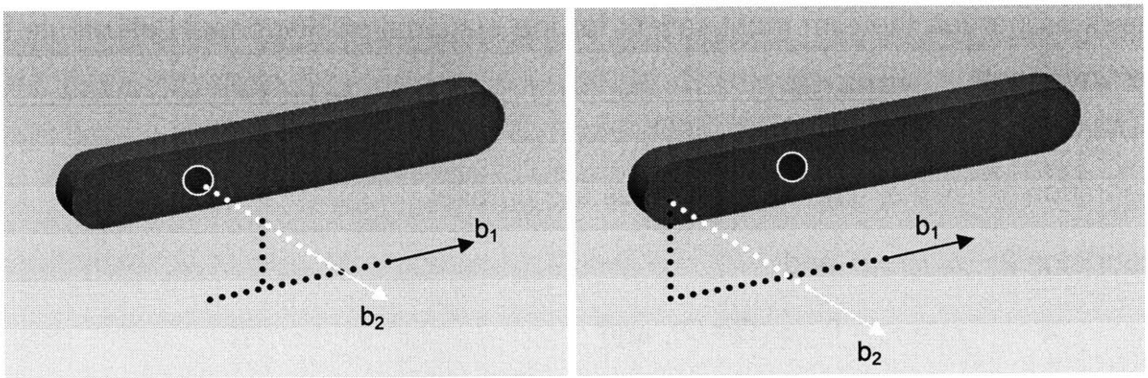

Figure II-5: (a) L=0 (b) r_z =0

For invariant inertia, conditions 1 and 2 apply. But suppose we take the case where the joint axes are not normal to each other ($b_z \neq 0$), in that case the above two conditions apply in addition to the following conditions:

Condition 3: $\begin{cases} b_z = 1, (b_x = b_y = 0) \\ L = 0 \end{cases}$

Condition 4: $\begin{cases} r_x = r_y = 0 \\ \overline{N_{xy}} = \overline{N_{yz}} = \overline{N_{xz}} = 0 \\ \overline{N_{xx}} + ML^2 = \overline{N_{yy}} \end{cases}$

Conditions 3 and 4 are sketched in Figure II-6.

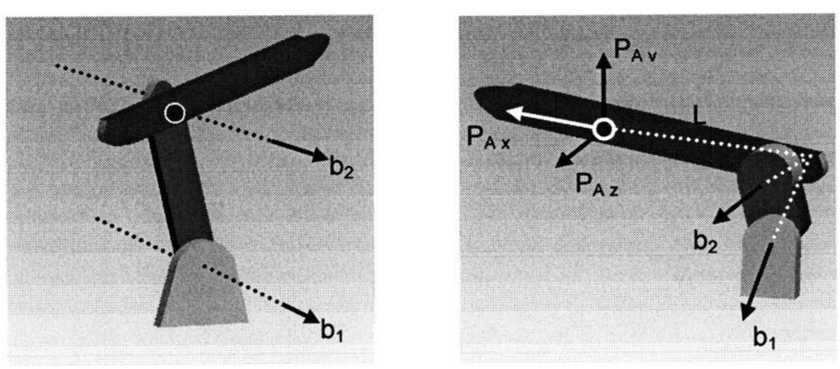

Figure II-6: Conditions 3 and 4

Mechanisms with oblique arms are seldom used and not practical (Figure II-6). A 3DOF system is reduced to a 2DOF one by immobilizing one of the links. Such mechanisms are designed by building two 2DOF models above each other. From the previous section we derived four conditions and sketched the equivalent model for having an invariant inertia matrix. The fourth Condition will be ignored.

II.5.4 Application to the serial drive mechanism

For the serial drive mechanism the inertia matrix derived in Appendix A can be summarized by:

$$H_{11} = m_1 l_{c1}^2 + I_1 + m_2(l_1^2 + l_{c2}^2 + 2l_1 l_{c2}\cos\theta_2) + I_2$$

$$H_{22} = m_2 l_{c2}^2 + I_2$$

$$H_{12} = m_2 l_1 l_{c2}\cos\theta_2 + m_2 l_{c2}^2 + I_2$$

$$h = m_2 l_1 l_{c2}\sin\theta_2$$

Since H_{11} and H_{12} depend on θ_2, they are configuration dependent and cannot be reduced to zero for all θ_2 by changing the mass properties. The only way for this to work is to have the joint axis pass through the centroid of the second link, which is not logical from a design point of view.

II.5.5 Application to the parallel drive mechanism

Appendix A gives the formulation of the kinematics and dynamics of the parallel drive mechanism. Inertia matrix H:

$$H = \begin{bmatrix} H_{11} & H_{21} \\ H_{12} & H_{22} \end{bmatrix}$$

$$H_{11} = I_1 + m_1 l_{c1}^2 + I_3 + m_3 l_{c3}^2 + m_4 l_1^2$$

$$H_{22} = I_4 + m_4 l_{c4}^2 + I_2 + m_2 l_{c2}^2 + m_3 l_2^2$$
$$H_{12} = (m_3 l_2 l_{c3} - m_4 l_1 l_{c4})\cos(\theta_2 - \theta_1)$$

From the inertia matrix, we notice that H_{11} and H_{22} are independent of the configuration however H_{12} depends on the angles θ_1 and θ_2. To have a simple decoupled inertia matrix we can reassign values for the mass and the dimensions of the manipulator links, so that the inertia term H_{12} goes to zero.

$$m_3 l_2 l_{c3} - m_4 l_1 l_{c4} = 0 \rightarrow \frac{m_3}{m_4} = \frac{l_1 l_{c4}}{l_2 l_{c3}}$$

Satisfying the above condition results in a completely decoupled and invariant inertia matrix. Hence the parallel drive mechanism has an unprecedented advantage over the serial one and is the mechanism of choice on the water jet cutter. Figure II-7 gives the foot print (19" x 24") and the mechanism dimensions for the detailed design of the machine. An experimental setup to test for decoupling between motors is to let one motor track a sinusoidal position command while keeping the other motor at rest. The peak-peak ratios between the actual position signal of the driven motor to that of the stationary one is a measure of coupling in the arm dynamics.

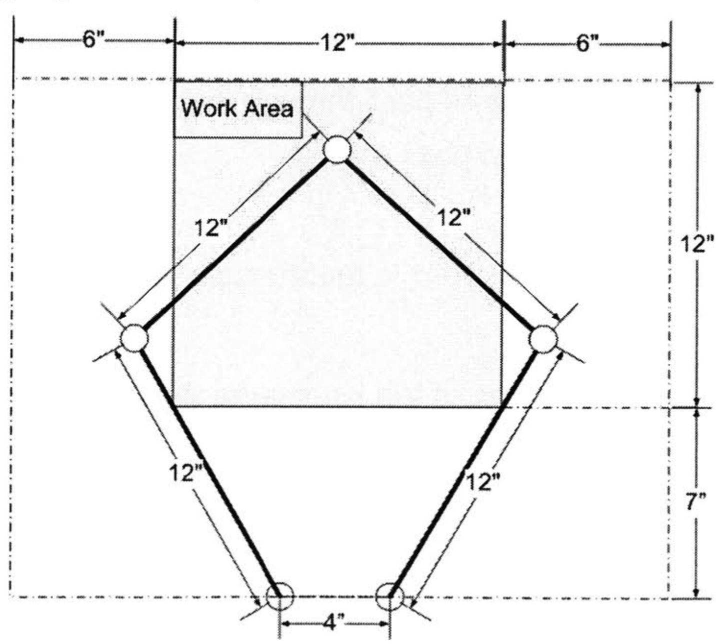

Figure II-7 Foot Print

II.6 Control Scenario

To test the machine a simple PID controller was developed as shown in Figure II-8.

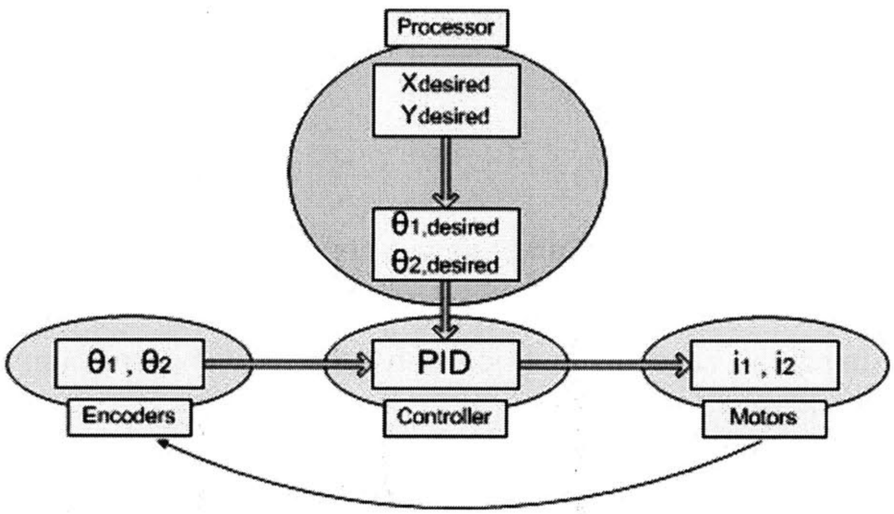

Figure II-8: PID controller designed to test the machine

III FINAL DESIGN

The machine requires both rigid and rotary joints. Two concepts for the rigid joint and four for the rotary one are presented. The reader is guided through a design process to select the concepts that best serve the functional requirements while maintaining simplicity in assembly, ease in fabrication and the use of standard components that are cost effective.

III.1 Rigid Joint Concepts

To rigidly mount the shaft to the mounting arm, two joint concepts were analyzed. The first one is that of a squeeze joint while the second one utilizes a keyless bushing. The squeeze joint concept is a traditional approach for attaining rigid connections, where the shaft is squeezed in both lateral and axial directions, to the mounting arm. Figure III-1 displays a squeeze joint prototype fabricated for a bench level experiment.

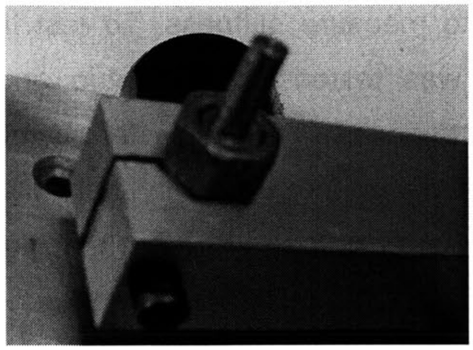

Figure III-1: Squeeze joint prototype

Keyless bushings are components with inner and outer sleeves connected via a collar nut. As the collar nut is tightened, the inner sleeve contracts grabbing the shaft while the outer sleeve expands grabbing the mounting arm. Mounting the keyless bushing requires a roughly finished hole to be drilled in the arm. Keyless bushings have been used to attach axles to wheels; our application is novel to the usage of this hardware. A rigid joint prototype using half inch keyless bushings by Fenner Drives[5] was fabricated as shown in Figure III-2.

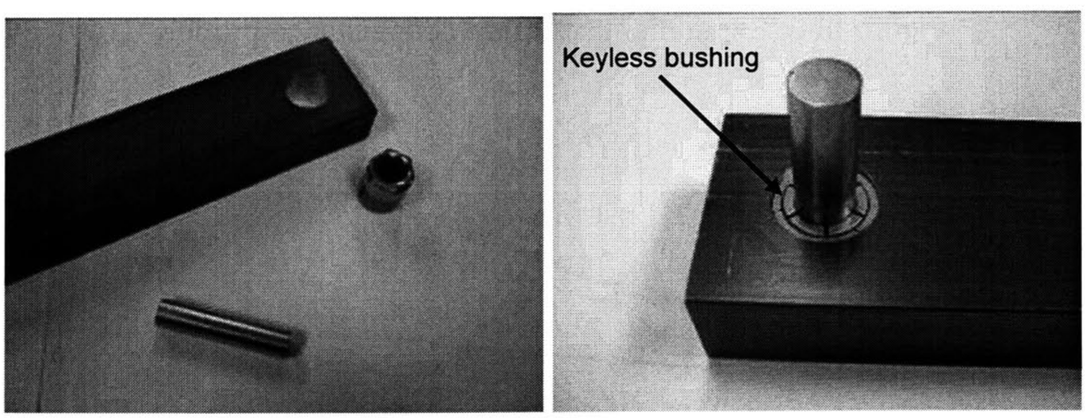

Figure III-2 A rigid joint prototype using half inch keyless bushing

A bench level experiment was set up to compare the load-deflection curves of each concept. Figure III-3 is the machined setup. Capacitance probes hooked up

---

[5] http://www.fennerdrives.com/

to DSpace[6] were used to measure stiffness. To test the accuracy of the test bench, a whole beam was tested on the setup and data obtained where compared with theory. The accuracy of the system came out on the sub micron level. Figure III-4 is a chart with both the experimental and numerical results for the two prototypes. The results from the keyless bushing joint stiffness test were comparable to those from the squeeze joint test. Hence the keyless bushing concept was selected for the rigid joints due to the simplicity in fabrication and assembly it brings forth to the design.

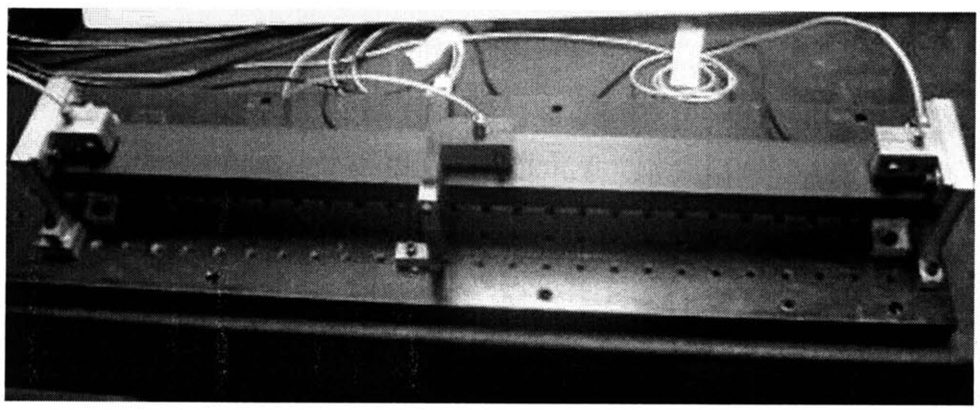

Figure III-3: Experiment setup with capacitance probes

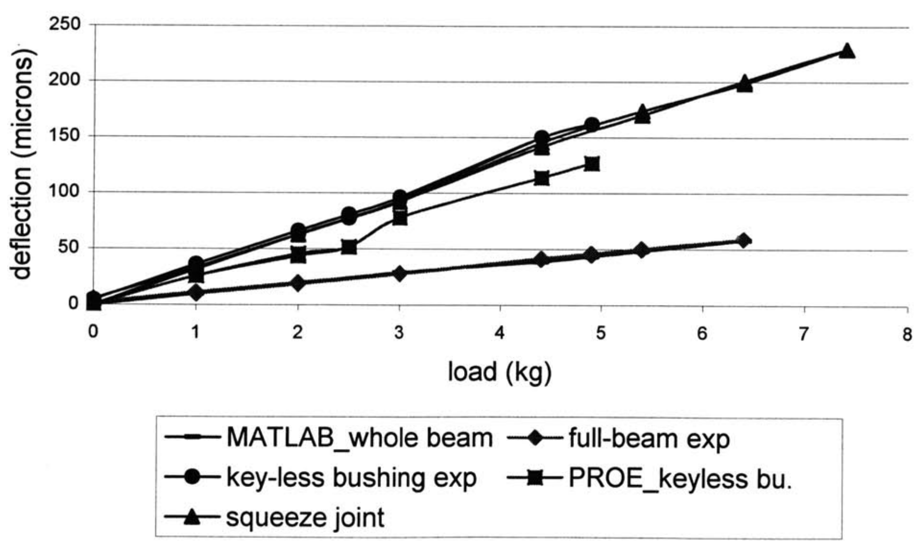

Figure III-4 rigid joint bench level experiments

---

[6] http://www.dspace.com.au/index.shtml

III.2 Rotary Joint Concepts

Four rotary joint concepts where analyzed at the details level. The four concepts will be compared based on the overall stiffness, errors, simplicity and ability to accommodate the cheapest means of preloading the bearings. The concepts are given the names: Cantilever design, Yoke design, C design and Final design.

III.2.1 Cantilever Design

Starting with a simple concept for the joints, a CAD model of the Cantilever design is displayed in Figure I-5. Using off-the-shelf bearings in the machine is one of the design goals. Therefore using 8mm deep groove ball bearings that are available world wide on roller blades became a functional requirement. However, numerical analyses on the cantilever arm design with the 8mm deep groove bearings resulted in large Z-axis deflections. Hence, 12 mm angular contact ball bearings were selected for this design. The angular contact bearings were oriented in a back-to-back position to obtain the greatest stiffness and to maintain thermal stability. The issue of preloading in a simple low-cost manner came into the picture next.

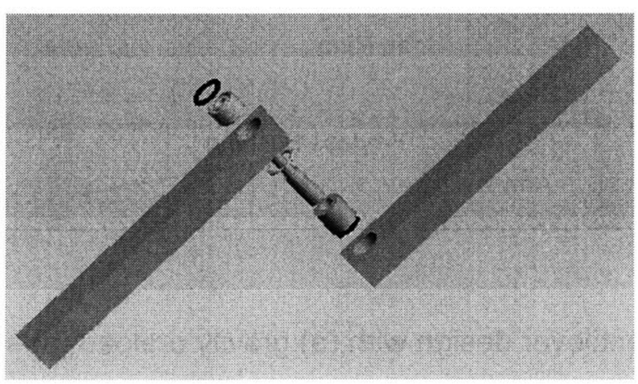

Figure III-5: CAD model of the Cantilever design

Two schemes of preloading where investigated: gravity preloading for the deep groove bearings and spring preloading for the angular contact ones. With gravity preloading the joint and bearings utilize the applied mass on the arm and the force of gravity to adequately remove backlash within the bearings. Gravity preloading is a very convenient method that enhances simplicity in the design and significantly reduces machining time. Figure III-6 (a) is a sketch of the Cantilever joint design with the 12mm bearings preloaded by gravity. Gravity preloading was not adequate in providing the necessary preload for the cantilever design. Spring Preloading on the other hand requires spring forces applied on the bearings. This complicates the design and increases the total machining time. The spring preload scheme in the design used a wave spring to provide the spring force and snap rings or steps machined to the shaft or the arms to properly constrain the bearings. Figure III-6(b) is a sketch of the cantilever design with spring preloading using a wave spring and a snap ring. Wave springs manufactured by Smalley®[7] are a compact design reducing spring cavity by 50% with equal deflection. Calculations for modeling the wave rings and snap rings for 12mm angular contact bearings are presented in Appendix B. In the attempt to reduce the machining cost, the cantilever design for joints was discarded.

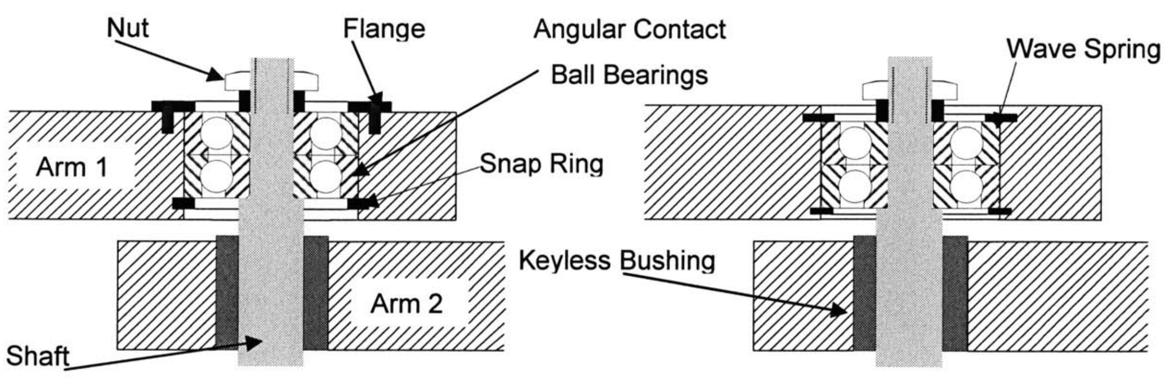

Figure III-6: Cantilever design with (a) gravity preload (b) spring preload

[7] www.smalley.com

III.2.2 Yoke Design

To have a joint stiffer than the cantilever design and that is capable of using the lowest cost 8mm deep groove ball bearings, a yoke model as shown in Figure III-7 was developed. To perform numerical analysis on the Yoke design a CAD model, shown in Figure III-8 was developed. The bearings and keyless bushings where modeled as shown in drawings 8 and 9 of Appendix C and assigned the properties of Aluminum 6061. Numerical analysis results were compared to test data of the actual prototype in Figure III-9. Machining the yoke prototype is expensive, an issue that adds extra cost to the fabrication process.

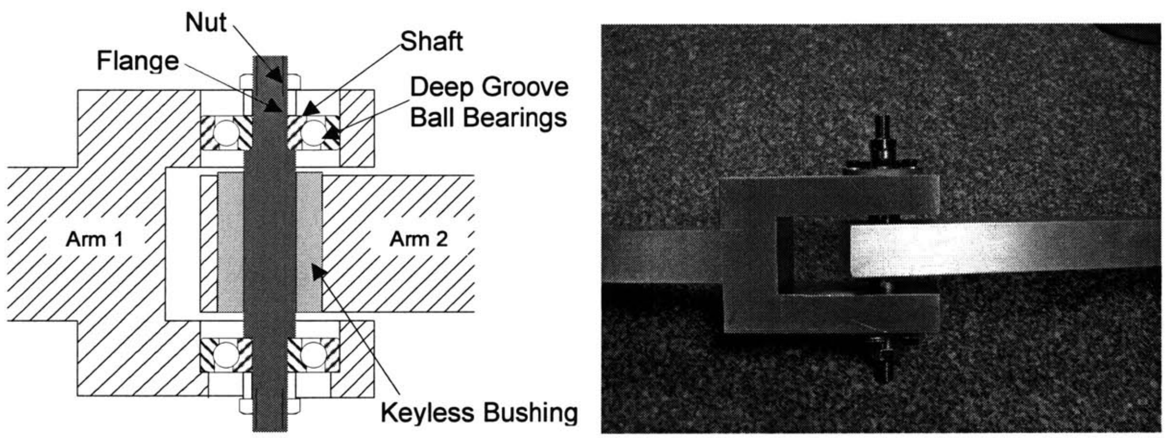

Figure III-7: Yoke joint design

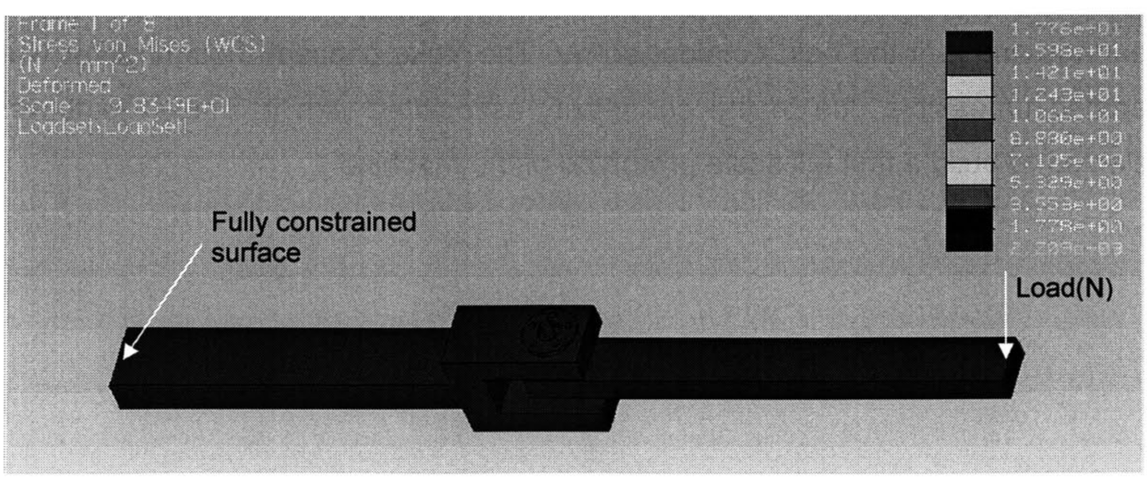

Figure III-8: CAD model of the Yoke joint

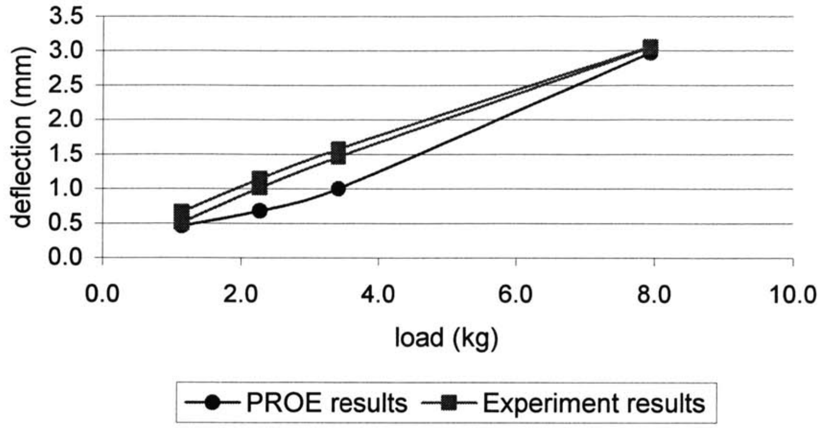

Figure III-9: Yoke design experiment results

III.2.3 C joint Design

To simplify the Yoke joint's machining process while keeping the same level of stiffness in the Z direction, a new C concept as shown in Figure III-10 was designed. To perform numerical analysis on the C design a CAD model, shown in Figure III-11 was developed. The bearings and keyless bushings where modeled as shown in drawings 8 and 9 of Appendix C and assigned the properties of Aluminum 6061. Numerical analysis results were compared to test data of the actual prototype in Figure III-12. The C concept with no precision dimensions, and a good stiffness in the Z axis using the 8mm gravity preloaded bearings, made it the best concept so far. The Yoke concept though stiffer was deemed unfeasible due to the complexity associated with it. The C joint was selected to build a first full scale prototype of the machine.

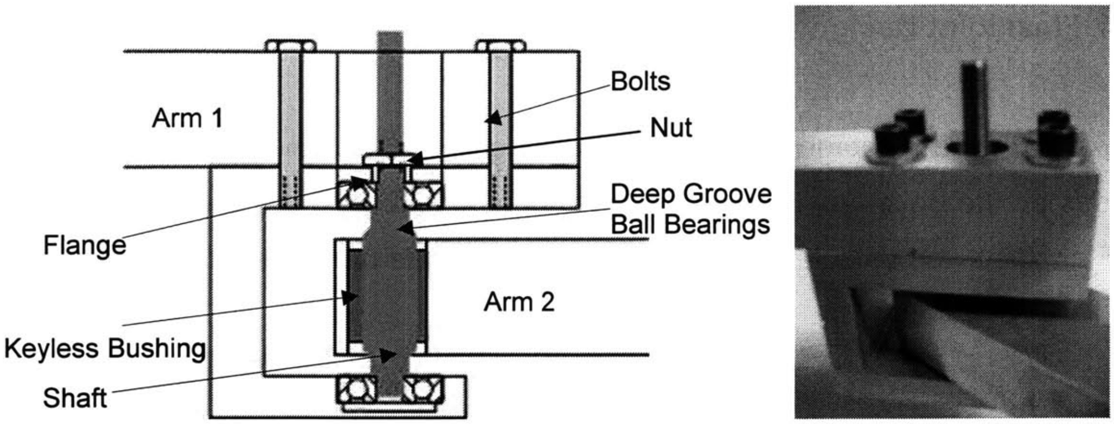

Figure III-10: C joint design

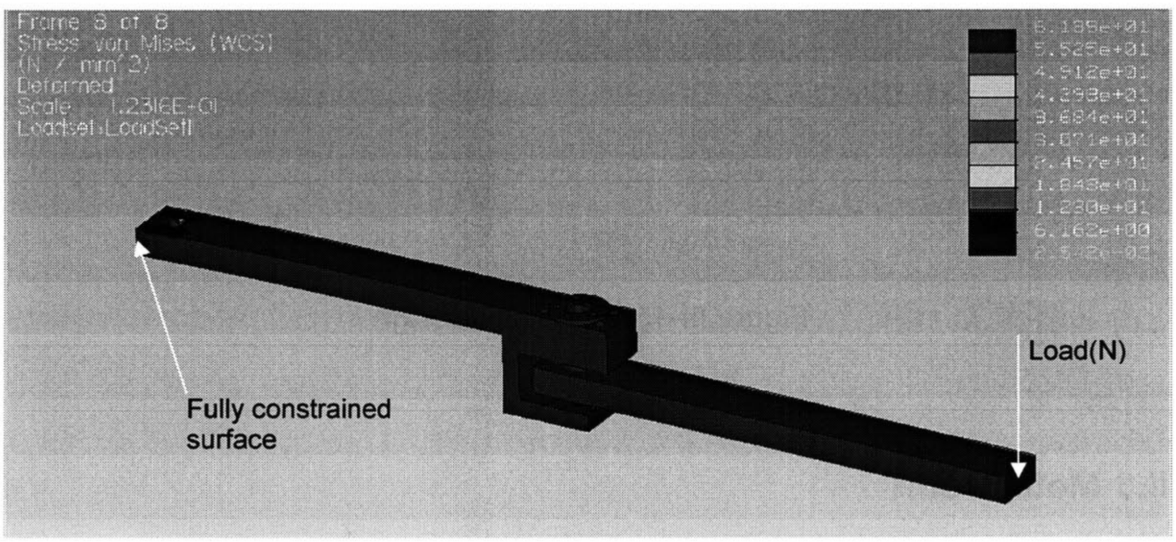

Figure III-11: CAD model of the C joint

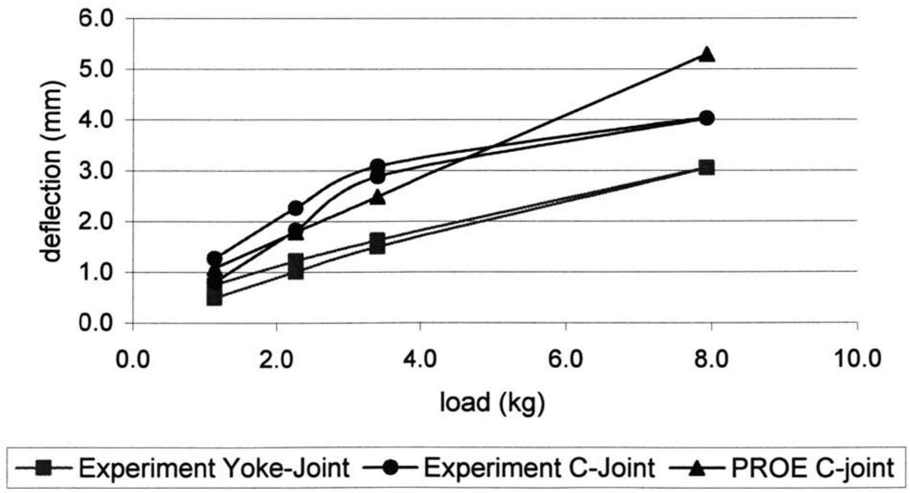

Figure III-12: Deflection Tests C joint vs. Yoke joint

III.2.4 Final joint Design

To take further advantage of gravity preloading in the C joint while reducing the stresses on the bolts, an inverted C joint was modeled as shown in Figure III-13. The Final joint was selected to build a second full scale prototype of the machine.

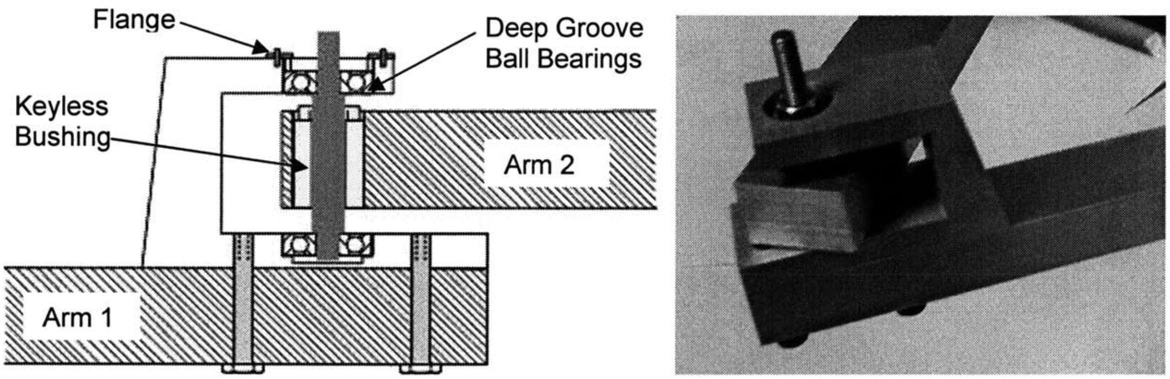

Figure III-13: Final joint design

III.3 Motor Joint

III.3.1 Motor shaft connection

In the first prototype, the concept of a squeeze joint is used to couple the motor's output shaft and the driven arm. A half inch shaft is adhesively bonded with Loc-Tite to the motor, and then squeezed in both lateral and axial directions relative to the mounting arm. The setup is shown in Figure III-1. The squeeze joint on the motor output shaft did not provide enough stiffness in the Z axis. As a result a modified version of the Final joint was used to couple the motor's output shaft to the driven arm. Figure III-14 is a CAD model of the motor's connection.

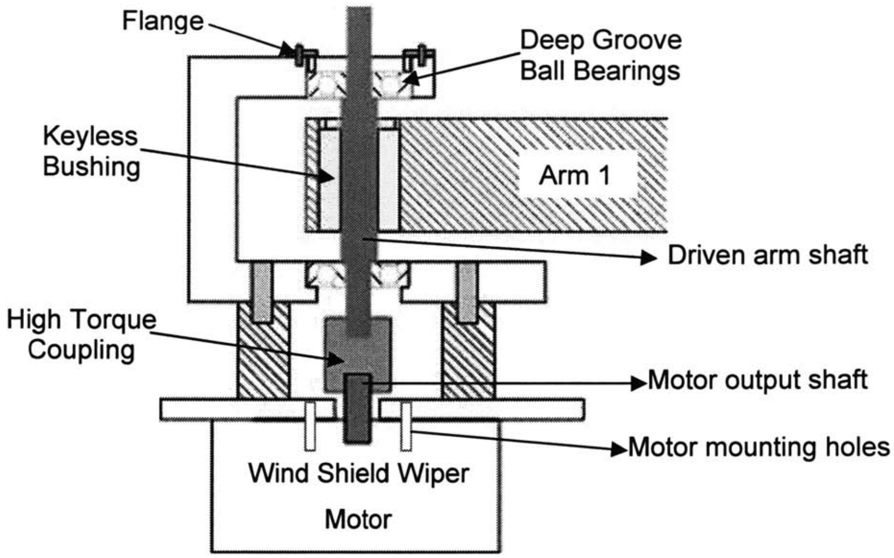

Figure III-14: Motor shaft / Driven arm connection

To simplify the fabrication process, very few precise dimensions where required in the parts' specifications. Hence misalignment between various blocks of the machine was eminent. To account for such misalignments between the motor's output shaft and the driven arm's shaft, the motor's mounting holes where made slightly bigger so that motor can be moved around until perfect alignment between the two shafts is achieved via a rigid coupling designed and fabricated specifically for this task. Figure III-15 is a photo of the machined rigid coupling. Figure III-16 is a photo of the machined motor joint.

Figure III-15: Machined rigid alignment coupling for manufacturing assembly

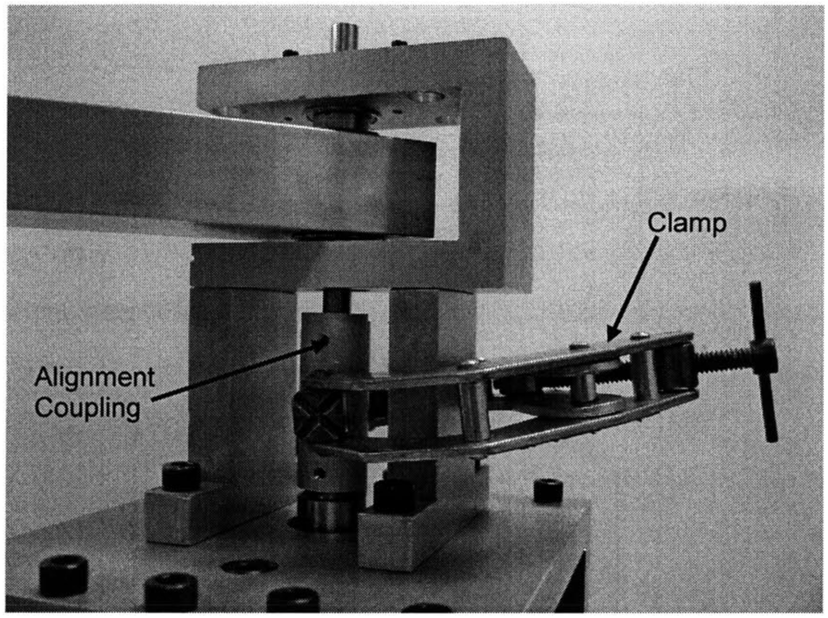

Figure III-16: Motor joint machined with the shafts being aligned

A CNC code was developed to machine shafts that precisely fit to the motors almost square output shaft cross-section. A photo of a fabricated shafted is displayed in Figure III-17.

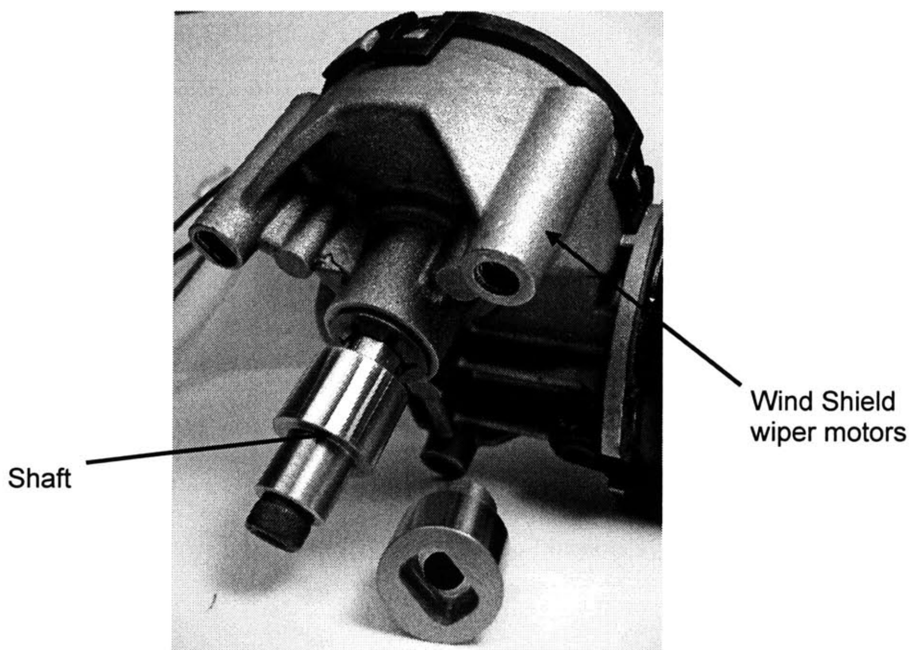

Figure III-17: Shafts that fit tight to the wind shield wiper motor's output shaft

III.4 Couplings

The output shaft from the motor-gear combination cannot handle significant direct radial loads. That was obvious when the squeeze joint concept in the Motor Joint failed. Radial shaft loads cause bending moments which decrease efficiency, stall the motor and lead to early failure of the transmission. To obtain sufficient stiffness at a high performance, a high torque coupling should be used to connect the motor output shaft to the driven arm's shaft. Helical beam couplings, high torque couplings and flexure type couplings are discussed next.

III.4.1 Helical Beam Couplings

Helical beam couplings are often used to transmit rotation from one shaft to another. The shaft coupling's simple one piece construction discards all forms of friction wear within its design, while ensuring a zero-backlash and a no torque-loss operation. Cyclic vibration caused by off-center loading is reduced due to the shaft clamping squeeze type arrangement being incorporated into the single design. However, one of the main obstacles in high-torque applications is one of torsional deformation due to the coupling's modest torsion stiffness. The stiffest helical beam couplings in the size range available can handle operating torque of 4Nm. However, joint torques of 10 Nm are not unusual. Figure III-18 is a photo of the helical beam couplings.

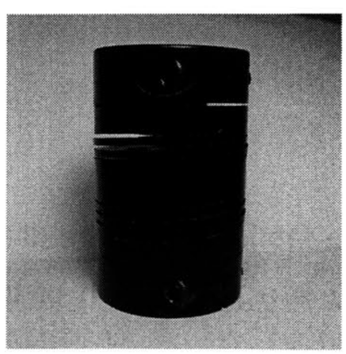

Figure III-18: Helical beam couplings

III.4.2 High Torque Couplings

Renbrandt[8] couplings are especially designed for precision instruments, robotics and encoder drives. Their features include: zero backlash, low inertia, torsional rigidity, uniform velocity, no friction and a long life. The couplings have an accurate concentricity that is unaffected by dust or corrosive atmosphere. The high torsional stiffness of those couplings is due to discs with hubs mounted at 90° with respect to each other. The optimum design for high torque necessitates a compromise in increased radial stiffness that diminishes the coupling ability to handle shaft misalignments. Figure III-19 is a photo of the Renbrandt coupling purchased for the machine. Those couplings are inexpensive to purchase and overcome a peak torque of 88Nm as opposed to a 9Nm peak torque with the same size helical beam ones.

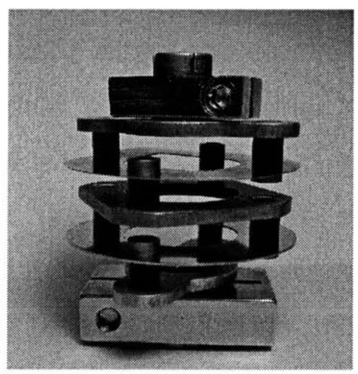

Figure III-19: Renbrandt high torque coupling

III.5 XY Stage Prototypes

Two full scale prototypes were fabricated. Figure III-20(a) is a CAD model of the full scale Prototype I and (b) is a photograph of the fabricated model. Figure

[8] http://www.renbrandt.com

III-21(a) is a CAD model of the full scale Prototype II and (b) is a photograph of the fabricated model.

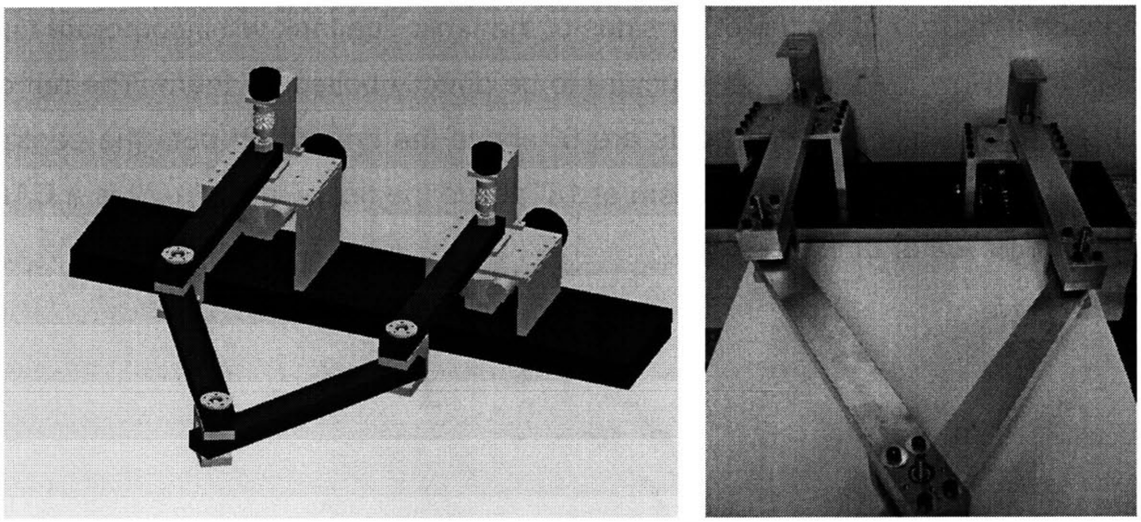

Figure III-20: (a) CAD model, (b) Photo of Prototype I

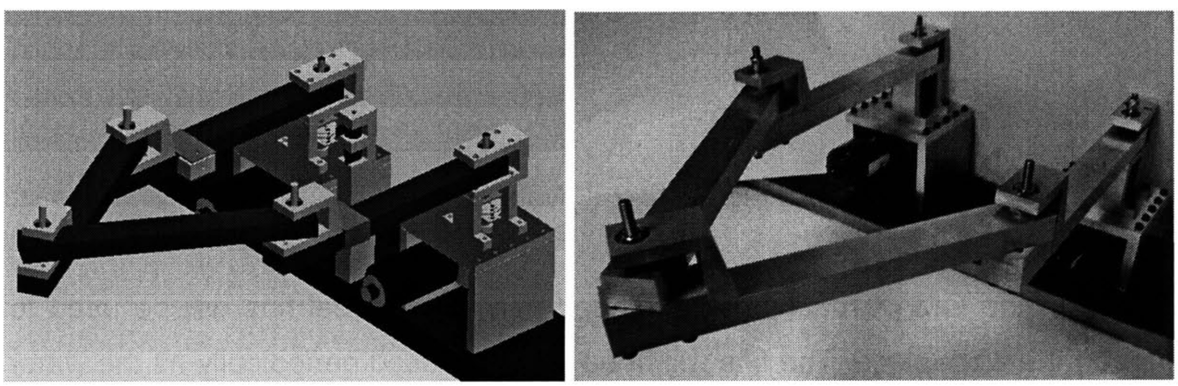

Figure III-21: (a) CAD model, (b) Photo of Prototype II

III.6 Water Tank

All abrasive water jet cutters require a tank full of water at their base to receive the jet of water and abrasive, reduce noise and eliminate the mess from the process by having the part under the water level. This water tank design is based on a tank previously designed by Varela and Slocum. [8] The tanks are to be cast out of polymer concrete using a two part mold with a parting line at the tank's rim. To create space on the front side of the tank a draft angle of 10° was used as opposed to a 3° draft on the other sides of the tank. The tank will incorporate two posts that allow the XY stage structure to be directly bolted on them. The rim of the tank is 30" high and the posts are 6" above the rim, which puts the central plane of the parallel arm mechanism at 18" above the rim. Figure III-22 is a CAD model of the water tank.

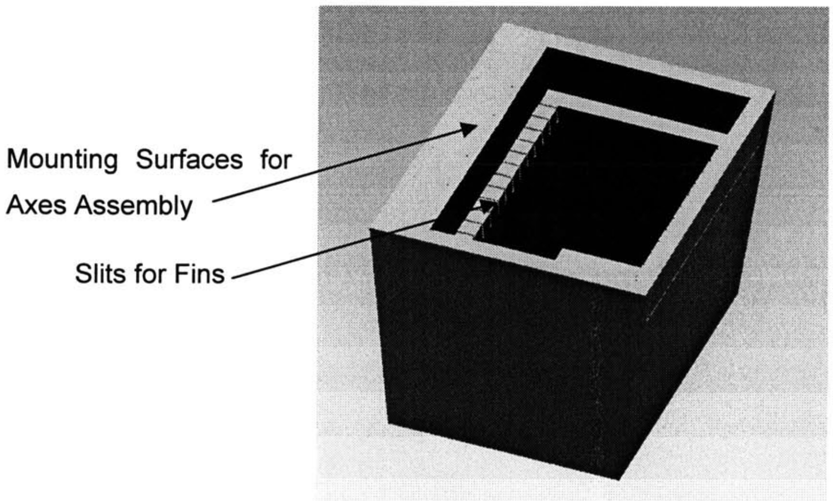

Figure III-22: Water tank

Based on the OMAX machine, hot-dipped galvanized steel fins will be used to support the work piece. The fins will need to be replaced periodically as the water jet cuts through them with time. The slots for the fins will be designed into the tank mold so that no additional hardware will be needed to hold the fins in place. [8].

III.7 Encoders

III.7.1 Rotary Encoders

Rotary encoders convert shaft rotation into square wave output pulses which are then digitized to indicate position, velocity, and direction. They mount to rotating shafts of motors, conveyors, and measuring wheels. An encoder's resolution is measured in cycles per revolution. Due to the mechanical components in such encoders, the prices associated with them tend to be high in the range of $100 to $300 for a resolution of 1000 to 2000 lines per revolution. Two rotary encoders are used in the first prototype and are connected to the output shaft via a helical beam coupling. Flexible couplings are an essential hardware to use in such cases due to the encoder's incapability to handle radial loads and machining misalignments. Figure III-23 is a model of the motor output shaft connected to the encoder. Rotary encoders have their own shaft and support bearings, Modular encoders on the other hand use the machine's existing shafts and bearings as discussed in the next section.

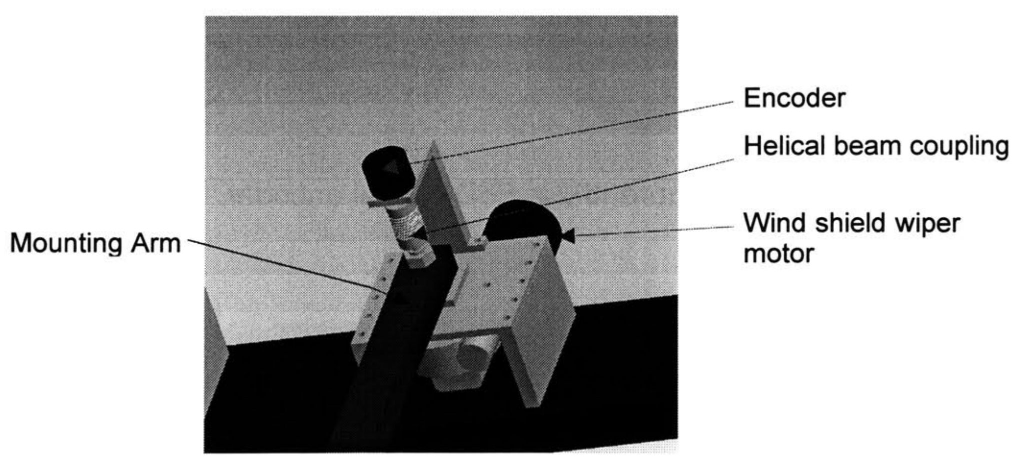

Figure III-23: Encoder mounting model

III.7.2 Modular Encoders

Modular encoders offer a high resolution up to 2048 cycles per revolution for an affordable price of \$50 to \$80. A quote from *US-Digital®* [9] on a simple and low cost optical kit encoder (E6D) made it ideal for this application. E6D is a non-contacting rotary to digital position feedback device designed to easily mount to and dismount from an existing shaft. The internal monolithic electronic module converts the real-time shaft angle, speed, and direction into TTL-compatible outputs. The kit consists of five parts: base, cover, hub/code wheel, module, and the internal differential line driver. The base and cover are made of rugged 20% glass filled polycarbonate. The hub/code wheel adapts to the 8 mm diameter of our shafts. Figure III-24 is a photo of the E6D modular encoder.

Figure III-24: E6D optical encoder. [10]

[9] http://www.usdigital.com

[10] http://www.usdigital.com

III.8 Amplifiers

Searching for amplifiers that are small in size, easy to use, low in cost and based on the surface-mount technology led to *Advanced Motion Controls (AMC)®* [11]. The 25A Series PWM servo amplifiers are designed to drive brush type DC motors at a high switching frequency. An LED indicates the operating status. Over-voltage, over-current, over-heating and short-circuits across motor, ground and power leads are protected for in the models. The models interface with digital controllers such as DSpace in our case. Loop gain, current limit and input gain are adjusted using potentiometers. Figure III-25 is a photo of the 25A8 amplifier selected for our application.

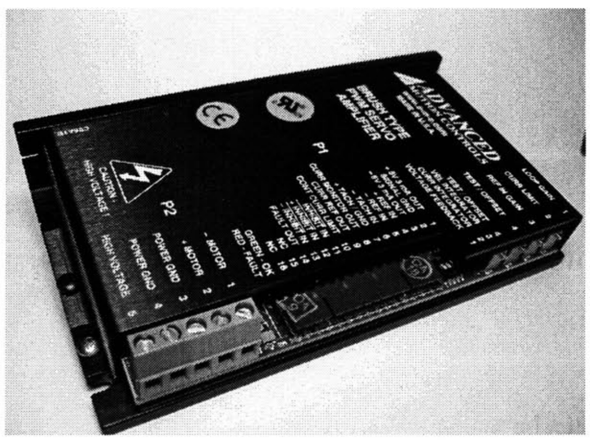

Figure III-25: 25A8 Amplifier by AMC

III.9 Joint Sealing

Due to the dirty working environment in abrasive water jet cutting, all the joints had to be sealed from splashing water and abrasive. This was accomplished

[11] http://www.advancedmotioncontrols.com

using square bellows surrounding every joint. The smallest standard square bellows in the market come 12" when extended and 0.67" when contracted. Bellows selected for the machine are made from Hypalan-Coated polyester with a 0.02" wall thickness, an outer dimension of 4.5"x4.5" and an inner dimension of 2.5"x2.5". Aluminum mounting flanges are bought separately to provide a rigid edge support for the bellows. Two square plates where designed to clamp on the arms of the machine and support the bellows by mounting the bellows flanges to the plates' rims. The assembly is shown in Figure III-26.

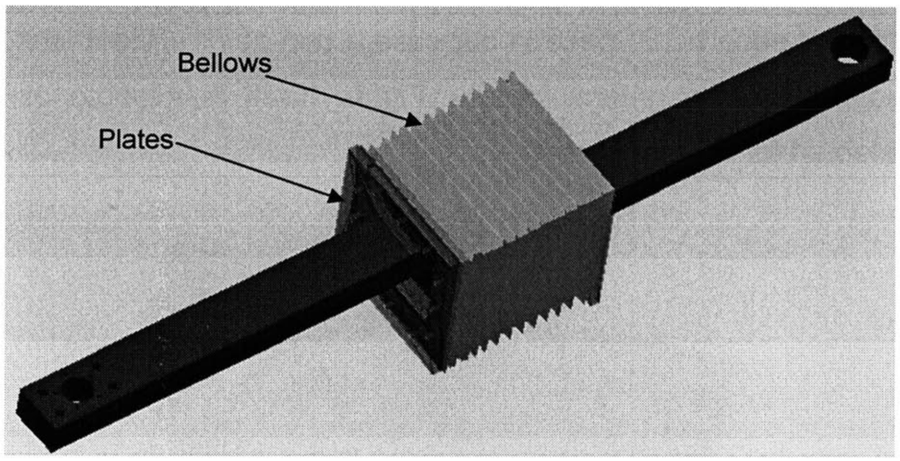

Figure III-26: Assembly for sealing the joints

III.10 Bill of Materials

Table 6 lists all the parts required to build the small abrasive water jet cutter with their quantities, retailers' part numbers, prices, and machining costs. From the list the total price for the machine's mechanical structure and control scenario is estimated at $1219.

The mechanical structure of the abrasive water jet cutter is an assembly of 53 components; the components consist of 12 different parts. All machined parts can be fabricated at a tolerance of 0.005", except for the two shafts that mount to the optical encoders whose tolerance must be less then 0.002". The machine is very simple to assemble and the only tools required for the task are a set of Allen keys and an English ranch. The machine will be sold in boxes and customers are expected to perform the assembly on their own.

The quoted costs for all 53 components of the machine are overpriced at a safety margin of 5 to 10%. The actual prices after appropriate negotiations with the vendors for buying large stocks should be at least 5% less. The cost to build the machine almost matched the functional requirement for a $1500 machine.

Qty	Description	Price	Total Price
McMaster (www.mcmaster.com)			
10	8mm deep groove ball bearing (McMaster #5972k66)	$3.8	$38.0
5	16mm quick mount keyless bushing (McMaster #2298k12)	$28.4	$142.0
1	16mm metric 1070 steel shaft (McMaster #1482K33) [12]	$36 / 4	$8.5
1	0.75" Metric 1070 Steel (McMaster #1346k36) [11]	$46 / 4	$11.5
1	1" x 1.5" Al 6061 rod (McMaster #8975k132)	$44	$44
1	1.5" thick Al 6061 (McMaster #89155k75) [13]	$50 / 2	$87
1	0.5" thick Al 6061 (McMaster #89155k44) [12]	$42 / 2	$21
5	1 ft of Rectangular Bellows (McMaster #9742k29)	$40	$200
1	Loctite 680 Compound (McMaster #91458A87)	$12	$3
US Digital (www.usdigital.com)			
2	Optical Encoders (E6D-2048-315-I-PKG3) [14]	$58	$116
Renbrandt (www.renbrandt.com)			
2	High Torque Couplings (C31-C50-C-HT)+(A101-14+A101-18)	$55	$110
American Motion Controls (www.a-m-c.com)			
2	Series 25A brush DC motors (25A8)	$100	$200
Machining Costs			
All parts can be machined at approximately 6 hours		$20/hr	$120
Tank		~$500	$500
Motors		$50 x 2	$100
	Estimated Cost of Machine		**$1219**

Table 6: Bill of Materials and total cost of the machine

[12] Shaft enough for 4 machines

[13] Plate enough for 2 machines

[14] Price based on buying a stock of 100 pieces

IV CONCLUSION

This thesis presents the design and fabrication of a low cost XY stage for abrasive water jet cutting from the specification of functional requirements, to concept generation, prototype testing to final design of the whole machine. Figure IV-1 is the CAD model of the finished machine.

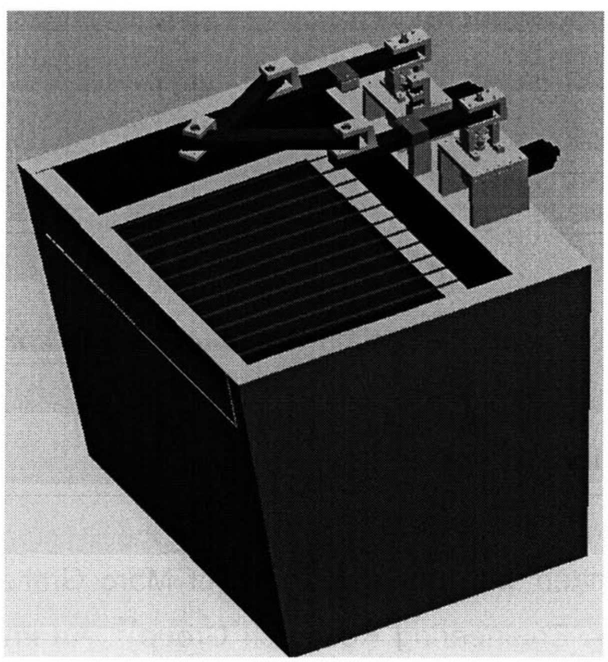

Figure IV-1: Finished machine

A $\theta\theta$ parallel drive stage was designed and fabricated for the nozzle relocation; the structural design's creativity was prevalent in the success it attained to significantly cut down the costs. The final design met a set of functional requirements defined in the introduction and followed through out the design process. The functional requirements included a work area of *310mmx310mm*, a cost of *$1500*, a resolution of *0.5mm*, a maximum acceleration of *0.1 g* and a top speed of *10mm/sec*. We got close in making our vision of abrasive water jet cutters being stacked on shelves of stores like Walmart® a reality, by designing the Mechanical parts of the machine fit a (40x30x13 cm^3) box as shown in Figure IV-2.

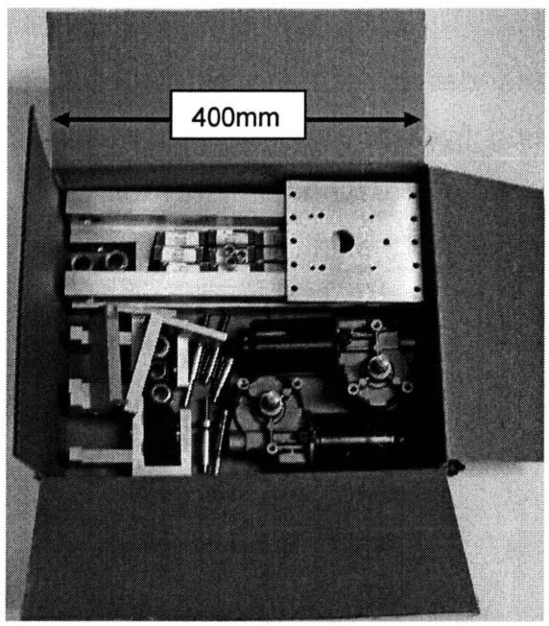

Figure IV-2: Mechanical parts fit a (40x30x13 cm^3) box

Benefits for Education

This section was written with the assistance of Marc Graham, a colleague of mine in the Precision Engineering Research Group[15]. An important part of this project is to incorporate the design process into an educational experience. Low

---

[15] http://pergatory.mit.edu

cost precision machining can serve a development-of-skills role similar to role of bridging the "digital divide" provided by low cost computing. Technology developments have allowed us to increase processing power, while decreasing the cost of computers; as the cost of computers continues to drop, more of the world's population can benefit from them. Advances in precision machine design has also provided an opportunity for us to create low cost precision machines, allowing more of the world's population to benefit from their use.

Part of being a good designer is having first-hand knowledge of how components are manufactured. In teaching design, students who have access to precision machines are able to straightforwardly conceive and develop advanced designs, not dissimilar to how students with access to super computers are able to complete highly complex computations. Not only do precision machines improve education, they improve economies by providing a means for people to create new products for commerce. As with other technological developments, precision machines play an important role in preparing students to become masters of their own destiny and increase the potential for them to create a productive world economy. We believe that this is a key to helping the Middle East evolve economically.

It is our intention to have low cost water jets made available to schools and universities all over the world. We hope to be able to work with third-world universities to build the machine at the universities by students. This process not only introduces people to the uses of precision machines, but also gives insight into the development and interworkings of such machines.

Future work

Further optimizations are being conducted and more product development need to be done before we have a product ready to be sold. A prototype version of the system has been fabricated and currently a simple controls scheme is being used to test the machine's performance. The prototype will be tested with a water jet cutting system supplied by OMAX®. A mini nozzle with high precision will be supplemented with a 5KW pump. In the end the the OMAX control software will be modified to control the mechanism that will be actuated by the wind shield wiper motors.

REFERENCES

[1] www.waterjets.org

[2] A. Slocum, *"Precision Machine Design"*, SME Publishing, 1992.

[3] Assada and Youcef-Toumi, *"Direct Drive Robots"*, MIT Publishing 1987

[4] Assada, Canade and Takeyama, *"Control of a Direct Drive Arm"*, ASME Journal of Dynamic Systems, Measurement and Control, Vol. 105, 1983

[5] Smalley Catalogue

[6] Chung, Y.H., and Lee, J.W, *"Design of a New 2DOF Parallel Mechanism"*, Intl. Conference on Advanced Intelligent Mechatronics Proceedings, PP.129-134, (2001).

[7] Cloy, D., *"Some Comparisons of Serial Driven and Parallel Driven Manipulators"*, Robotica, Vol. 8, PP: 355-362, 1990.

[8] P. Varela, *"The Design of a Small and Inexpensive Abrasive Waterjet Cutter"*, MIT SM thesis, 1999

APPENDIX A

Serial Drive Mechanism

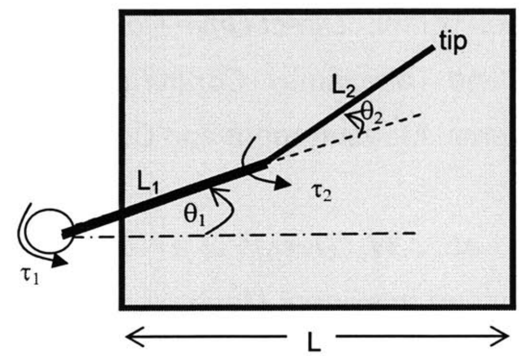

Figure IV-3: Sketch of the 2 link serial drive manipulator.

Kinematics:

$$X_{tip} = L_1 \cos\theta_1 + L_2 \cos(\theta_1 + \theta_2)$$
$$Y_{tip} = L_1 \sin\theta_1 + L_2 \sin(\theta_1 + \theta_2)$$

By differentiating the above equations and applying a certain angular error of: $\partial\theta_1, \partial\theta_2$, the error translated to the tip will be:

$$\partial X_{tip} = -L_1 \sin(\theta_1)\partial\theta_1 - L_2 \sin(\theta_1 + \theta_2)(\partial\theta_1 + \partial\theta_2)$$
$$\partial Y_{tip} = L_1 \cos(\theta_1)\partial\theta_1 + L_2 \cos(\theta_1 + \theta_2)(\partial\theta_1 + \partial\theta_2)$$

Running a MATLAB script that simulates the above 2 equations generates the mechanism's sensitivity to angular error (Abbe error).

Dynamics:

$$\omega_1 = \dot{\theta}_1, \dot{\omega}_1 = \ddot{\theta}_1$$

$$v_{c1} = \begin{bmatrix} -l_{c1}\dot{\theta}_1 \sin\theta_1 \\ l_{c1}\dot{\theta}_1 \cos\theta_1 \end{bmatrix} \rightarrow a_{c1} = \begin{bmatrix} -l_{c1}\ddot{\theta}_1 \sin\theta_1 - l_{c1}\dot{\theta}_1^2 \cos\theta_1 \\ l_{c1}\ddot{\theta}_1 \cos\theta_1 - l_{c1}\dot{\theta}_1^2 \sin\theta_1 \end{bmatrix}$$

l_{c1}, l_{c2} and l_{c3} are distances from the joints to the respective links.

$$a_{c2-1} = -l_1\ddot{\theta}_1 \sin\theta_1 - l_1\dot{\theta}_1^2 \cos\theta_1 - l_{c2}\ddot{\theta}_1 \sin(\theta_1+\theta_2) - l_{c2}\dot{\theta}_1(\dot{\theta}_1+\dot{\theta}_2)\cos(\theta_1+\theta_2) -$$
$$l_{c2}\ddot{\theta}_2 \sin(\theta_1+\theta_2) - l_{c2}\dot{\theta}_2(\dot{\theta}_1+\dot{\theta}_2)\cos(\theta_1+\theta_2)$$

$$a_{c2-2} = l_1\ddot{\theta}_1 \cos\theta_1 - l_1\dot{\theta}_1^2 \sin\theta_1 + l_{c2}\ddot{\theta}_1 \cos(\theta_1+\theta_2) - l_{c2}\dot{\theta}_1(\dot{\theta}_1+\dot{\theta}_2)\sin(\theta_1+\theta_2) +$$
$$l_{c2}\ddot{\theta}_2 \cos(\theta_1+\theta_2) - l_{c2}\dot{\theta}_2(\dot{\theta}_1+\dot{\theta}_2)\sin(\theta_1+\theta_2)$$

Solving the Newton Equation result in:

$$\tau_1 = H_{11}\ddot{\theta}_1 + H_{12}\ddot{\theta}_2 - h\dot{\theta}_2^2 - 2h\dot{\theta}_1\dot{\theta}_2 + G_1$$
$$\tau_2 = H_{22}\ddot{\theta}_2 + H_{12}\ddot{\theta}_1 + h\dot{\theta}_1^2 + G_2$$
$$H_{11} = m_1 l_{c1}^2 + I_1 + m_2(l_1^2 + l_{c2}^2 + 2l_1 l_{c2}\cos\theta_2) + I_2$$
$$H_{22} = m_2 l_{c2}^2 + I_2$$
$$H_{12} = m_2 l_1 l_{c2}\cos\theta_2 + m_2 l_{c2}^2 + I_2$$
$$h = m_2 l_1 l_{c2}\sin\theta_2$$
$$G_1 = m_1 l_{c1} g\cos\theta_1 + m_2 l_{c2} g\cos(\theta_1+\theta_2)$$
$$G_2 = m_2 l_{c2} g\cos(\theta_1+\theta_2) + \Psi$$
$$\psi = func(extra\_parameters)$$

The above can be used to simulate the system under various control algorithms. Running a MatLab script that simulates the above set of equations generates the mechanism's torque requirements.

Parallel Drive Mechanism:

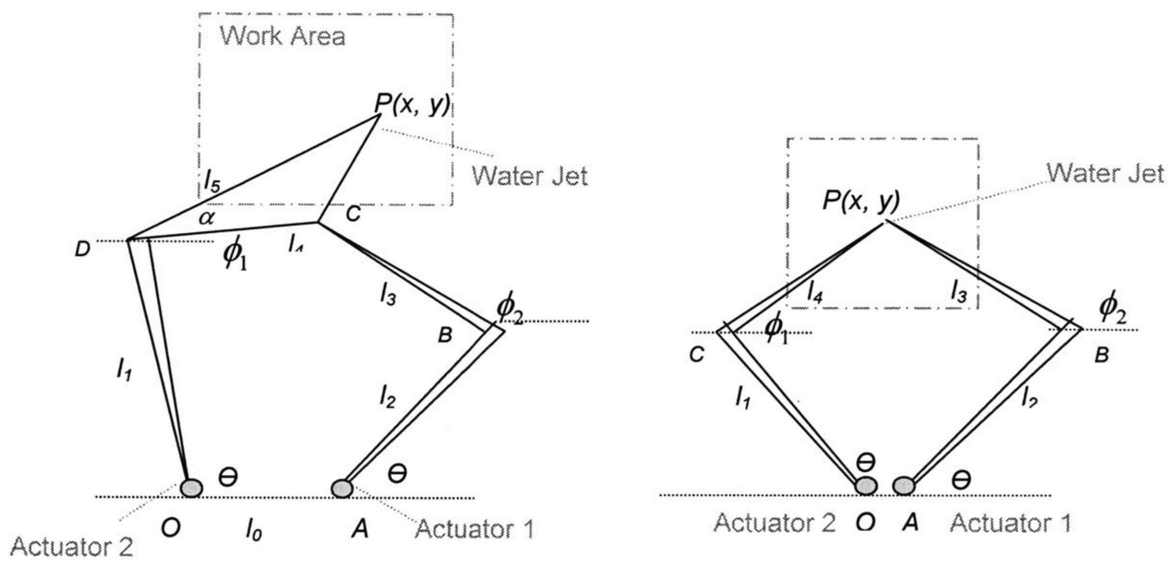

Figure IV-4: Architecture of the proposed mechanism:

The architeture of the 2 DOF proposed design is sketched in Figure IV-4. Planar manipulators with 2DOF can be one of 20 different combinations [7]. However this number is reduced to one with the actuators being rotary and attached to the ground. The closed 5-bar linkage can be considered as a parallel plane manipulator, composed of the two serial sub-chains O-D-P and O-A-C-P (Figure IV-4), connecting the end effecter P to the base. In our case $\alpha = 0$ and $l_4 = l_5$.

Kinematics:

$$x_{tip} = l_1 \cos\theta_1 + l_5 \cos\phi_1$$
$$y_{tip} = l_1 \sin\theta_1 + l_5 \sin\phi_1$$

$$\phi_1 = func(\theta_1 + \theta_2)$$
$$l_1 \cos\theta_1 + l_4 \cos\phi_1 = l_0 + l_2 \cos\theta_2 + l_3 \cos\phi_2$$
$$l_1 \sin\theta_1 + l_4 \sin\phi_1 = l_0 + l_2 \sin\theta_2 + l_3 \sin\phi_2$$

Solving the kinematics equations one can find all four unknowns θ_1, θ_2, ϕ_1 and ϕ_2. [3][6]. The kinematic equations have four solutions that lead to the same tip position. Different modes result in different endpoint Force-Speed characteristics. Figure 3 sketches the four manipulator modes for the same tip location. Whenever the system goes from one mode to another it passes through a singularity. The best way to avoid singularities is to have them outside the working area, this way the mechanism operates in one mode at all times. An algorithm to detect the largest working area was set and the result showed that mode1 is the best mode in which to operate.

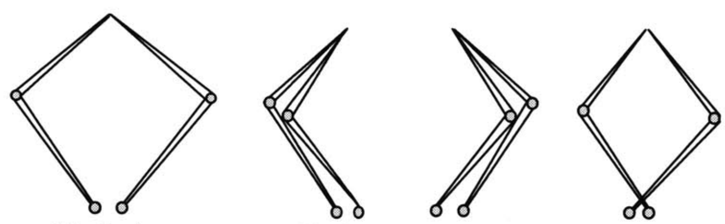

Figure IV-5: Four manipulator modes for the same tip location

The kinematics equations can be used to solve for the Jacobean matrix J.

$$\partial X = J \partial \theta$$

$$J = \begin{bmatrix} J_{11} & J_{21} \\ J_{12} & J_{22} \end{bmatrix}$$

$$J_{11} = -l_1 \sin\theta_1 - \frac{l_1 l_5 \sin(\phi_1 + \alpha)\sin(\theta_1 - \phi_2)}{l_4 \sin(\phi_2 - \phi_1)}$$

$$J_{12} = -\frac{l_2 l_5 \sin(\phi_1 + \alpha)\sin(-\theta_2 + \phi_2)}{l_4 \sin(\phi_2 - \phi_1)}$$

$$J_{21} = l_1 \cos\theta_1 + \frac{l_1 l_5 \sin(\phi_1 + \alpha)\sin(\theta_1 - \phi_2)}{l_4 \sin(\phi_2 - \phi_1)}$$

$$J_{22} = \frac{l_2 l_5 \cos(\phi_1 + \alpha)\sin(-\theta_2 + \phi_2)}{l_4 \sin(\phi_2 - \phi_1)}$$

A MATLAB code was developed to simulate the kinematics, and the impact of angular errors to the final output. For $|J| = 0$ we get three singularity locations at : $\phi_1 + \alpha - \theta_1 = 0$, $\phi_2 - \theta_2 = 0$ that define boundaries between various modes. The third singularity occurs at $\phi_2 - \phi_1 = 0$ and defines the boundary-to-reachable region. The direct kinematic singularity of the mechanism occurs near the boundary of the workspace; hence to investigate the effect of this on the kinematic performance of the mechanism, a manipulability ellipsoid can be plotted. The plot will be non-uniform and anisotropic near the singularity boundary.

Dynamics:

$$H = \begin{bmatrix} H_{11} & H_{21} \\ H_{12} & H_{22} \end{bmatrix}$$

First fix the second actuator at joint 1 we get inertia relative to joint 0:

$$H_{11} = \underbrace{I_1 + m_1 l_{c1}^2}_{*} + \underbrace{I_3 + m_3 l_{c3}^2}_{**} + \underbrace{m_4 l_1^2}_{***}$$

*: Resultant inertia of link 1 about axis of joint B.

**: Because link 3 rotates about B when joint one rotates

***: Mass center of link 4 moves at a constant radius of l_1.

Similarly:

$$H_{22} = I_4 + m_4 l_{c4}^2 + I_2 + m_2 l_{c2}^2 + m_3 l_2^2$$

$$H_{12} = (m_3 l_2 l_{c3} - m_4 l_1 l_{c4}) \cos(\theta_2 - \theta_1)$$

Rθ mechanism

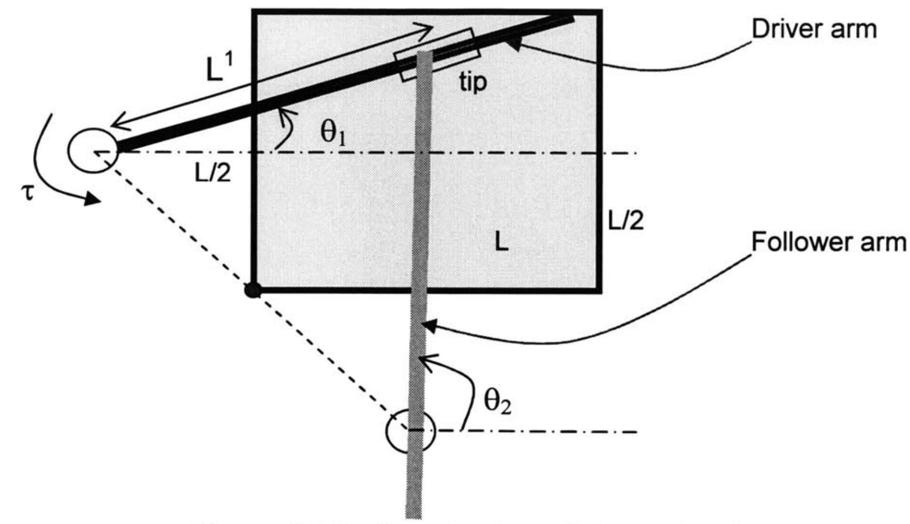

Figure IV-6: Sketch of the Rθ mechanism.

Kinematics

$$X_{tip} = L^1 \cos\theta_1 - L/2 \Rightarrow \dot{X}_{tip} = -L^l \sin\theta_l (d\theta_l)$$

$$Y_{tip} = L/2 + L^1 \sin\theta_1 \Rightarrow \dot{Y}_{tip} = L^l \cos\theta_l (d\theta_l)$$

$$\rightarrow \theta_1 = \tan^{-1}\left(\frac{Y_{tip} - L/2}{X_{tip} + L/2}\right)$$

$$\rightarrow L^1 = \frac{(X_{tip} + L/2)}{\cos\theta_1}$$

$$\rightarrow L^{ll} = \sqrt{(Y_{tip} + L/2)^2 + (X_{tip} - L/2)^2}$$

$$\rightarrow \theta_2 = 90 - \tan^{-1}\left(\frac{X_{tip} - L/2}{L^{ll}}\right)$$

Using the above equations, a simulation was run on MATLAB where the user input the equation of the trajectory $Y_{tip} = f\left(X_{tip}\right)$, and a simulation of the motion is presented. Figure IV-7 is the end position of the machine after the simulation. Note that the trajectory for the tip and the end of the following arm are shown.

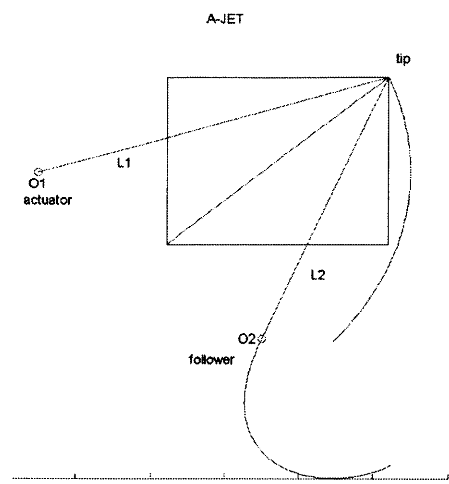

Figure IV-7: Shot from the Ajet simulation

APPENDIX B

A tutorial for designing a spring preloaded system using 12 mm angular contact ball bearings, wave rings and snap rings is presented in this Appendix. All equations and data are referenced in the 2003 Smalley Catalogue. [5]

Materials available for the preloading elements included Carbon Steels, Super Alloys, Stainless Steels and Coppers. Stainless Steel 302 was selected for this application due to the machine's operation in a water environment, the physical properties of the alloy, and its low cost.

Retaining Rings

<u>General:</u>

For a 12mm angular contact ball bearing with a 32mm outer diameter, two retaining rings and one wave ring are available from the Smalley catalogue as shown in Table 7 and 7.

Part Number	Housing Diameter (mm)	Thrust Capacity		Ring Dia. (mm)	Radial Wall (mm)	Ring Thick-ness (mm)	Groove Dia. (mm)	Min. Groove Width (mm)	Turns	Crimp
		Ring Shear (N)	Groove Yield (N)							
DHH-32 Internal, 2-turn, DIN metric series	32.00	33,187	13,256	34.04	2.41	1.14	33.70	1.30	2	Yes
EH-32 Internal, 2-turn, metric series	32.00	36,950	15,880	34.23	2.64	1.27	34.00	1.40	2	Yes

Table 7: Retaining rings. [5]

Part Number	Operates in Bore Diam. (mm)	Clears Shaft Diam. (mm)	Load (N)	Work Height (mm)	Free Height (mm)	Waves	Turns	Wire Thickness (mm)	Radial Wall (mm)	Spring Rate (N/mm)
SSB-0126 Bearing Preload, Single Turn, Overlap Type Wave Springs (Metric Series)	32.00	24.22	89	1.98	3.81	3	1	0.41	3.38	52

Table 8: Wave ring. [5]

The allowable thrust load P_r on the retaining ring in shear is:

$$P_r = \frac{DTS_Y\pi}{K}$$

D: Ring diameter (34.04*mm* in the machine design)

S_Y: Shear yield for stainless steel (137*Ksi*)

K: Safety factor (3)

T: Ring thickness (1.27*mm*)

$\Rightarrow P_r = 9037.2lb = 40.7KN$

However, as permanent groove deformation occurs the ring begins to twist. As the angle of twist increases, the ring begins to enlarge in diameter. Ultimately, the ring becomes dished and protrudes from the groove. Thus the allowable thrust load based on groove shear:

$$P_g = \frac{DdS_Y\pi}{K}$$

D: Ring outer diameter (32*mm* in the machine design)

S_Y: Yield stress for Al 6061 arm (40*Ksi*)

K: Safety factor (3)

d: Groove depth (1.4*mm*)

$\Rightarrow P_r = 2908.7lb = 13.1KN$.

Hence the design will be limited to a thrust load of 13.1KN due to groove deformation.

To assure maximum load capacity it is essential to have square corners on the groove and retained components. Moreover retained components must always be square to the ring groove in order to maintain a uniform concentric load against the retained part. For a shaft diameter less than 1" the maximum radius should be 0.01" as shown in Figure IV-8.

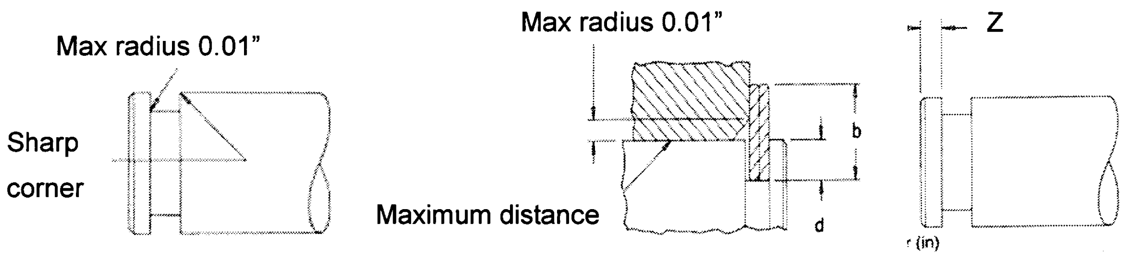

Figure IV-8: Sketches for modeling retaining rings

For the retained components the maximum radius of chamfer allowable on the retained part is equal to $0.5(b-d)=0.5(2.41-1.4)=0.6mm$ as shown in Figure IV-8.

Edge Margin:

The maximum edge margin Z due to shear and bending are:

$$Z_{shear} = \frac{3KP}{S_Y D_G \pi}$$

K=3, P: load=225lb (on the safe side), S_Y=40ksi, D_G=34mm

$$Z_{bending} = \left[\frac{6dKP}{S_Y D_G \pi}\right]^{\frac{1}{2}}$$

K=3, P=225 lb, S_Y=40 ksi, D_G=34mm, d=1mm

Comparing the above 2, it can be concluded that bending is the determining factor for the critical edge margin. $\Rightarrow Z_{critical} = Z_{bending} = 1mm$

Maximum RPM:

Maximum RPM is not an issue since the joints will be operating at low speeds.

$$N=\left[\frac{3600VEIg}{4\pi^2Y\gamma AR_M^5}\right]^{\frac{1}{2}}$$

I : Moment of inertia $tb^3/12$=1.33mm^4,

E : Modulus of elasticity=28x10^{6}psi,

g : Gravity acc=386.4 in/sec^2,

t : Material thickness=1.14mm,

b : Radial wall=2.41mm,

R_M = (D_I+b)/2=17.205mm,

V = (D_G-D_I)/2=1,

$A=tb-.12t^2$ =2.59mm^2,

Y : Multiple turn factor=3.407,

γ : Material density=0.283 lbs/in^3.

Installation Stresses:

$$S_C=\frac{Eb\left(D_o-D_H\right)}{\left(D_o-b\right)\left(D_H-b\right)}=144.4Ksi$$

Minimum tensile strength of the ring material (table from Smalley) = 185Ksi, 80% of 185Ksi= 150Ksi. Since $S_C <$ minimum tensile strength, permanent set is not expected.

Wave Spring

Deflection:

The amount of deflection, δ, in the wave spring can be calculated as follows:

$$\delta=\frac{PKD_m^3}{Ebt^3N^4}\frac{ID}{OD}$$

P : load (150N)

E: Young's modulus (29.5x10^6*Ksi*)

K: Safety factor (1)

b: Size of the radial wall (3.38*mm*)

t: Thickness (0.41*mm*)

N: Number of turns (1)

ID: Inside diameter (24.22mm)

OD: Outside diameter (32mm)

MD: Mean diameter (28.11mm)

$\Rightarrow \delta = 1.8mm$

Preload provided = 89N.

APPENDIX C

Machine Drawings:

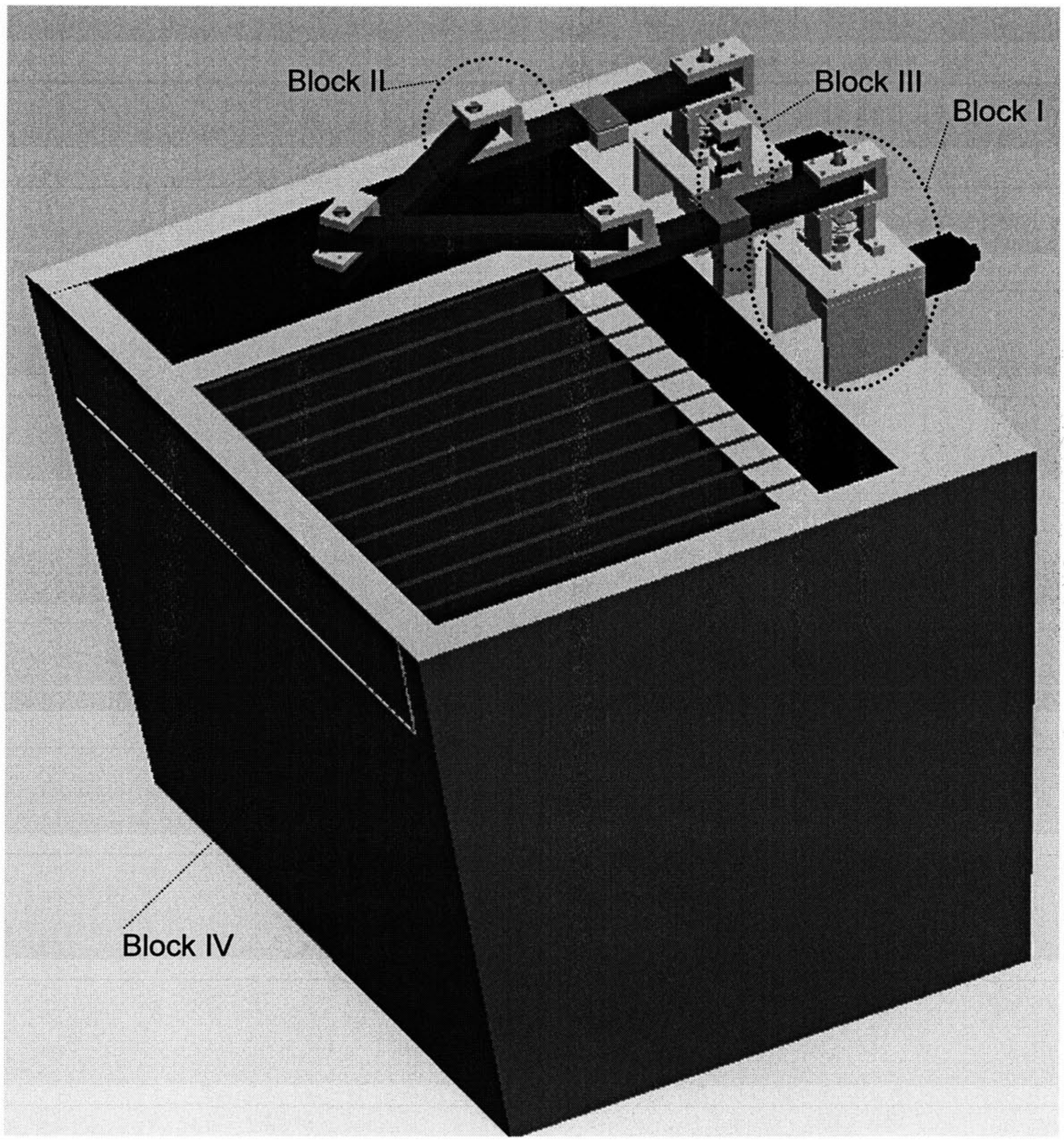

Figure IV-9: Machine drawings

Block I: Motor joint drawings

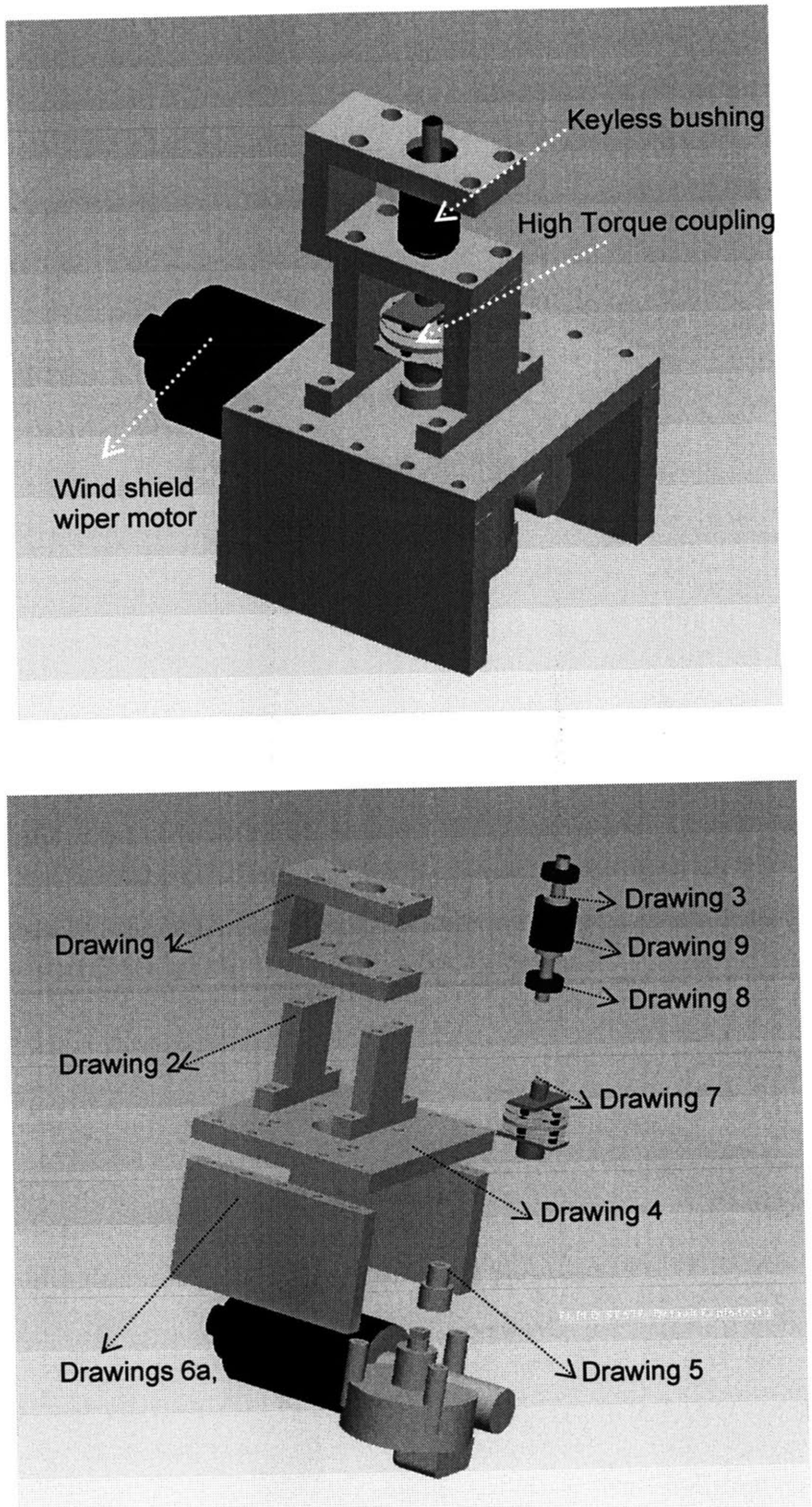

Figure IV-10: Motor joint drawings

Block II: Parallel arms drawings

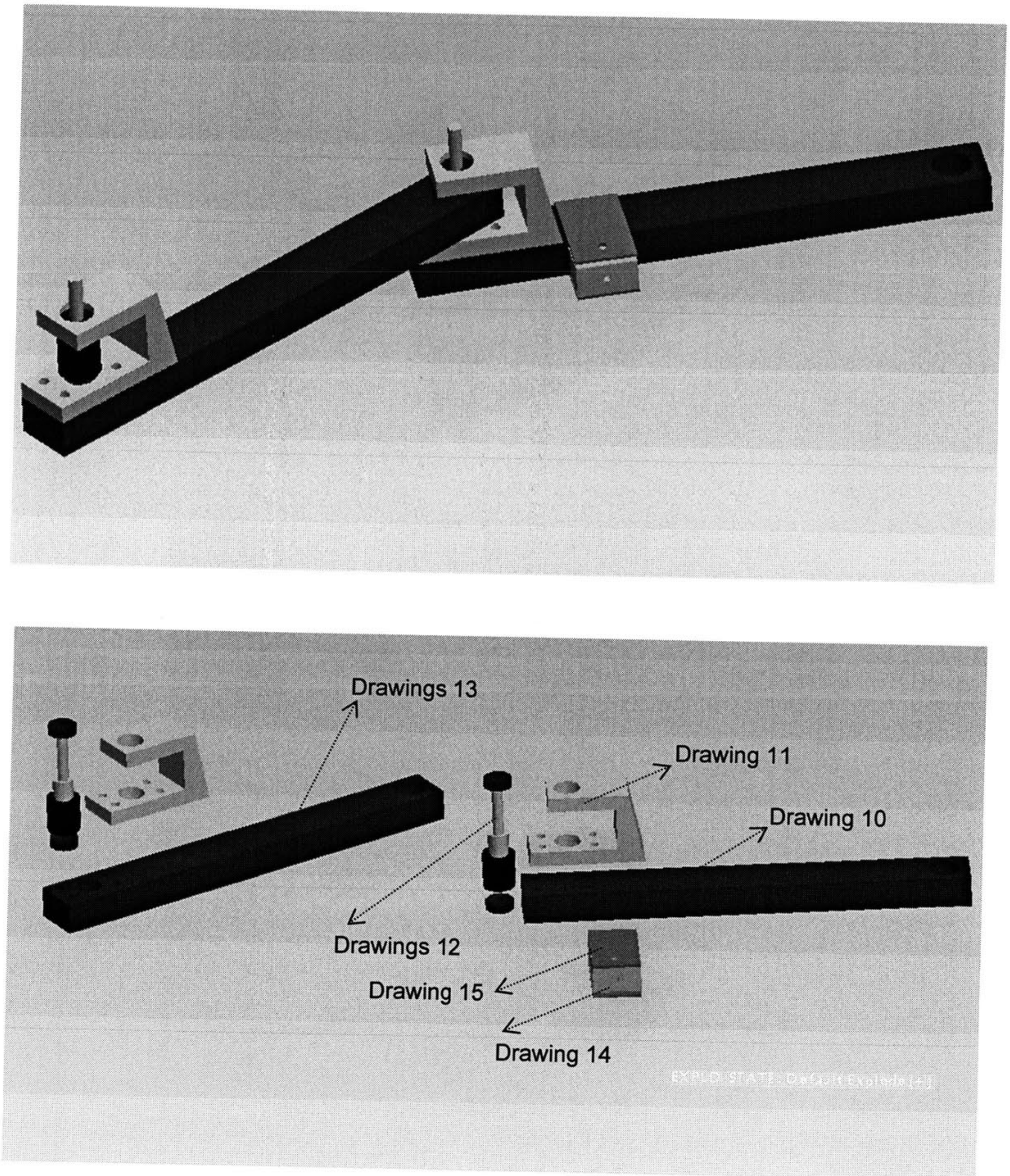

Figure IV-11: Parallel arms drawings

Block III: Preload drawings

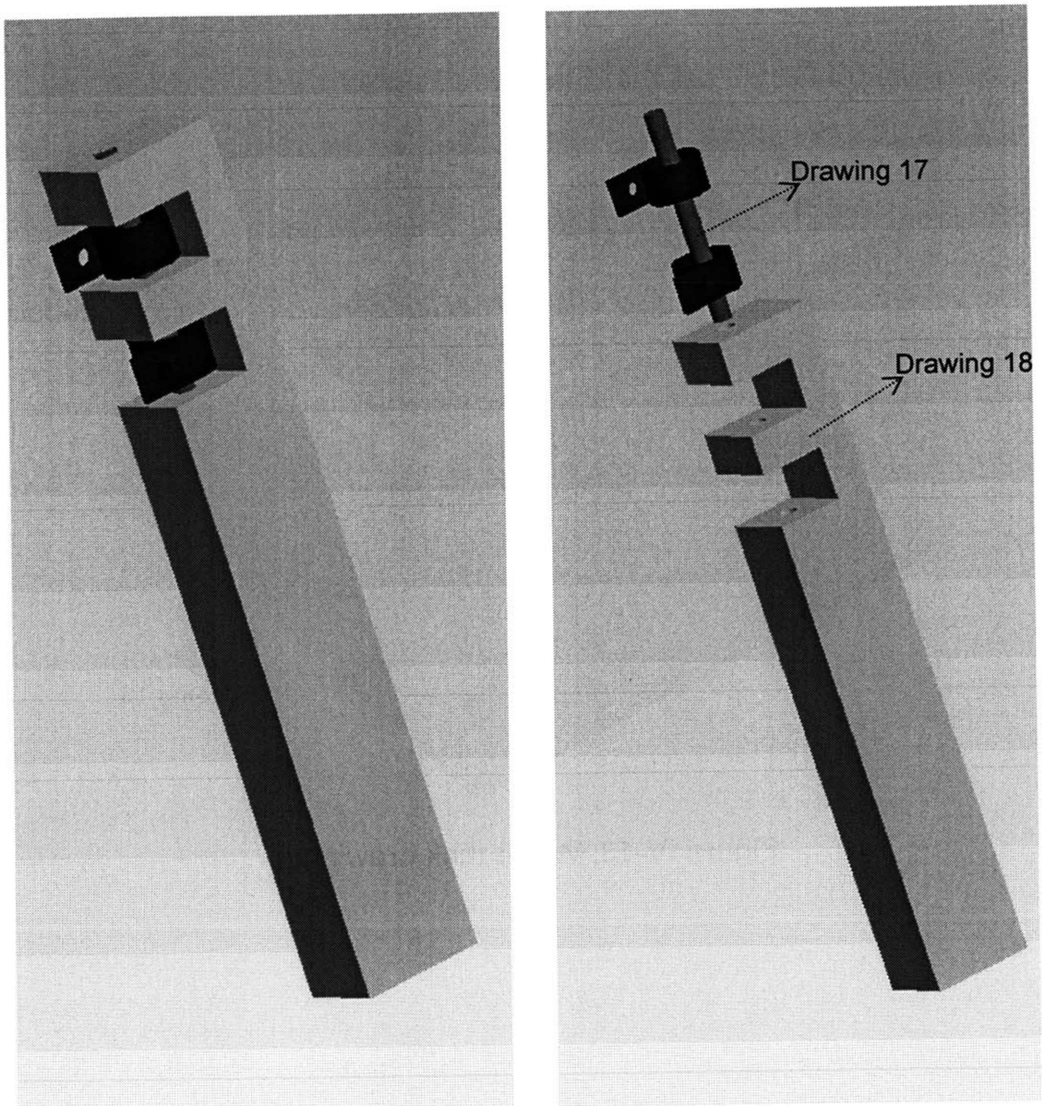

Figure IV-12: Preload drawings

Block IV: Water tank drawings

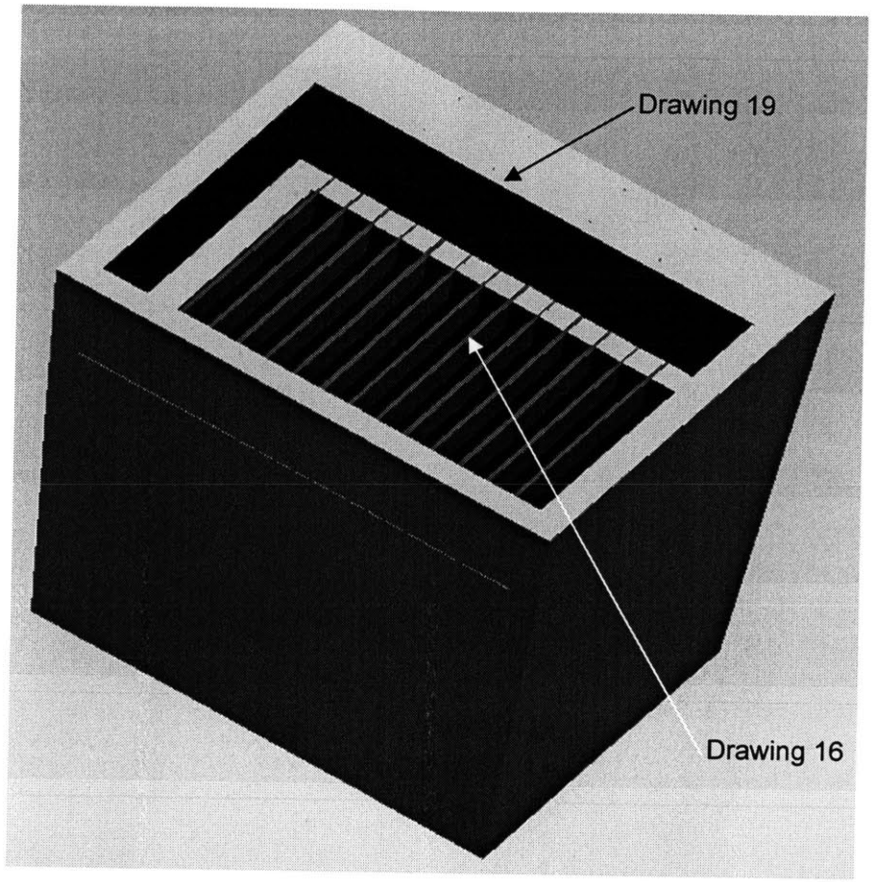

Figure IV-13: Water tank drawings

Block V: Joint seal drawings

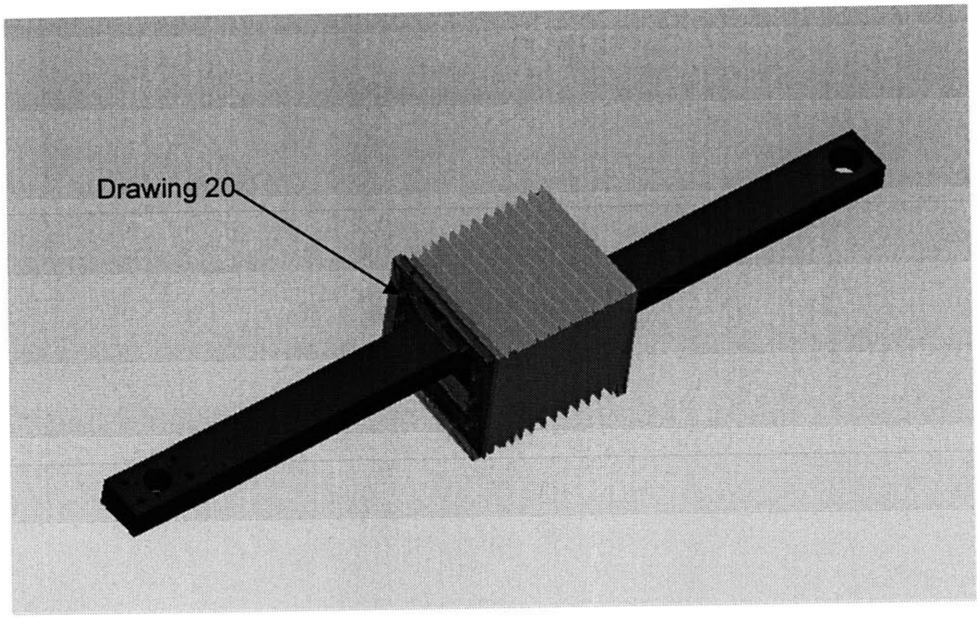

Figure IV-14: Joint seal drawings

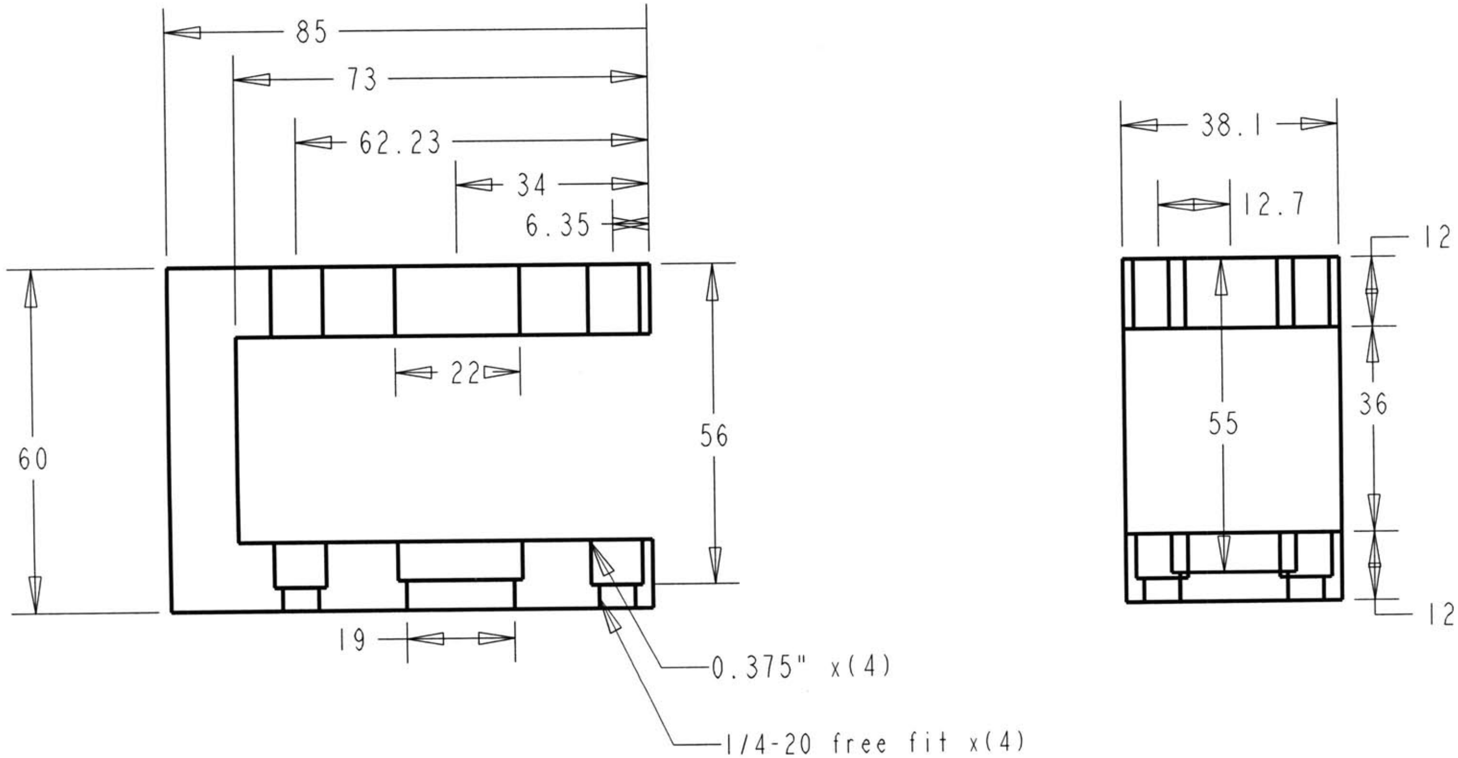

drawing 1
Qty: 2

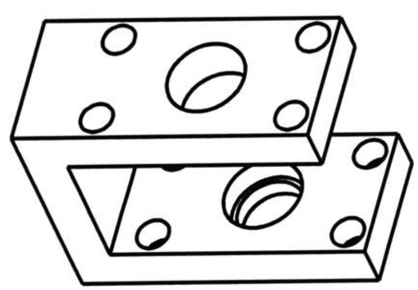

SCALE 0.500

MATERIAL Al-6061	DESIGN 5/7/2004 Fadi A Ibrahim	Massachusetts Institute of Technology Precision Engineering Research Group (PERG) 77 MASS. AVE, BUILDING 35-014, CAMBRIDGE, MA 02139
UNLESS OTHERWISE SPECIFIED DIMENSIONS ARE IN MM	DRAWN 23-Apr-04 Fadi A Ibrahim	TITLE Motor base, part 1 drawing 1
Property of PERG	TOLERANCES	
INERPRET PER ANSI Y14.5	0,0 ±0,15 0,00 ±0,05	PRO/E DRAW FILE DRW1 | REV
CODE IDENT 31413	ANGLES ± 1	SIZE A | SCALE 0.750 | SHEET 1 OF 1

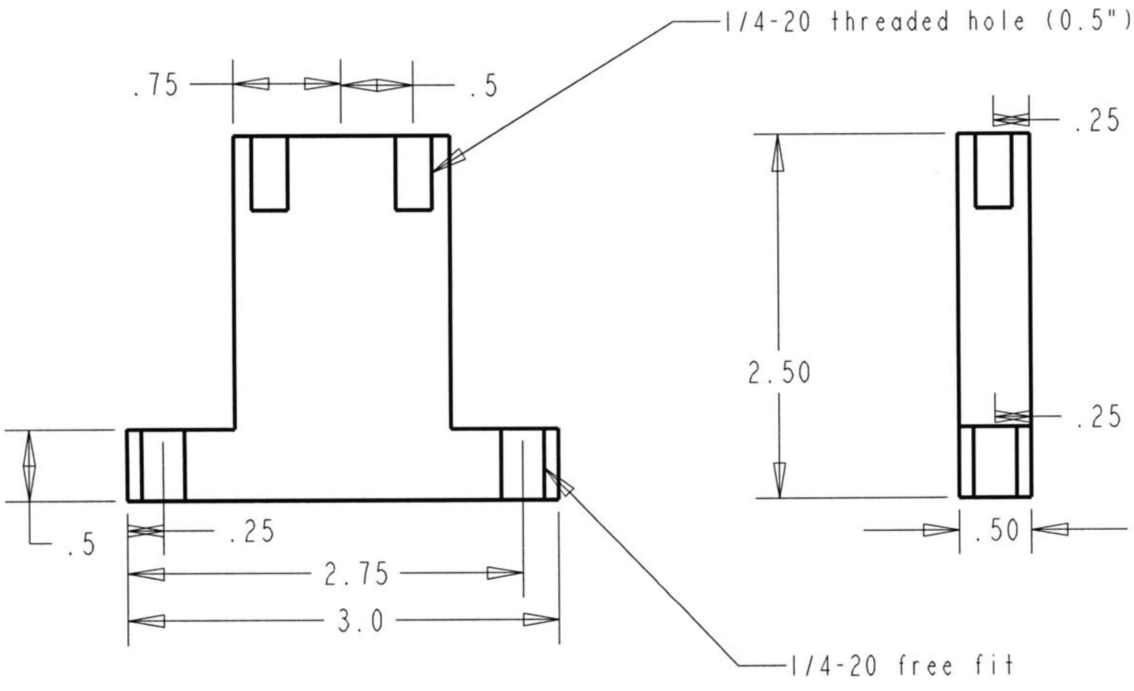

Drawing 2
Qty: 4
(INCHES)

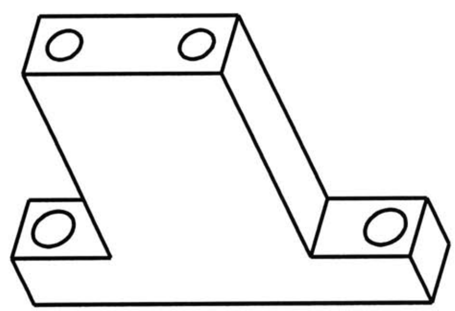

SCALE 0.750

MATERIAL Al-6061	DESIGN 5/7/2004 Fadi A Ibrahim		Massachusetts Institute of Technology Precision Engineering Research Group (PERG) 77 MASS. AVE, BUILDING 35-014, CAMBRIDGE, MA 02139	
UNLESS OTHERWISE SPECIFIED DIMENSIONS ARE IN MM	DRAWN 23-Apr-04 Fadi A Ibrahim		TITLE Motor Base 2 Drawing 2	
Property of PERG	TOLERANCES			
INERPRET PER ANSI Y14.5	0,0	±0,15	PRO/E DRAW FILE DRW2	REV
	0,00	±0,05		
CODE IDENT 31413	ANGLES	± 1	SIZE A	SCALE 0.750	SHEET 1 OF 1	

drawing 3
Qty: 2

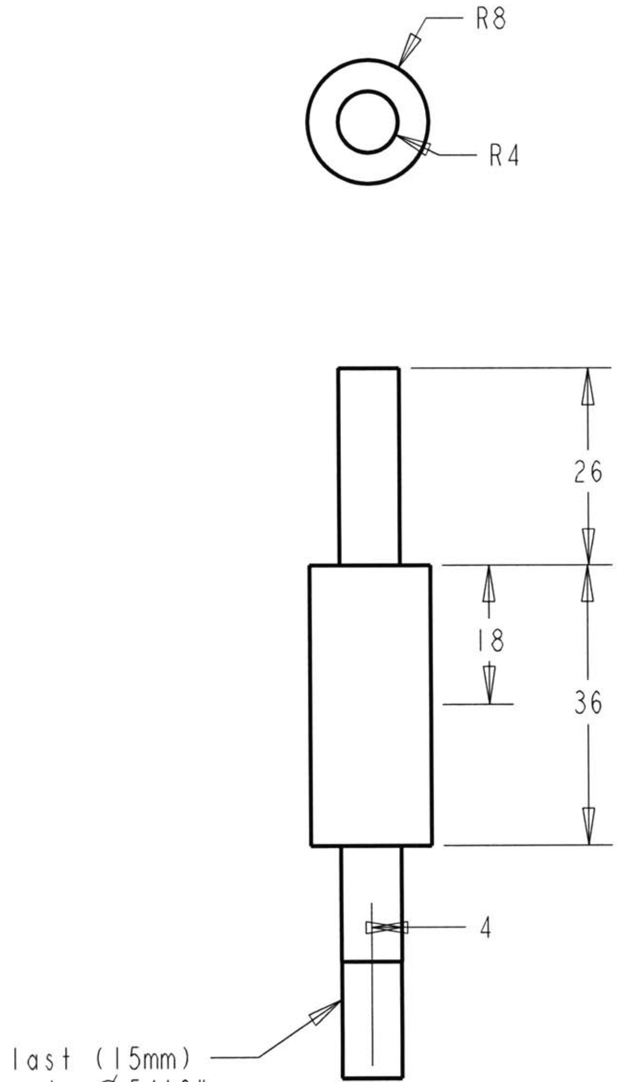

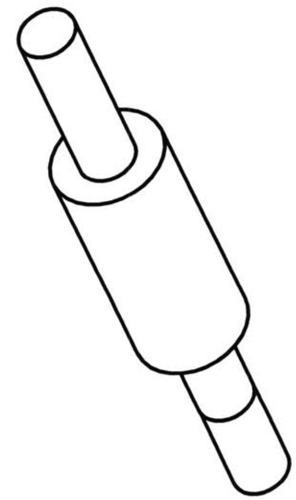

MATERIAL SS	DESIGN 5/7/2004 Fadi A Ibrahim	Massachusetts Institute of Technology Precision Engineering Research Group (PERG) 77 MASS. AVE, BUILDING 35-014, CAMBRIDGE, MA 02139
UNLESS OTHERWISE SPECIFIED DIMENSIONS ARE IN MM	DRAWN 23-Apr-04 Fadi A Ibrahim	TITLE Motor Base, part3 drawing 3

Property of PERG	TOLERANCES	
INERPRET PER ANSI Y14.5	0,0	±0,15
	0,00	±0,05
CODE IDENT 31413	ANGLES	± 1

PRO/E DRAW FILE DRW3		REV
SIZE A	SCALE 1.000	SHEET 1 OF 1

Drawing 4
Qty: 2
(INCHES)

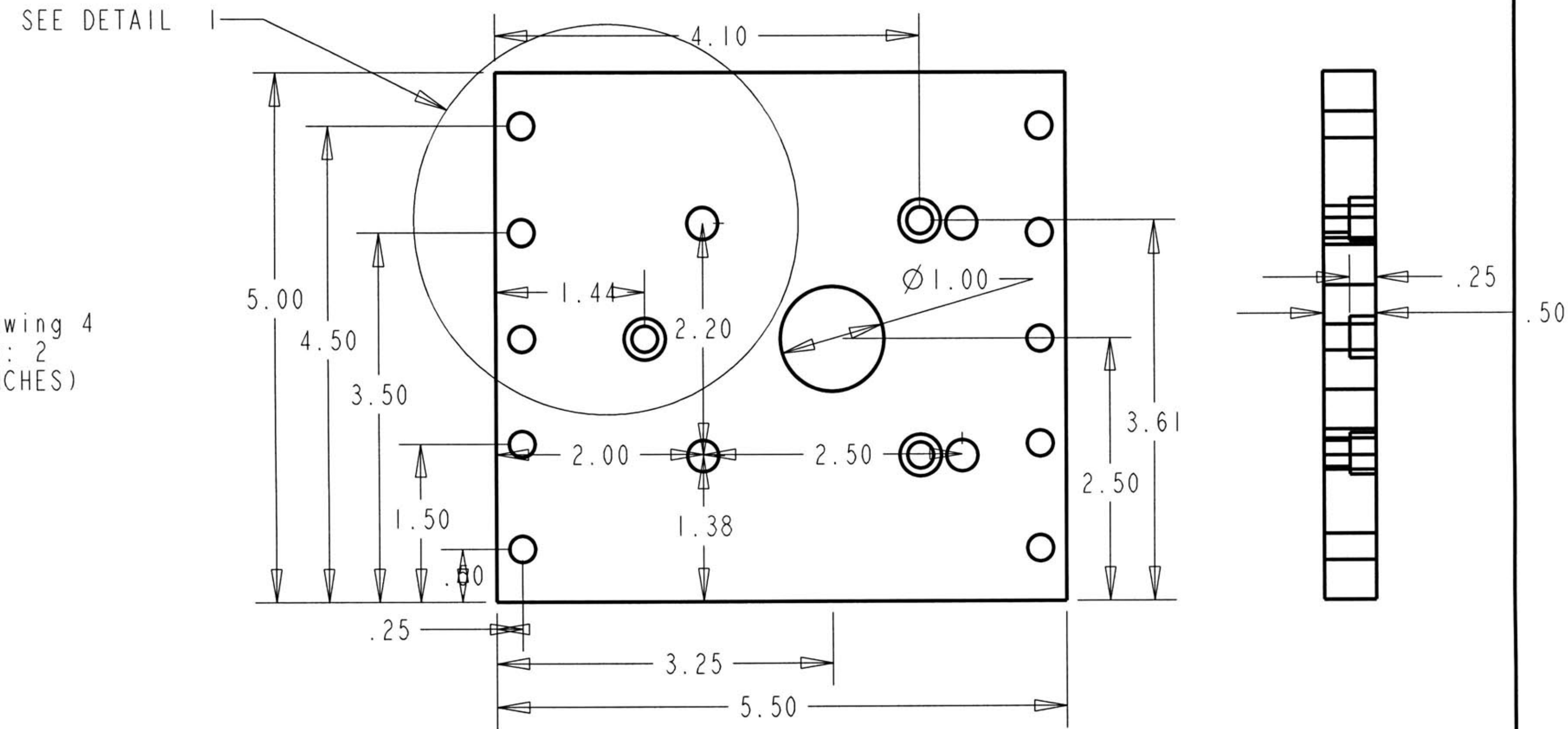

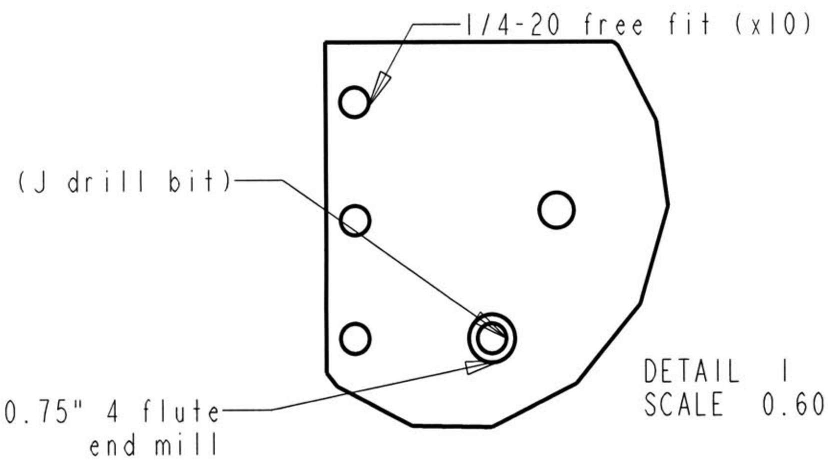

DETAIL 1
SCALE 0.600

MATERIAL Al-6061	DESIGN 5/7/2004 Fadi A Ibrahim	Massachusetts Institute of Technology Precision Engineering Research Group (PERG) 77 MASS. AVE, BUILDING 35-014, CAMBRIDGE, MA 02139	
UNLESS OTHERWISE SPECIFIED DIMENSIONS ARE IN MM	DRAWN 24-Apr-04 Fadi A Ibrahim	TITLE Motor Base, part 5 drawing 4	
Property of PERG	TOLERANCES		
INERPRET PER ANSI Y14.5	0,0 ±0,15	PRO/E DRAW FILE DRW4	REV
	0,00 ±0,05		
CODE IDENT 31413	ANGLES ± 1	SIZE A SCALE 0.600	SHEET 1 OF 1

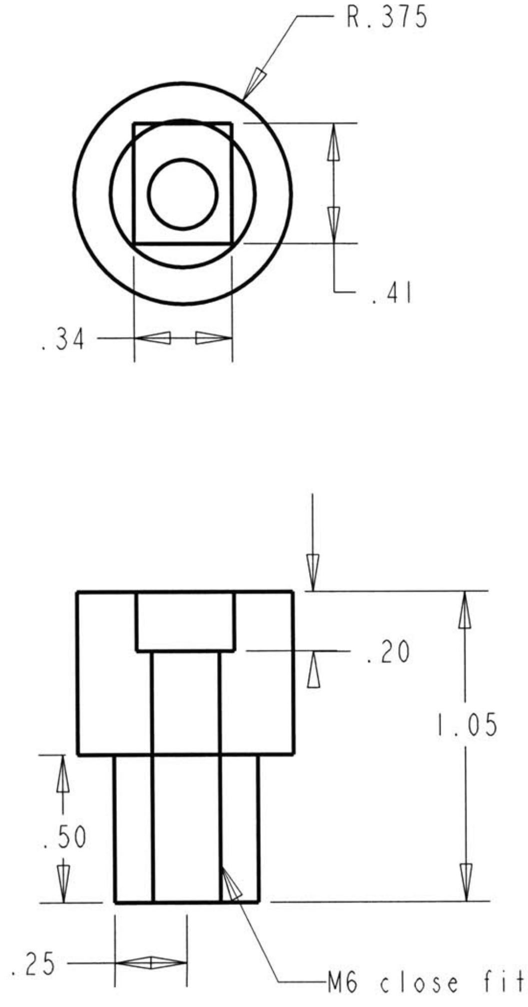

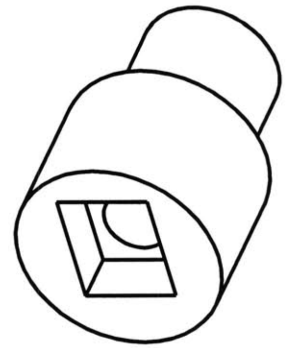

Drawing 5
Qty: 2
(INCHES)

MATERIAL SS	DESIGN 5/7/2004 Fadi A Ibrahim		Massachusetts Institute of Technology Precision Engineering Research Group (PERG) 77 MASS. AVE, BUILDING 35-014, CAMBRIDGE, MA 02139	
UNLESS OTHERWISE SPECIFIED DIMENSIONS ARE IN MM	DRAWN 24-Apr-04 Fadi A Ibrahim		TITLE Motor Base, part 5 drawing 5	
Property of PERG	TOLERANCES			
	0,0	±0,15		
INERPRET PER ANSI Y14.5	0,00	±0,05	PRO/E DRAW FILE DRW5	REV
CODE IDENT 31413	ANGLES	± 1	SIZE A	SCALE 1.500	SHEET 1 OF 1	

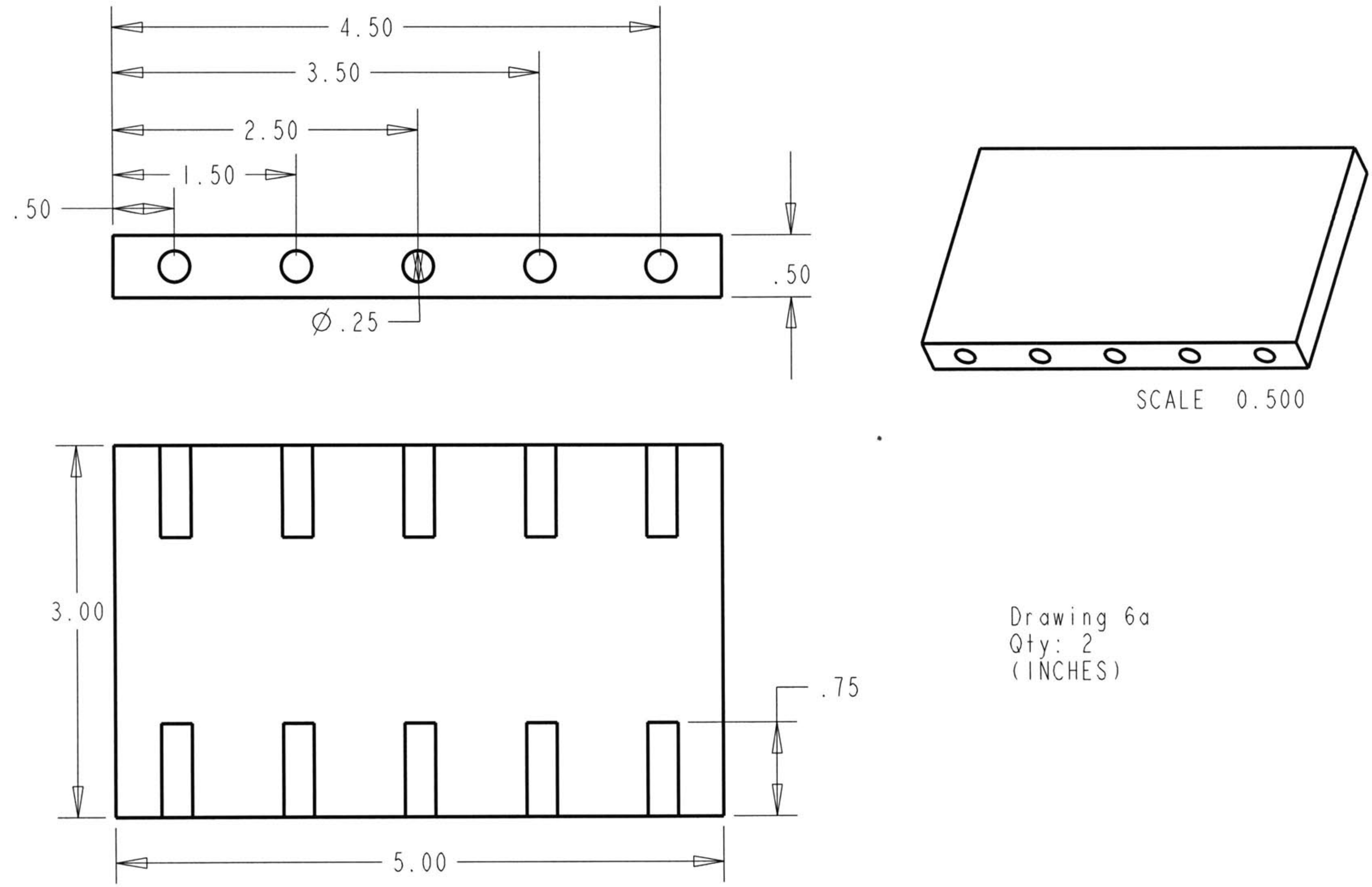

Drawing 6a
Qty: 2
(INCHES)

MATERIAL Al-6061	DESIGN 5/7/2004 Fadi A Ibrahim			Massachusetts Institute of Technology Precision Engineering Research Group (PERG) 77 MASS. AVE, BUILDING 35-014, CAMBRIDGE, MA 02139
UNLESS OTHERWISE SPECIFIED DIMENSIONS ARE IN MM	DRAWN 24-Apr-04 Fadi A Ibrahim			TITLE Motor Base, part6 drawing 6a
Property of PERG	TOLERANCES			
	0,0	±0,15		
INERPRET PER ANSI Y14.5	0,00	±0,05		PRO/E DRAW FILE DRW6A — REV
CODE IDENT 31413	ANGLES	± 1		SIZE A — SCALE 0.750 — SHEET 1 OF 1

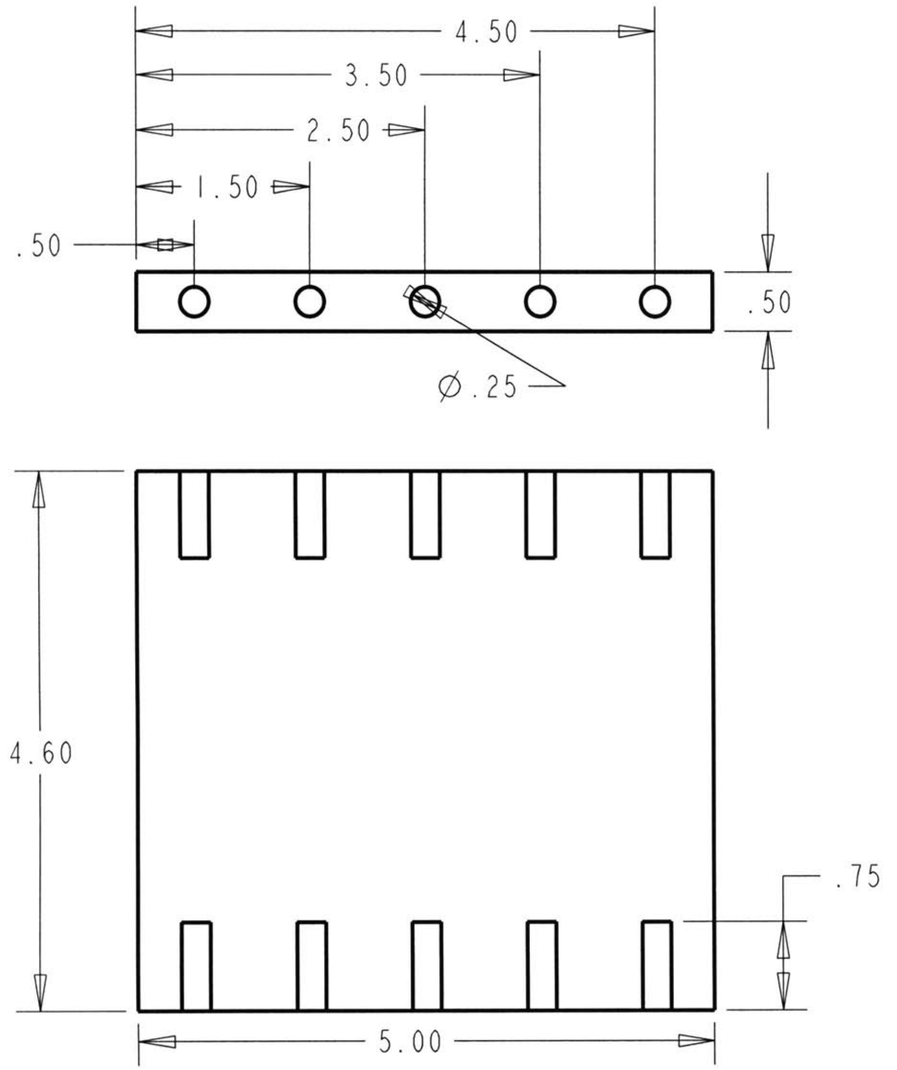

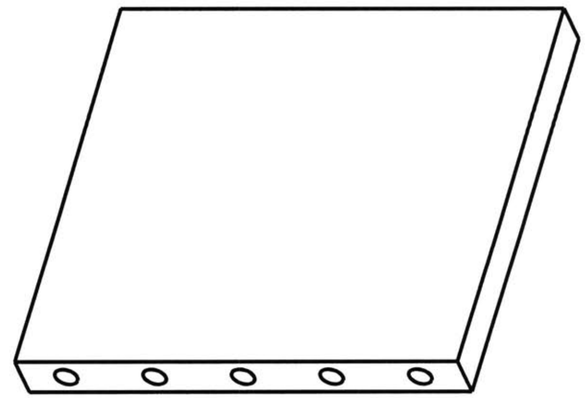

SCALE 0.500

Drawing 6B
Qty: 2
(INCHES)

MATERIAL Al-6061	DESIGN 5/7/2004 Fadi A Ibrahim	Massachusetts Institute of Technology Precision Engineering Research Group (PERG) 77 MASS. AVE, BUILDING 35-014, CAMBRIDGE, MA 02139
UNLESS OTHERWISE SPECIFIED DIMENSIONS ARE IN MM	DRAWN 24-Apr-04 Fadi A Ibrahim	TITLE Motor Base, part 6b drawing 6b
Property of PERG	TOLERANCES	
INERPRET PER ANSI Y14.5	0,0 ±0,15	PRO/E DRAW FILE DRW6B — REV
	0,00 ±0,05	
CODE IDENT 31413	ANGLES ± 1	SIZE A — SCALE 0.600 — SHEET 1 OF 1

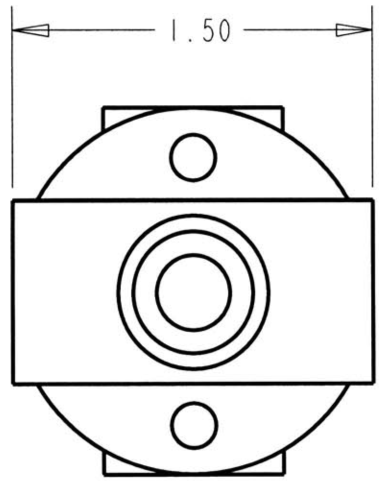

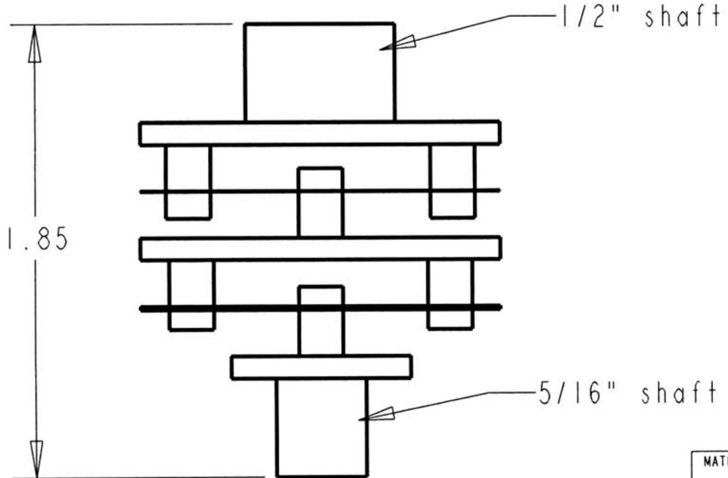

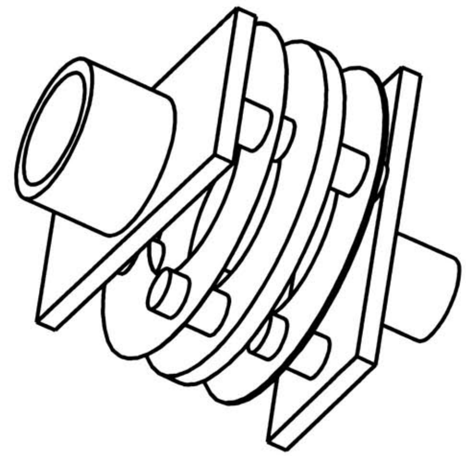

Drawing 7
Qty: 2
(INCHES)

MATERIAL SS	DESIGN Renbrandt	Massachusetts Institute of Technology Precision Engineering Research Group (PERG) 77 MASS. AVE, BUILDING 35-014, CAMBRIDGE, MA 02139
UNLESS OTHERWISE SPECIFIED DIMENSIONS ARE IN MM	DRAWN 04-May-04 Fadi A Ibrahim	TITLE HT coupling drawing 7
Property of PERG	TOLERANCES	
INERPRET PER ANSI Y14.5	0,0 ±0,15	
	0,00 ±0,05	PRO/E DRAW FILE DRW7 — REV
CODE IDENT 31413	ANGLES ± 1	SIZE A — SCALE 1.250 — SHEET 1 OF 1

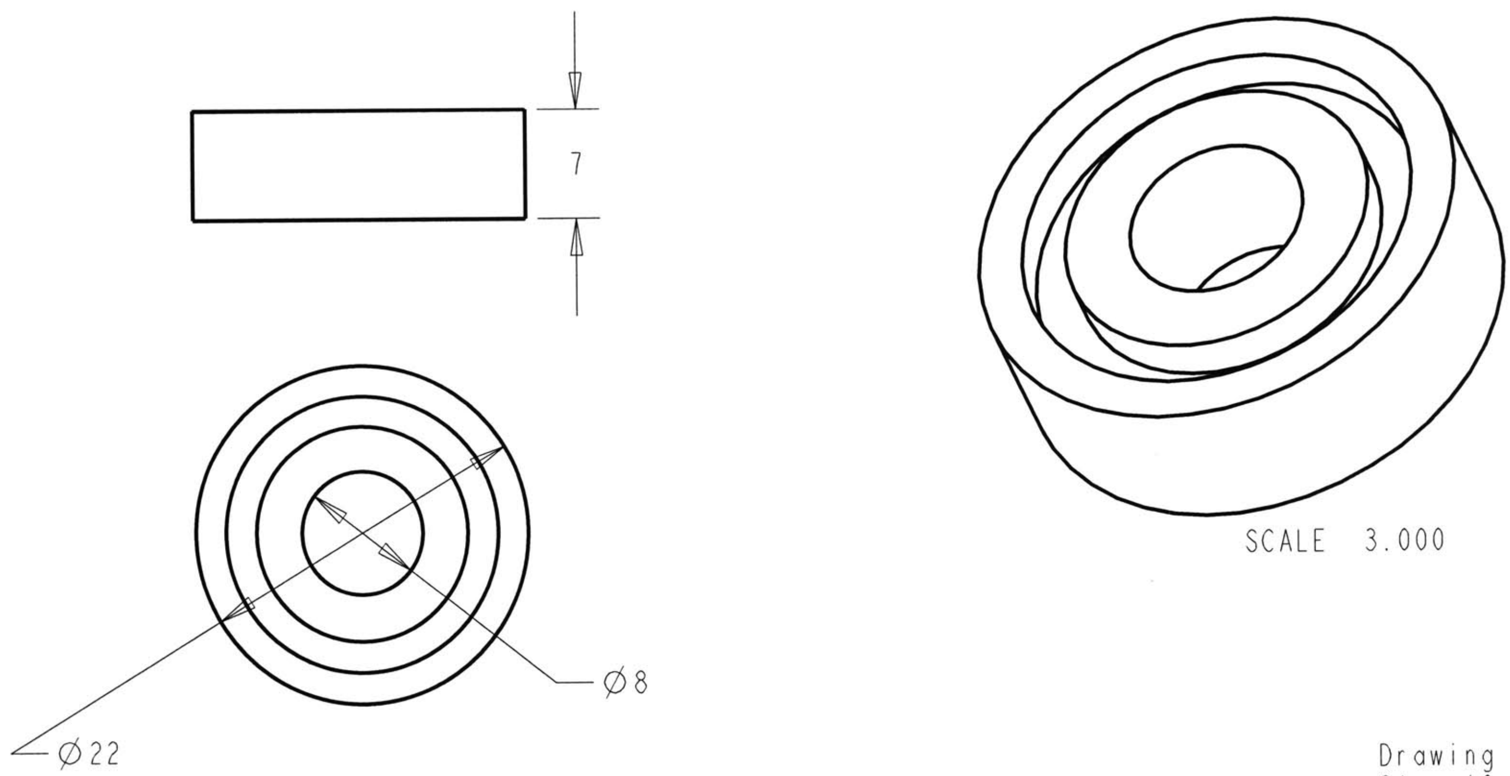

Drawing 8
Qty: 10

MATERIAL SS	DESIGN 5/7/2004 AIA bearings	Massachusetts Institute of Technology Precision Engineering Research Group (PERG) 77 MASS. AVE, BUILDING 35-014, CAMBRIDGE, MA 02139
UNLESS OTHERWISE SPECIFIED DIMENSIONS ARE IN MM	DRAWN 04-May-04 Fadi A Ibrahim	TITLE Bearings drawing 8
Property of PERG	TOLERANCES	
INERPRET PER ANSI Y14.5	0,0 ±0,15 / 0,00 ±0,05	PRO/E DRAW FILE DRW8 REV
CODE IDENT 31413	ANGLES ± 1	SIZE A SCALE 2.000 SHEET 1 OF 1

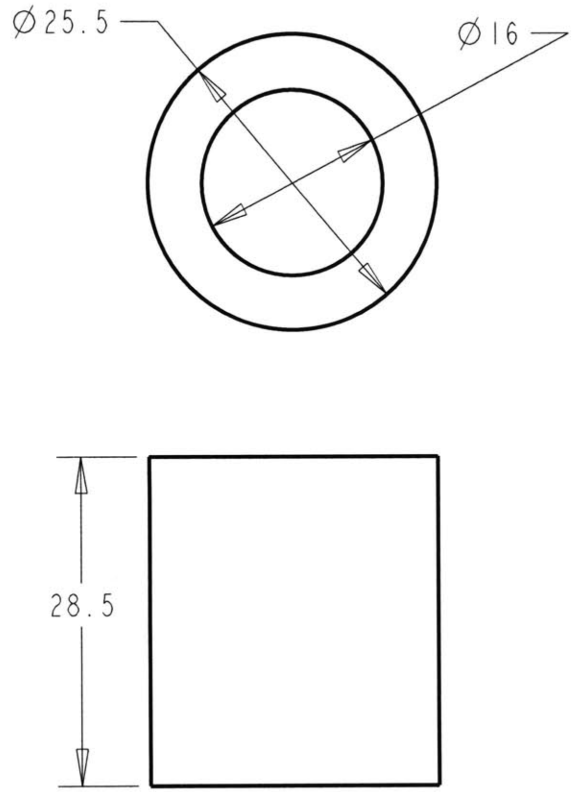

Drawing 9
Qty: 5
Intended to give a sense of size,
not details

MATERIAL Steel	DESIGN 5/7/2004 Fenner Drives	Massachusetts Institute of Technology Precision Engineering Research Group (PERG) 77 MASS. AVE, BUILDING 35-014, CAMBRIDGE, MA 02139
UNLESS OTHERWISE SPECIFIED DIMENSIONS ARE IN MM	DRAWN 04-May-04 Fadi A Ibrahim	TITLE Keyless Bushing drawing 9
Property of PERG	TOLERANCES	
INERPRET PER ANSI Y14.5	0,0 ±0,15 0,00 ±0,05	PRO/E DRAW FILE DRW9 REV
CODE IDENT 31413	ANGLES ± 1	SIZE A SCALE 1.500 SHEET 1 OF 1

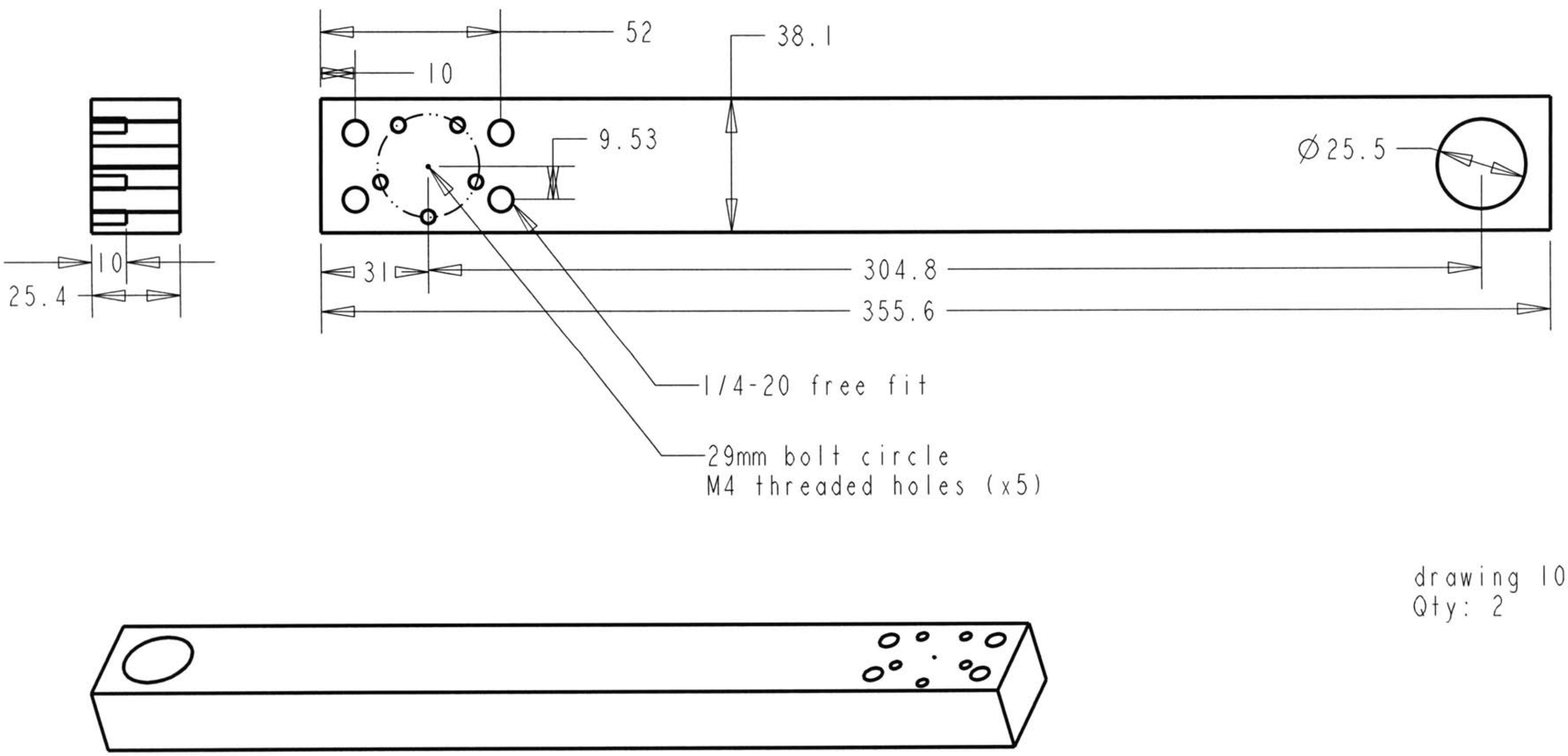

SCALE 0.400

MATERIAL Al-6061	DESIGN 5/7/2004 Fadi A Ibrahim		Massachusetts Institute of Technology Precision Engineering Research Group (PERG) 77 MASS. AVE, BUILDING 35-014, CAMBRIDGE, MA 02139
UNLESS OTHERWISE SPECIFIED DIMENSIONS ARE IN MM	DRAWN 24-Apr-04 Fadi A Ibrahim		TITLE Arms, part 1 drawing 10
Property of PERG	TOLERANCES		
INERPRET PER ANSI Y14.5	0,0	±0,15	PRO/E DRAW FILE DRW10
	0,00	±0,05	REV
CODE IDENT 31413	ANGLES	± 1	SIZE A | SCALE 0.500 | SHEET 1 OF 1

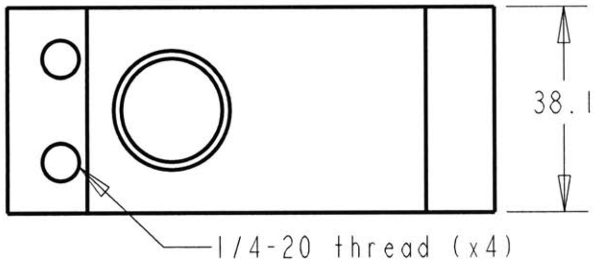

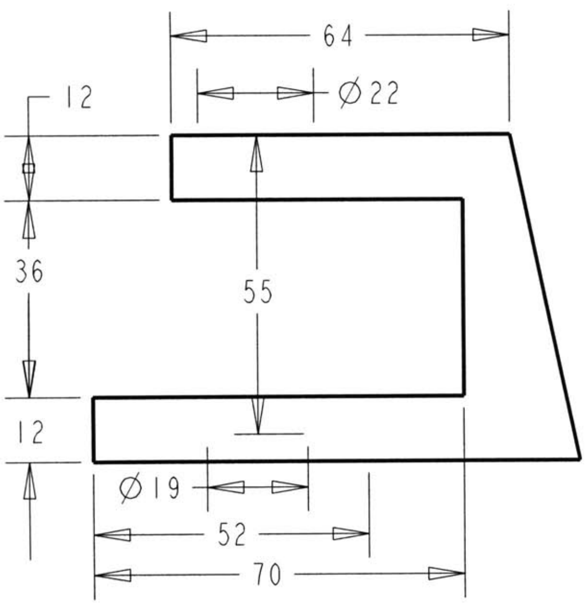

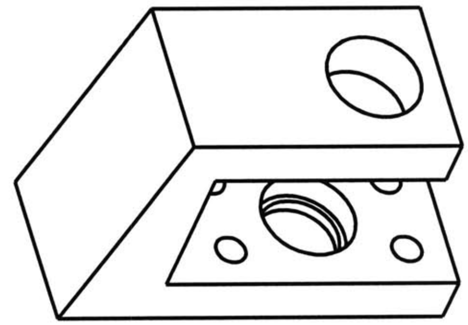

SCALE 0.600

Drawing 11
Qty: 3

MATERIAL Al-6061	DESIGN 5/7/2004 Fadi A Ibrahim			Massachusetts Institute of Technology Precision Engineering Research Group (PERG) 77 MASS. AVE, BUILDING 35-014, CAMBRIDGE, MA 02139
UNLESS OTHERWISE SPECIFIED DIMENSIONS ARE IN MM	DRAWN 24-Apr-04 Fadi A Ibrahim			TITLE Arms, part 3 drawing 11
Property of PERG		TOLERANCES		
		0,0	±0,15	
INERPRET PER ANSI Y14.5		0,00	±0,05	PRO/E DRAW FILE DRW11 — REV
CODE IDENT 31413		ANGLES	± 1	SIZE A — SCALE 0.700 — SHEET 1 OF 1

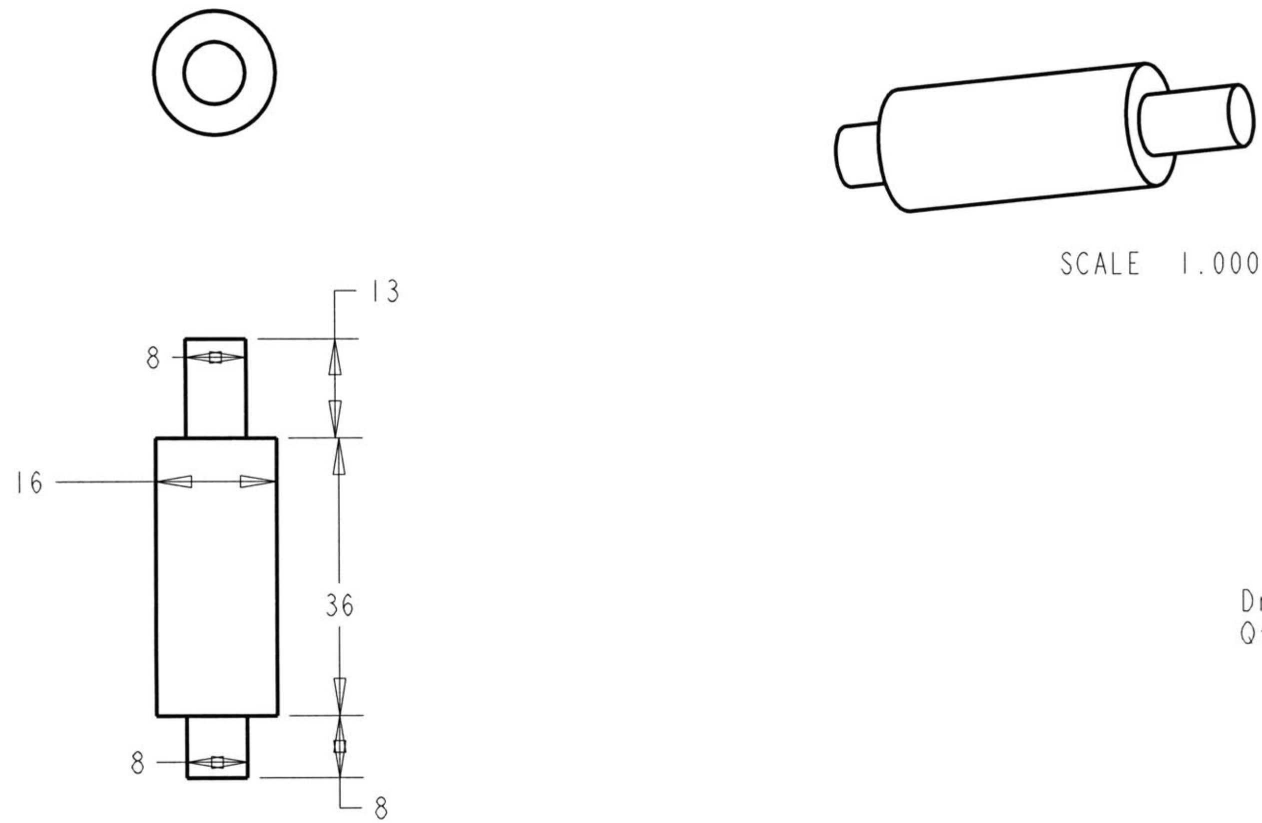

Drawing 12
Qty: 3

MATERIAL SS	DESIGN 5/7/2004 Fadi A Ibrahim		Massachusetts Institute of Technology Precision Engineering Research Group (PERG) 77 MASS. AVE, BUILDING 35-014, CAMBRIDGE, MA 02139
UNLESS OTHERWISE SPECIFIED DIMENSIONS ARE IN MM	DRAWN 24-Apr-04 Fadi A Ibrahim		TITLE Arms, part 4 drawing 12
Property of PERG	TOLERANCES		
INERPRET PER ANSI Y14.5	0,0	±0,15	PRO/E DRAW FILE DRW12 REV
	0,00	±0,05	
CODE IDENT 31413	ANGLES	± 1	SIZE A | SCALE 1.000 | SHEET 1 OF 1

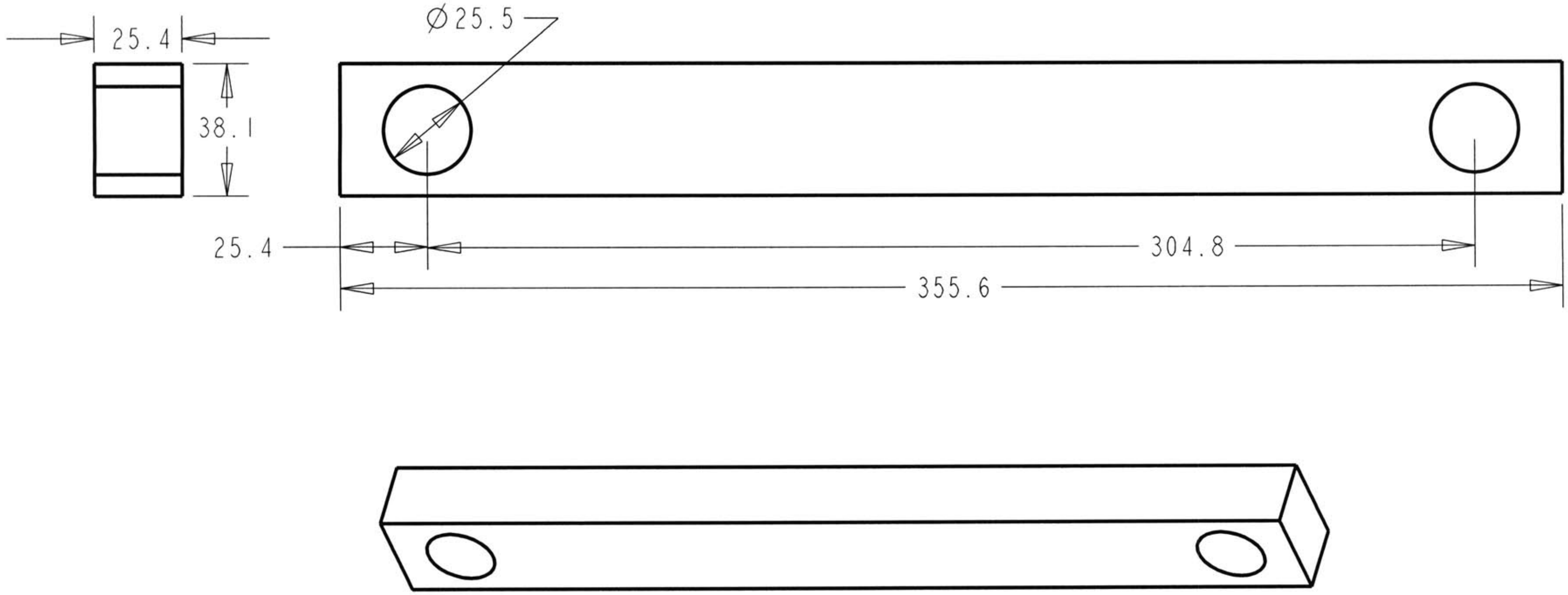

SCALE 0.400

Drawing 13
Qty: 2

MATERIAL Al-6061	DESIGN 5/7/2004 Fadi A Ibrahim	Massachusetts Institute of Technology Precision Engineering Research Group (PERG) 77 MASS. AVE, BUILDING 35-014, CAMBRIDGE, MA 02139
UNLESS OTHERWISE SPECIFIED DIMENSIONS ARE IN MM	DRAWN 24-Apr-04 Fadi A Ibrahim	TITLE Arms, part 2 drawing 13
Property of PERG	TOLERANCES	
INERPRET PER ANSI Y14.5	0,0 ±0,15 0,00 ±0,05	PRO/E DRAW FILE DRW13 / REV
CODE IDENT 31413	ANGLES ± 1	SIZE A / SCALE 0.500 / SHEET 1 OF 1

Drawing 14
Qty: 2
(inches)

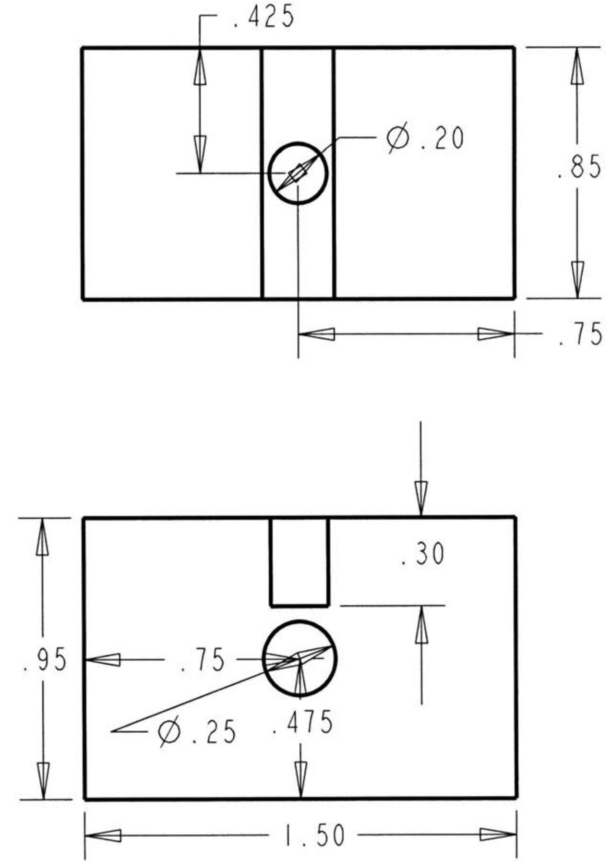

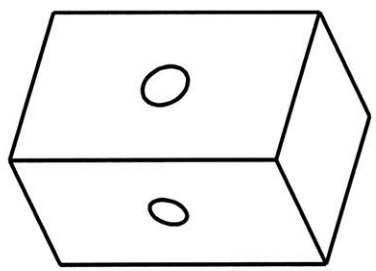

SCALE 1.000

MATERIAL Al-6061	DESIGN 5/7/2004 Fadi A Ibrahim	Massachusetts Institute of Technology Precision Engineering Research Group (PERG) 77 MASS. AVE, BUILDING 35-014, CAMBRIDGE, MA 02139
UNLESS OTHERWISE SPECIFIED DIMENSIONS ARE IN MM	DRAWN 24-Apr-04 Fadi A Ibrahim	TITLE Arms, part 7 drawing 14
Property of PERG	TOLERANCES	
INERPRET PER ANSI Y14.5	0,0 ±0,15 0,00 ±0,05	PRO/E DRAW FILE DRW14 / REV
CODE IDENT 31413	ANGLES ± 1	SIZE A / SCALE 1.500 / SHEET 1 OF 1

Drawing 15
Qty: 2
(INCHES)

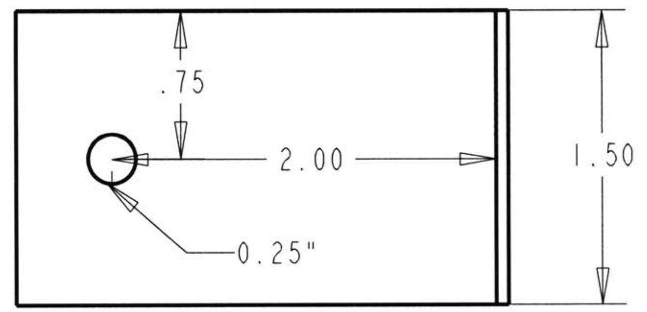

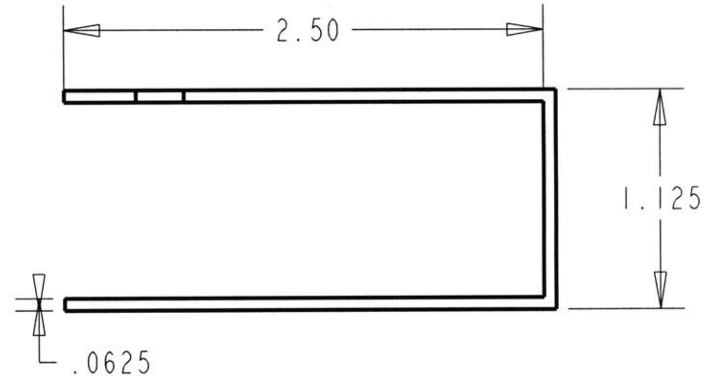

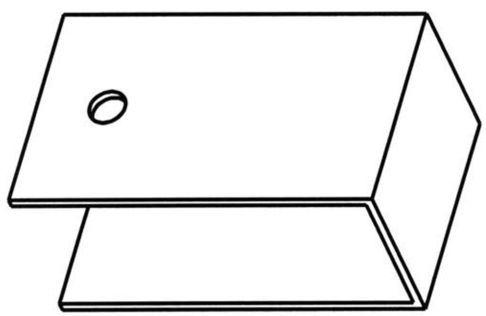

SCALE 0.800

MATERIAL Al-6061	DESIGN 5/7/2004 Fadi A Ibrahim		Massachusetts Institute of Technology Precision Engineering Research Group (PERG) 77 MASS. AVE, BUILDING 35-014, CAMBRIDGE, MA 02139	
UNLESS OTHERWISE SPECIFIED DIMENSIONS ARE IN MM	DRAWN 24-Apr-04 Fadi A Ibrahim		TITLE Arms, part 6 drawing 15	
Property of PERG	TOLERANCES			
INERPRET PER ANSI Y14.5	0,0	±0,15	PRO/E DRAW FILE DRW15	REV
	0,00	±0,05		
CODE IDENT 31413	ANGLES	± 1	SIZE A	SCALE 1.000 SHEET 1 OF 1

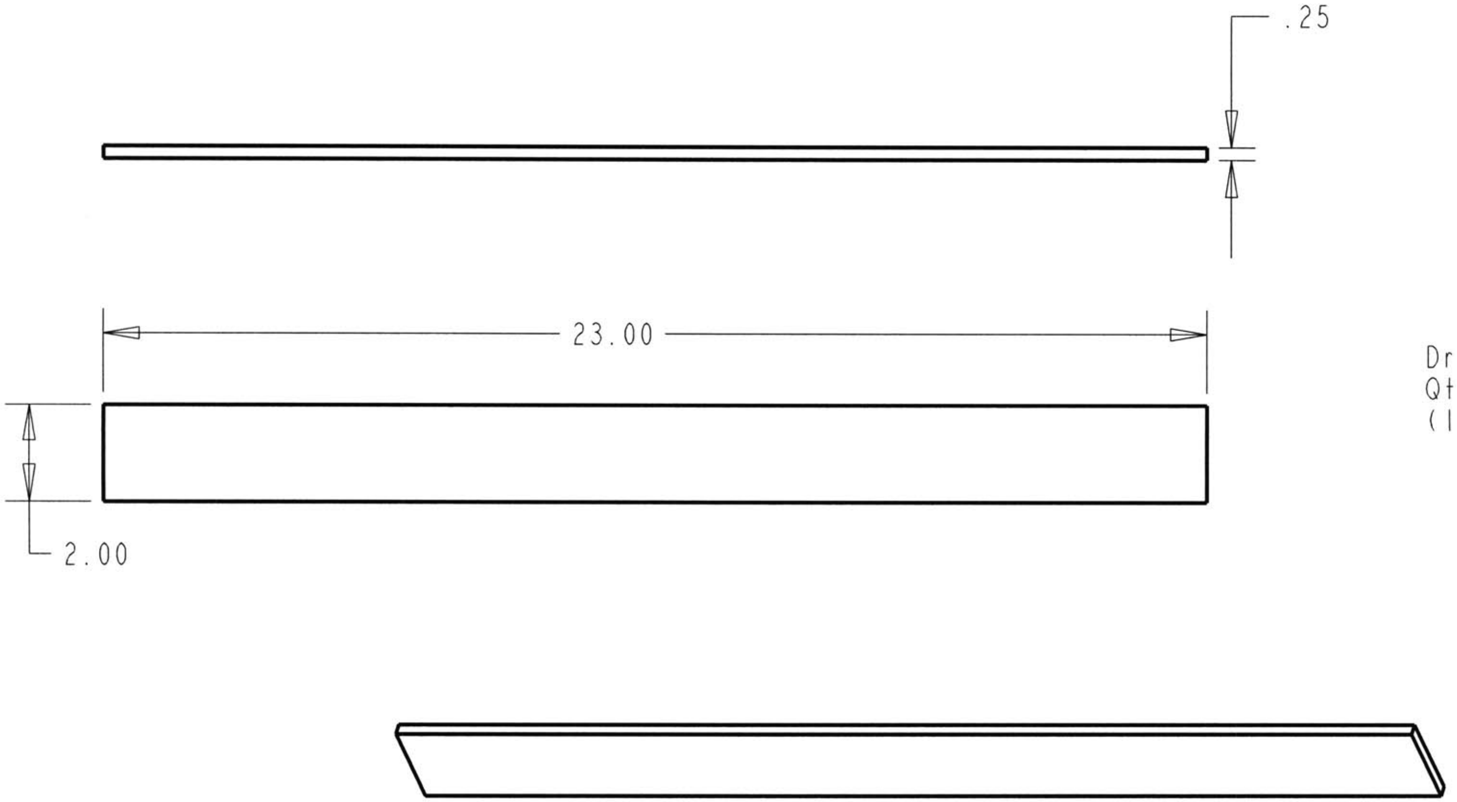

SCALE 0.250

Drawing 16
Qty: 14
(INCHES)

MATERIAL Al 6061	DESIGN 5/7/3004 Ethan Crumlin, Fadi Ibrahim		Massachusetts Institute of Technology Precision Engineering Research Group (PERG) 77 MASS. AVE, BUILDING 35-014, CAMBRIDGE, MA 02139
UNLESS OTHERWISE SPECIFIED DIMENSIONS ARE IN MM	DRAWN 06-May-04 Ethan Crumlin		TITLE
Property of PERG	TOLERANCES		Fins drawing 16
	0,0	±0,15	
INERPRET PER ANSI Y14.5	0,00	±0,05	PRO/E DRAW FILE DRW16 — REV
CODE IDENT 31413	ANGLES	± 1	SIZE A — SCALE 0.250 — SHEET 1 OF 1

Drawing 17
Qty: 2
(INCHES)

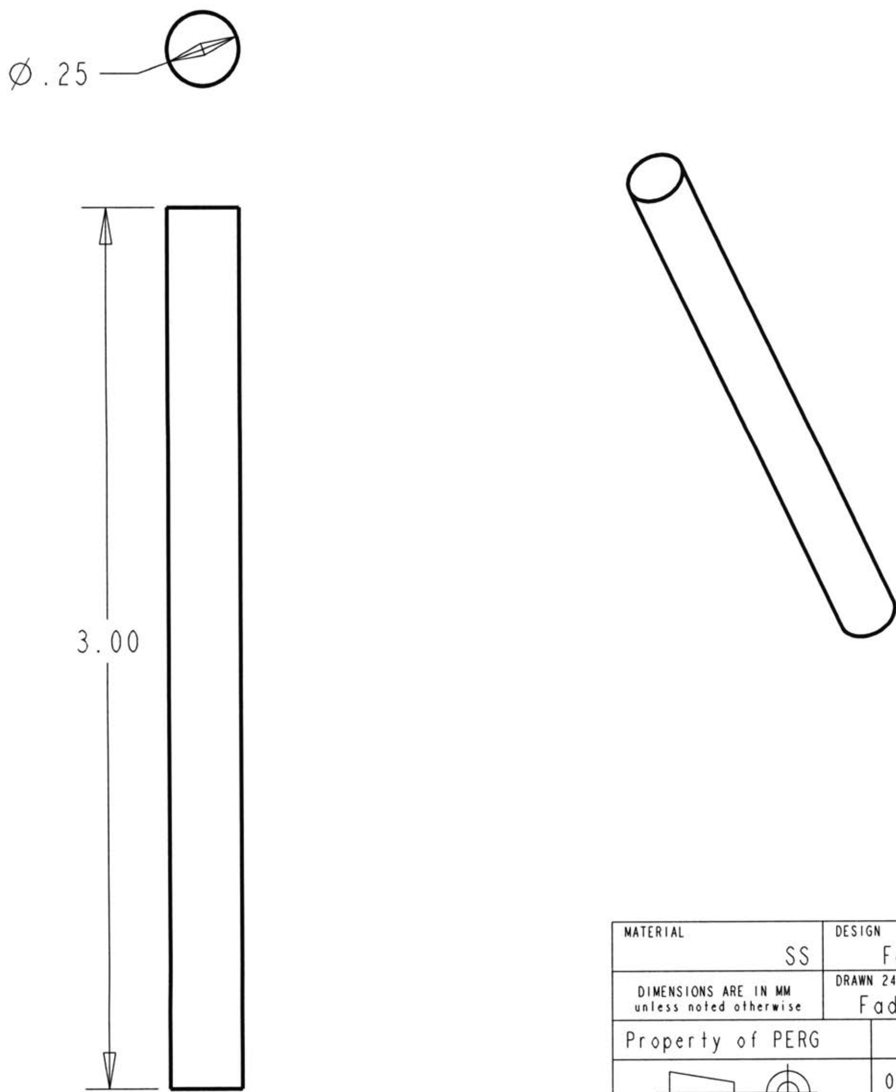

SCALE 1.200

MATERIAL SS	DESIGN 5/7/2004 Fadi A Ibrahim	Massachusetts Institute of Technology Precision Engineering Research Group (PERG) 77 MASS. AVE, BUILDING 35-014, CAMBRIDGE, MA 02139	
DIMENSIONS ARE IN MM unless noted otherwise	DRAWN 24-Apr-04 Fadi A Ibrahim	TITLE Preload, Part 1 drawing 17	
Property of PERG	TOLERANCES		
INERPRET PER ANSI Y14.5	0,0 ±0,15	PRO/E DRAW FILE DRW17	REV
	0,00 ±0,05		
CODE IDENT 31413	ANGLES ± 1	SIZE A SCALE 1.500	SHEET 1 OF 1

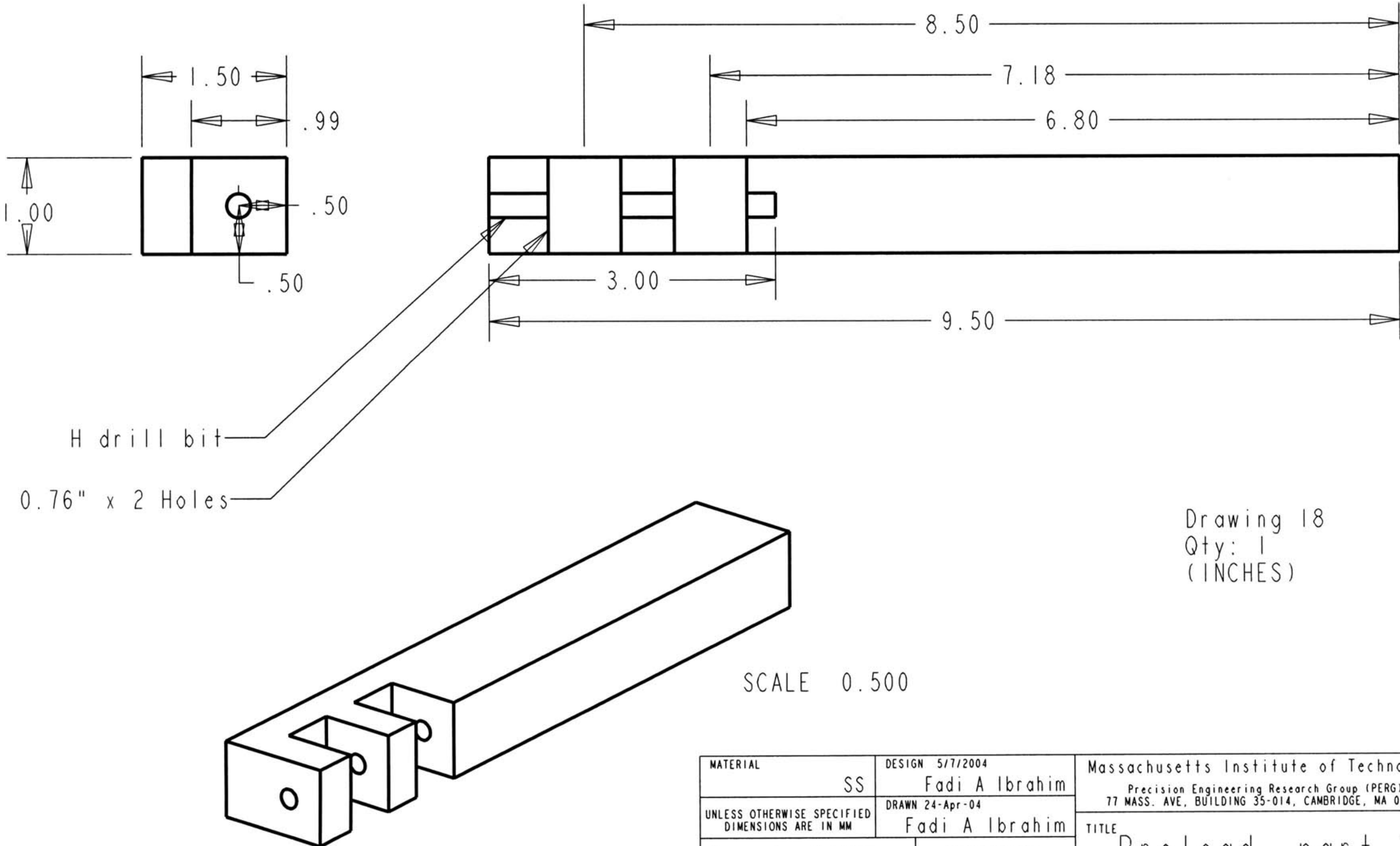

MATERIAL SS

DESIGN 5/7/2004 Fadi A Ibrahim

DRAWN 24-Apr-04 Fadi A Ibrahim

UNLESS OTHERWISE SPECIFIED DIMENSIONS ARE IN MM

Property of PERG

TOLERANCES	
0,0	±0,15
0,00	±0,05
ANGLES	± 1

INERPRET PER ANSI Y14.5

CODE IDENT 31413

Massachusetts Institute of Technology

Precision Engineering Research Group (PERG)
77 MASS. AVE, BUILDING 35-014, CAMBRIDGE, MA 02139

TITLE Preload, part 2
drawing 18

PRO/E DRAW FILE DRW18

REV

SIZE A | SCALE 0.600 | SHEET 1 OF 1

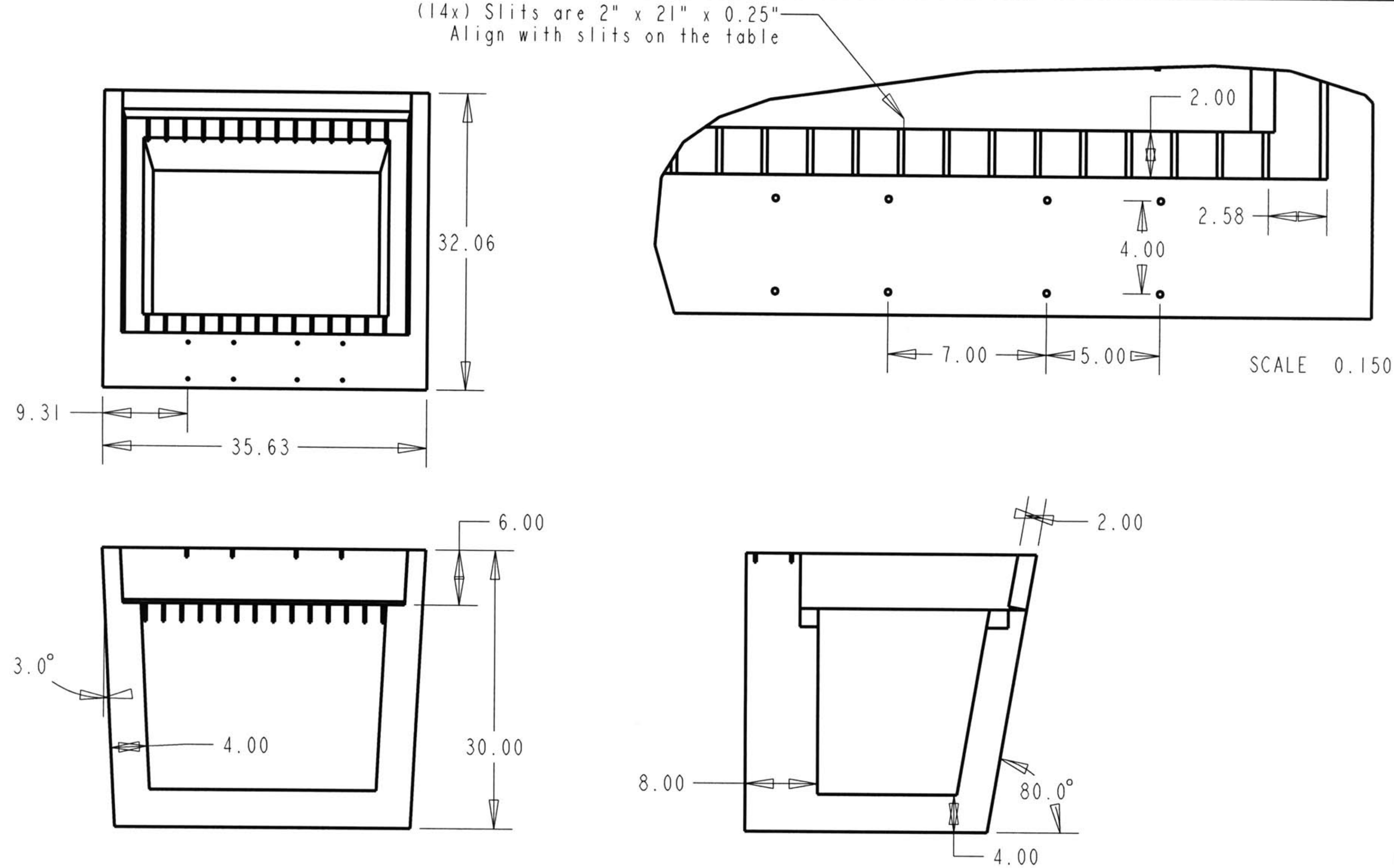

MATERIAL Polymer Concrete	DESIGN 5/7/2004 Fadi A Ibrahim	Massachusetts Institute of Technology Precision Engineering Research Group (PERG) 77 MASS. AVE, BUILDING 35-014, CAMBRIDGE, MA 02139
UNLESS OTHERWISE SPECIFIED DIMENSIONS ARE IN MM	DRAWN 10-May-04 Fadi A Ibrahim	TITLE Water Bed drawing 19
Property of PERG	TOLERANCES	
INERPRET PER ANSI Y14.5	0,0 ±0,15 0,00 ±0,05	PRO/E DRAW FILE DRW19 — REV
CODE IDENT 31413	ANGLES ± 1	SIZE A — SCALE 0.060 — SHEET 1 OF 1

Drawing 19
Qty: 1
(INCHES)

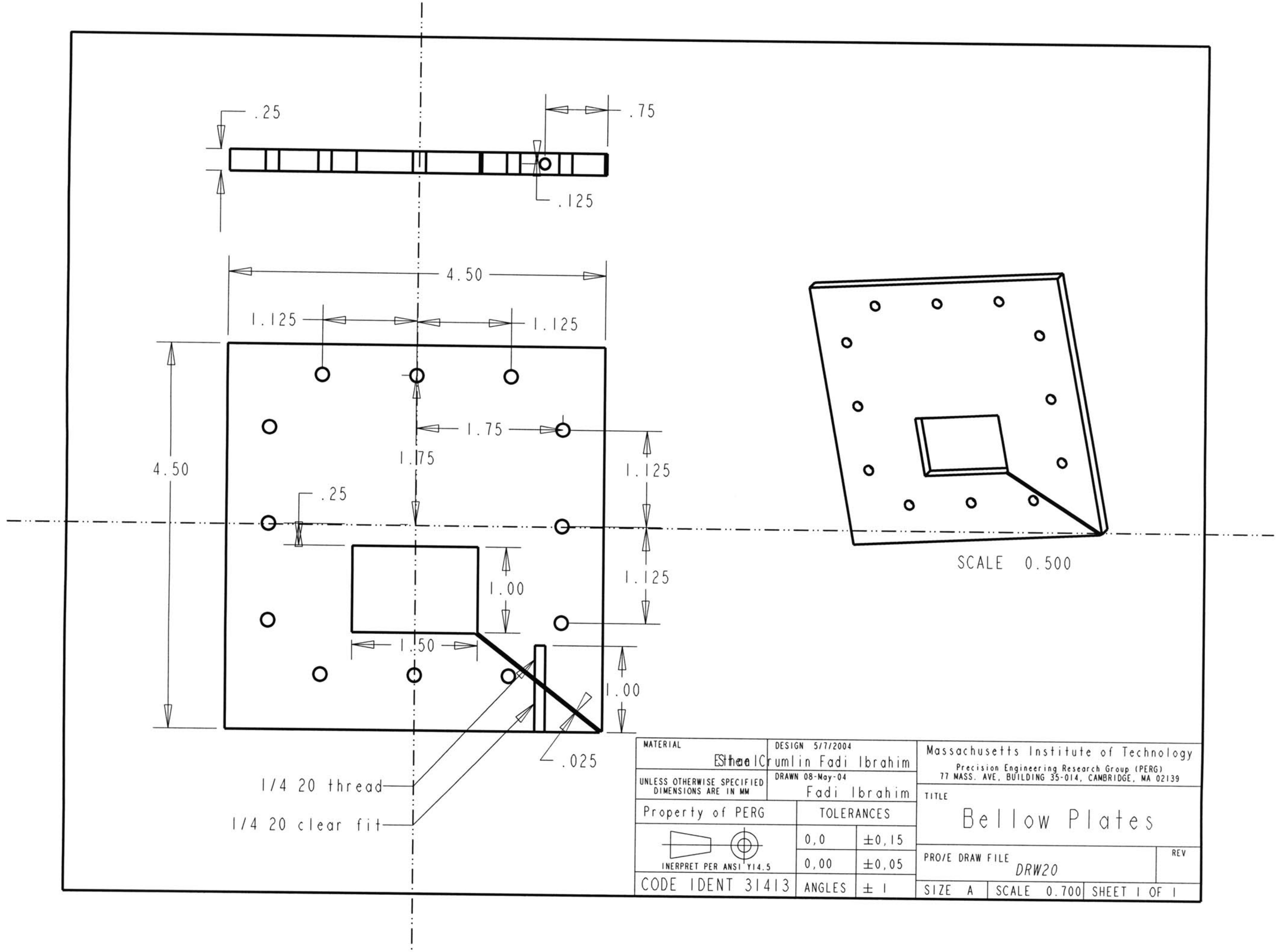

MATERIAL	DESIGN 5/7/2004 Esther Crumlin Fadi Ibrahim		Massachusetts Institute of Technology Precision Engineering Research Group (PERG) 77 MASS. AVE, BUILDING 35-014, CAMBRIDGE, MA 02139
UNLESS OTHERWISE SPECIFIED DIMENSIONS ARE IN MM	DRAWN 08-May-04 Fadi Ibrahim		TITLE Bellow Plates
Property of PERG	TOLERANCES		
INERPRET PER ANSI Y14.5	0,0	±0,15	
	0,00	±0,05	PRO/E DRAW FILE DRW20 REV
CODE IDENT 31413	ANGLES	± 1	SIZE A | SCALE 0.700 | SHEET 1 OF 1